UCLA
UCLA Electronic Theses and Dissertations

Title

Ultra-stretchable Electronic Rubber Band for Electrical Stimulation, Electromyography and Gastrointestinal Motility Monitoring

Permalink

https://escholarship.org/uc/item/2bv575gk

Author

Chung, Pei-Shan

Publication Date

2021

Supplemental Material

https://escholarship.org/uc/item/2bv575gk#supplemental

Peer reviewed|Thesis/dissertation

UNIVERSITY OF CALIFORNIA

Los Angeles

Ultra-stretchable Electronic Rubber Band for Electrical Stimulation, Electromyography and

Gastrointestinal Motility Monitoring

A dissertation submitted in partial satisfaction of the

requirements for the degree Doctor of Philosophy

in Bioengineering

by

Pei-Shan Chung

2021

ABSTRACT OF THE DISSERTATION

Ultra-Stretchable Electronic Rubber Band

for Electrical Stimulation, Electromyography and Gastrointestinal Motility Monitoring

by

Pei-Shan Chung

Doctor of Philosophy in Bioengineering

University of California, Los Angeles, 2021

Professor Pei-Yu Chiou, Chair

Gastrointestinal (GI) pacing for stomach and intestines, analogous to cardiac pacing for heart, has been an emerging electrotherapy to entrain omnipresent bioelectrical activity and stimulate contraction of smooth muscle cells (SMCs), especially for patients who are refractory to medical therapy. Concurrent tracking of the electrical activities of SMCs and mechanical responses of the GI tract can offer essential and quantitative information to interpret and mitigate stimulated

digestive processes. However, existing technologies for concurrent measurements of electrical and mechanical responses are still limited. The major limitations are the rigid nature of insertion electrodes and sensors, and the lack of highly stretchable and conformal platforms to accommodate the free-moving and stretchable nature of small and large intestines.

In this dissertation, an ultra-stretchable electronic rubber band, which we called e-band, has been demonstrated on slaughtered and neuroactive porcine small intestine segments for the functions of electrical stimulation, electromyography, and tissue motility recordings. The latter includes tissue impedance measurement and transmural pressure recordings.

The e-band was simply realized by one liquid-metal based strain sensor and two medical-grade stainless-steel electrodes compacted in five layers of ultra-thin silicone elastomer films. It was fabricated by the techniques of silicone thin film transfer, UV laser cutting, screen printing, and microfluidic filling in a fashion of low cost, fast turning rate, and clean-room free.

The e-band was pre-strained, wrapped around, and partially anchored on small intestine segments to form a closed loop. It was proved to be compliant to the GI tract. Electrical stimulation with various amplitudes of biphasic current pulses has induced different levels of contraction movement that was concurrently monitored by the strain sensor for transmural pressure recordings. Concurrent measurement of the electrical activity of SMCs and the mechanical movement of tissues has been demonstrated by the two stainless-steel electrodes for electromyography (EMG) and tissue impedance measurement, and the strain sensor for transmural pressure monitoring,

respectively. Slow waves, spikes, and corresponding contraction movement of the SMCs have been observed in EMG and transmural pressure recordings.

In conclusion, an implantable, stretchable, and conformal GI neuromuscular stimulator with concurrent measurement of transient electrical and mechanical responses has been demonstrated on slaughtered and neuroactive porcine small intestine segments.

The dissertation of Pei-Shan Chung is approved.

Benjamin M. Wu

Dino Di Carlo

Yongjie Hu

Pei-Yu Chiou, Committee Chair

University of California, Los Angeles

2021

CONTENTS

LIST OF FIGURES

LIST OF TABLES

ACKNOWLEDGEMENTS

It has been an extremely challenging and precious experience and journey working towards my Ph.D. degree in Bioengineering at the University of California, Los Angeles. I want to express my sincere gratitude to all who have provided invaluable guidance, advice and support to help me grow and overcome all the obstacles in the past six years and two months.

First and foremost, I would like to express my deepest appreciation to my advisor, Professor Pei-Yu Chiou for his guidance and unwavering support. He equipped me with creative and brave mindsets, solid foundation in knowledge and fabrication techniques, and critical thinking and problem-solving skills. He gave me a huge encouragement and trust that motivate me to embrace challenges, to deal with bottlenecks within projects, and to step out of the comfort zone. His central idea is "simple is the best" and his pet phrases include "you know what" followed by his new and creative ideas, "don't just follow what PI asks you to do" and "know what you're doing" when students being confusing about their work, and "work smart is always better than work hard" to encourage students to think more before wasting time, effort and money on experiment and costly clean-room fabrication. His passion and persistence in creating truly innovative ideas that have significant impact to the society greatly encourage me to set higher goals and self-requirements.

VITA

Education

2015 – 2017   M.S., Bioengineering

University of California, Los Angeles, CA

2011 – 2013   M.S., Electronics Engineering

National Taiwan University, Taipei, Taiwan

2007 – 2011   B.S., Electrical Engineering

National Taiwan University, Taipei, Taiwan

Publications and Presentations

Zhu, X., Man, T., Tan, X. H. M., **Chung, P. S.,** Teitell, M. A., & Chiou, P. Y. (2021). Distributed colorimetric interferometer for mapping the pressure distribution in a complex microfluidics network. *Lab Chip*, *21*(5), 942-950.

Wang, B., Wen, X., Cao, Y., Huang, S., Lam, H. A., Liu, T. L., **Chung, P. S.**, Monbouquette, H. G., Chiou, P. Y., & Maidment, N. T. (2020). An implantable multifunctional neural microprobe for simultaneous multi-analyte sensing and chemical delivery. *Lab Chip*, *20*(8), 1390-1397.

Man, T., Zhu, X., Chow, Y. T., Dawson, E. R., Wen, X., Patananan, A. N., Liu, T. L., Zhao, C., Wu, C., Hong, J. S., **Chung, P. S.**, Clemens, D. L., Lee, B. Y., Weiss, P. S., Teitell, M. A., & Chiou, P. Y. (2019). Intracellular Photothermal Delivery for Suspension Cells Using Sharp Nanoscale Tips in Microwells. *ACS Nano*, *13*(9), 10835-10844.

Tung, K. W., **Chung, P. S.**, Wu, C., Man, T., Tiwari, S., Wu, B., Chou, Y. F., Yang, F. L., & Chiou, P. Y. (2019). Deep, sub-wavelength acoustic patterning of complex and non-periodic shapes on soft membranes supported by air cavities. *Lab Chip*, *19*(21), 3714-3725.

Wen, X., Wang, B., Huang, S., Liu, T. L., Lee, M. S., **Chung, P. S.**, Chow, Y. T., Huang, I. W., Monbouquette, H. G., Maidment, N. T., & Chiou, P. Y. (2019). Flexible, multifunctional neural probe with liquid metal enabled, ultra-large tunable stiffness

for deep-brain chemical sensing and agent delivery. *Biosens Bioelectron*, *131*, 37-45.

Deng, C. Z., Fan, Y. J., **Chung, P. S.**, & Sheen, H. J. (2018). A Novel Thermal Bubble Valve Integrated Nanofluidic Preconcentrator for Highly Sensitive Biomarker Detection. *ACS Sens*, *3*(7), 1409-1415.

Fan, Y. J., Deng, C. Z., **Chung, P. S.**, Tian, W. C., & Sheen, H. J. (2018). A high sensitivity bead-based immunoassay with nanofluidic preconcentration for biomarker detection. *Sensors and Actuators B: Chemical*, *272*, 502-509.

Chow, Y. T., Man, T., Acosta-Velez, G. F., Zhu, X., Wen, X., **Chung, P. S.**, Liu, T. L., Wu, B. M., & Chiou, P. Y. (2018). Liquid Metal-Based Multifunctional Micropipette for 4D Single Cell Manipulation. *Adv Sci (Weinh)*, *5*(7), 1700711.

Wu, C., Zhu, X., Man, T., **Chung, P. S.**, Teitell, M. A., & Chiou, P. Y. (2018). Lift-off cell lithography for cell patterning with clean background. *Lab Chip*, *18*(20), 3074-3078.

Chow, Y. T., Man, T., Acosta-Velez, G. F., Zhu, X., Wen, X., **Chung, P. S.**, Leo Liu, T., Wu, B. M., & Chiou, P.-Y. (2018). *Rapid fabrication of multifunctional microcapillary for four-dimensional single cell manipulation* 2018 IEEE Micro Electro Mechanical Systems (MEMS),

Chung, P. S., Fan, Y. J., Sheen, H. J., & Tian, W. C. (2015). Real-time dual-loop electric current measurement for label-free nanofluidic preconcentration chip. *Lab Chip*, *15*(1), 319-330.

Lee, W. H., You, M. L,, Wei, P. K., **Chung, P. S.**, Lee, K. L., & Tian, W. C. (2015). *Ultra-sensitive and label-free biosensors using surface plasmon resonance of nano-grating structure in nanofluidic preconcentrator* 2015 Ieee Sensors.

Chung, P. S., Fan, Y. J., Tian, W. C., & Sheen, H. J. (2015). Design principle of nanofluidic concentration by vortex simulation and validation. 5th International Conference on Optofluidics, Optofluidics 2015, Taipei, Taiwan. (Best paper award)

Chung, P. S., Fan, Y. J., Sheen, H.J., & Tian, W. C. (2014). A Rapid Protein Preconcentration Monitoring without Fluorescent Labeling by Dual-Loop Current Measurement Method. Biosensors 2014, Melbourne, Australia. (Best poster award)

Chung, P. S. (2013). Development of Label-free Nanofluidic Preconcentration Chip by Loop Currents Monitoring for Immunoassay Application [Master thesis, Nation Taiwan University]. Taiwan.

Chung, P. S., Liu, Y. L., Liao, K. P., Fan, Y. J., Sung, K. B., Sheen, H. J., & Tian, W. C. (2013). Label-free nanofluidic preconcentration with multi-operational modes by loop currents monitoring for biological application. 17th International Conference on Miniaturized Systems for Chemistry and Life Sciences, MicroTAS 2013, Freiburg, Germany.

Chapter 1 Introduction

This chapter introduces the state-of-the-art in the fields of stretchable electronics and bioelectronic interfaces for the gastrointestinal tract. Current progress and future challenges are discussed.

1.1 Stretchable electronics

The interest of soft, flexible, and stretchable electronics has been driven by the huge demand for wearable, intelligent, and integrated electronic devices for health care, energy, and military purposes [1], as shown in Figure 1.1 (a). The development trends involve the innovation of stretchable mechanical designs, intrinsically stretchable and conductive materials, and practical fabrication strategies.

Stretchable electronics are generally achieved by engineering shapes of hard materials, such as metallic conductors and plastic insulators. Design strategies apply the shape deformation of in-plane and out-of-plane curved structures upon application of force to enhance stretchability. To realize the stretchability, the in-plane structures, such as in-plane serpentine structures [2] and fractal designs [3, 4], and kirigami configurations [5], experience out-of-plane buckling during stretching, while the out-of-plane structures, such as out-of-plane serpentine structures [4] and origami configurations [6], are flattened during stretching, as shown Figure 1.1 (b).

On the other hand, soft stretchable electronics have immense applications due to their high degree of conformity to curvilinear surfaces, ability to withstand high strains, and cost-effective

fabrication alternative to lithography-based approaches. A wide range of intrinsically stretchable and conductive materials could be made by liquid metal [7], ionic liquids [8] and ionic gels [9, 10], conductive polymer [11], and metallic nanoparticle-filled elastomer [1, 12] in company with curved structures [13, 14], as shown in Figure 1.1 (c). Various printing methods have been developed [15], including screen-printing [16, 17], stencil printing [12, 18] and inkjet printing [19].

Strenuous efforts have been made to develop practical applications and realize the stretchability, electrical stability, and cost-efficiency for stretchable electronics. Simple approaches and strategies are desired to achieve higher technical level and overcome challenges to be instrumental in high-throughput manufacturing.
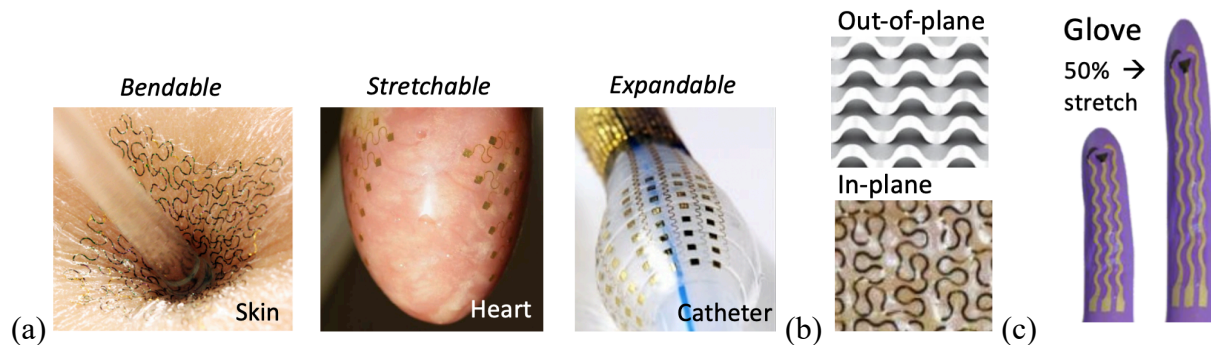
Figure 1.1 Stretchable electronics. (a) Stretchable wavy structures for biological application. (b) In-plane and out-of-plane wavy structures. (c) Intrinsic stretchable and conductive material printed on gloves.

1.2 Bioelectronic interfaces for gastrointestinal tract

The Bioelectronic interfaces apply electrical engineering principles to advance the fundamental concepts of biology, medicine, behavior, or health, and create knowledge for the molecular to the organ system levels, such as brain [20] and nervous system [21], cardiovascular

system [4], skin and musculoskeletal system [4], and gastrointestinal tract [22]. Innovative devices have been developed for the prevention, diagnosis, and treatment of disease for patient rehabilitation and for improving health.

These interfaces operate in a variety of manners and utilize detectors, sensors, stimulators, transducers, and micro-channels to detect physical presences, such as chemicals and gases, to sense physical, optical, or electrical properties, such as temperature, pressure, motion, light intensity, and bioelectrical activity, to apply electrical pulses for electrotherapy, to convert physical energy to electrical energy or vice versa, such as ultrasonic, magnetic, and power transducers, and to deliver fluids or drugs for disease treatment.
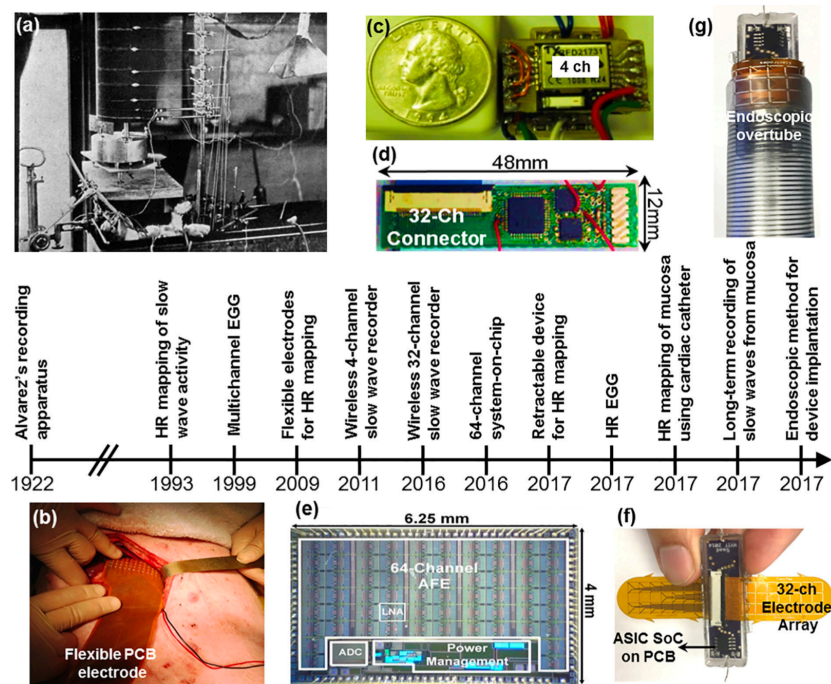
Figure 1.2 Timeline of selective major milestones in gut bioelectronic interfaces [22]

3

Further technological developments on bioelectronic interfaces for the gastrointestinal tract are required to allow effective treatment and minimally invasive implantation that are safely prepared for human use. Timeline of selective major milestones in gut bioelectronic interfaces is shown in Figure 1.2. In the following sections, bioelectronic interfaces focusing on gastrointestinal tract are introduced.

1.2.1 Electroceuticals

Over the past few decades, electroceuticals have attracted considerable attention as a novel therapeutic modality. The electroceuticals for the gastrointestinal tract hold significant potential to treat gastrointestinal disorders such as malabsorption, dysmotility, and related disorders, such as metabolism, inflammation, and infection. Different forms of electrical stimulations have been developed for GI tract, including transcutaneous stimulation, electroacupuncture stimulation, implanted stimulation system, nerve cuff stimulation, and magnetic stimulation. [23].

Stimulation parameters, such as waveform, amplitude, frequency, pulse width, duty cycle, and pulse train (on-time and off-time) [24], render the stimulation mechanism and performance differently on stomach [25] and intestines [26], as shown in Figure 1.3. In general, pacing with pulse widths of up to 1 millisecond trigger neural excitation and result in symptomatic improvement with no influence on gastric contractions, while pacing with longer pulse widths of up to 1 second induce muscle contraction and repair damaged interstitial cells of Cajal (ICCs). High frequency pulses prohibit a refractory period for cells to reset before re-excitation and hence are used to block signal transmission through nerve bundles [23].
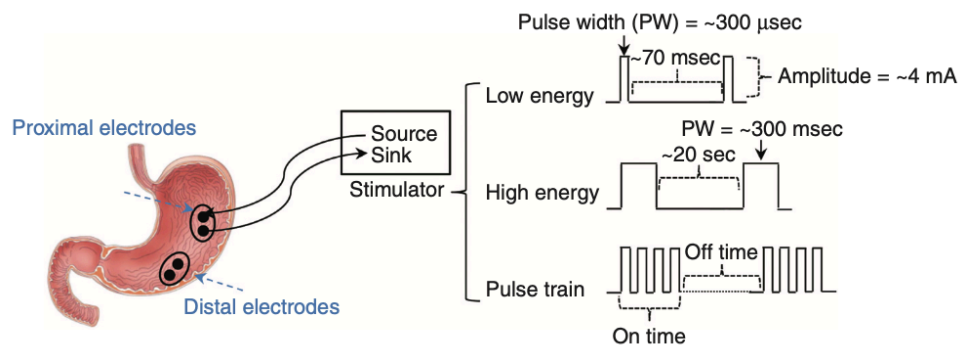
Figure 1.3 Electrotherapy for stomach [24]

Reported effects of single-site and multiple-site electrical stimulation have enhanced motor functions in stomach, such as improved emptying, normalization of dysrhythmia, reduction in vomiting and nausea, and decrease intake of food, in small intestine, such as delayed or accelerated transit, and enhancement or inhibition of water and nutrient intake, and in large intestine, such as delayed transit, and displacement of semisolid colon content [27]. In commercial products, Medtronic's Enterra II won FDA approval under humanitarian device exemption (HDE) provision to treat chronic, intractable, and drug resistant nausea and vomiting resulting from gastroparesis in 2015, and Medtronic's Interstim received FDA approval to treat accidental bowel leakage or fecal incontinence in 2011.

Various types of non-invasive and invasive electrodes have been developed for neuromuscular stimulation and recording [24], as shown in Figure 1.4. Non-invasive abdominal surface electrodes are placed on skin for transcutaneous electrical stimulation (TES) and electrogastrography (EGG) [28]. The effects of TES on bowel movement require further examination [29]. Three invasive electrode types are classified by their location, including extraluminal surface electrodes, extraluminal and intramuscular serosal electrodes, and intraluminal surface electrodes. An array of extraluminal surface electrodes embedded on

biocompatible flexible substrate can record large-area surface electromyography (sEMG) to map the slow wave of stomach [30] and intestines [31, 32], and to provide electrotherapy on intestines [33, 34]. Extraluminal and intramuscular electrodes, so-called serosal electrodes, such as hook needle electrodes, can be inserted and affixed in the serosal layer for electrical stimulation and intramuscular electromyography (iEMG) [25, 35]. Intraluminal surface electrodes, such as clip electrodes [36], suction electrodes, and ring-shaped electrodes [37], are anchored on or contacted to the mucosal layer to record intraluminal surface electromyography. No significant difference has been observed between the effects induced by extraluminal stimulation and intraluminal stimulation [24, 27].

Location
- Intracellular recording
- Extracellular recording
- Intramuscular electrode
- Surface electrode

Configuration
- Monopolar electrode
- Bipolar electrode
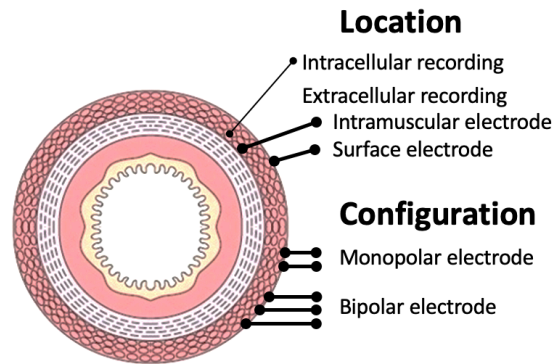
Figure 1.4 Electrode types and configurations

Some crucial milestones that must be achieved for the widespread implementation of GI electrotherapy include but not limit to the optimization of electrical stimulation parameters and the technological developments on implantable high-energy wireless devices with close-loop feedback control of intestinal motility [23, 35].

1.2.2 Electrophysiology recordings

The electrical activity in the GI tract is a complex collaboration and communication of multiple cells, including enteric neurons, interstitial cells of Cajal (ICC), and smooth muscle cells, as shown in Figure 1.5. Majority of ICC reside alongside the myenteric plexus and in the space between longitudinal and circumferential smooth muscle cells. These CIC act as neuromuscular apparatus to convert neural signal from enteric motor neurons and generate intrinsic electrical rhythm in smooth muscle cells [38]. The rhythmic depolarizations of the membrane potential, also known as slow waves, propagate through the GI tract. If the depolarization of membrane potential is activated along with neural and chemical control activities, it exceeds a certain threshold potential and trigger action potentials or so-called spikes and contractile movement until the repolarization of the membrane potential. These slow waves and spikes activities can be recorded by intracellular electrodes and extracellular electrodes, and are decoupled by filtering the signal between 0-0.3 Hz and 5-10 Hz, respectively [39, 40]. Other filtering parameters are also adopted [31, 32].

General structure of the gut wall
1: *Mucosa:* Epithelium
2: *Mucosa:* Lamina propria
3: *Mucosa:* Muscularis mucosae
4: Lumen
5: Lymphatic tissue
6: Duct of gland outside tract
7: Gland in mucosa
8: *Submucosa*
9: Glands in submucosa
10: Meissner's submucosal plexus
11: Vein
12: *Muscularis:* Circular muscle
13: *Muscularis:* Longitudinal muscle
14: *Serosa:* Areolar connective tissue
15: *Serosa:* Epithelium
16: Auerbach's myenteric plexus
17: Nerve
18: Artery
19: Mesentery

Figure 1.5 General structure and neuromuscular communication of gut wall [41]

These myoelectric activity recordings of slow waves and action potentials in gastrointestinal muscles appear in a various types, frequencies, and waveforms [39, 40, 42, 43]. For example, the depolarization of slow waves from extracellular recordings is a derivative of the transmembrane potential recorded by the intracellular electrodes [44], as shown in Figure 1.6 (a). In fact, the variability of the recordings comes from different animal specimen (stomach vs. small intestine vs. colon), electrode positioning (intracellular vs. intramuscular vs. surface), recording techniques (unipolar vs. bipolar), interelectrode distances (global vs. local), alignment direction of recording electrodes (longitudinal vs. circumferential), electrode performance (macroelectrode vs. microelectrode), noise (inherent noise in electronics equipment, electromagnetic radiation, motion artifacts, inherent instability of EMG signal, etc.), circuit designs (differential amplifiers, filters, rectifiers, smoothing circuits, inverters, level shifters, etc.) and data processing [44-46]. Table 1.1 shows some of the current bioelectronic interfaces on the gastrointestinal tract.

8

(b)

E
TC = 0.1
LCF = 9.6 c/min

E
TC = 0.8
LCF = 1.2 c/min

E
DC

SG

E
TC = 0.1
LCF = 9.6 c/min

E
TC = 0.8
LCF = 1.2 c/min

E
DC

SG

15 sec   0.4 mV

A

E1-20   0.1 mV
E2-15   0.2 mV
E3-10   0.4 mV
E4-5   1.0 mV
E5-0   0.4 mV

B

SG1-20   1.0 mV
SG2-15   1.0 mV
SG3-10   1.0 mV
SG4-5   1.0 mV
SG5-0   1.0 mV

30 sec

(c)

E1 (RAW)   0.4 mV

E1 (0-0.3 Hz)   0.2 mV

1 min

E1 (5-10 Hz)   0.04 mV

SG1   1 mV

(d)

9

(e)
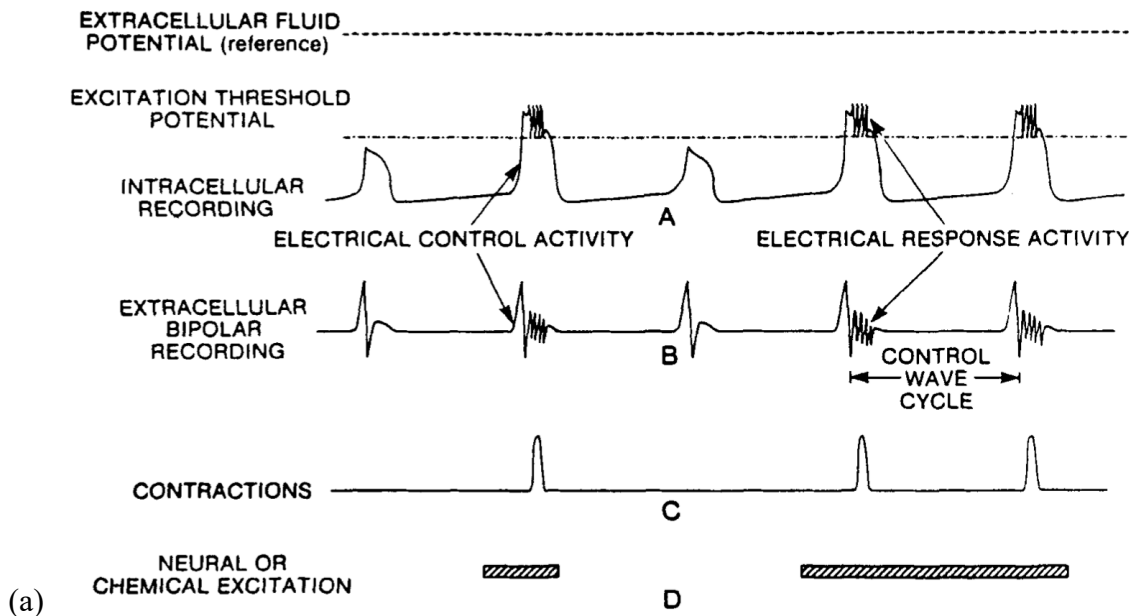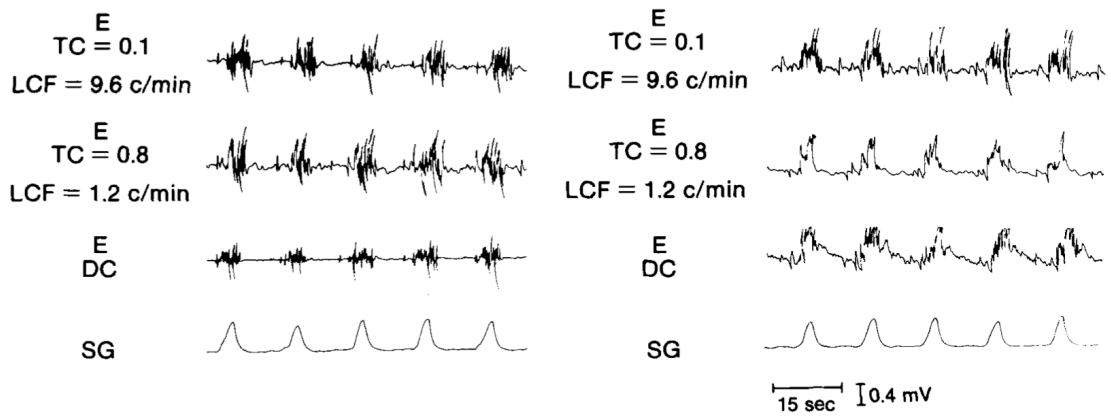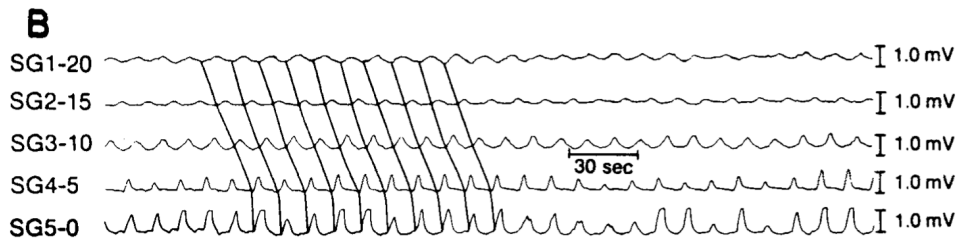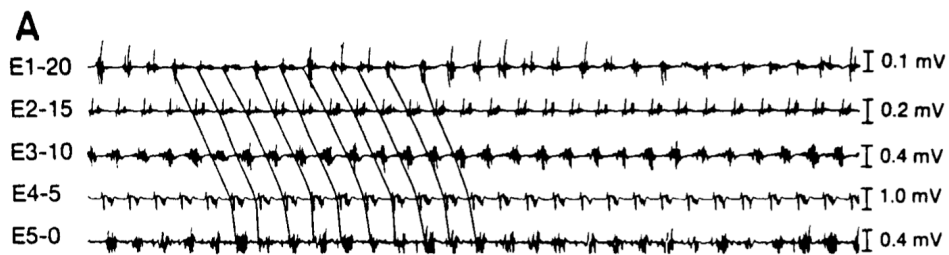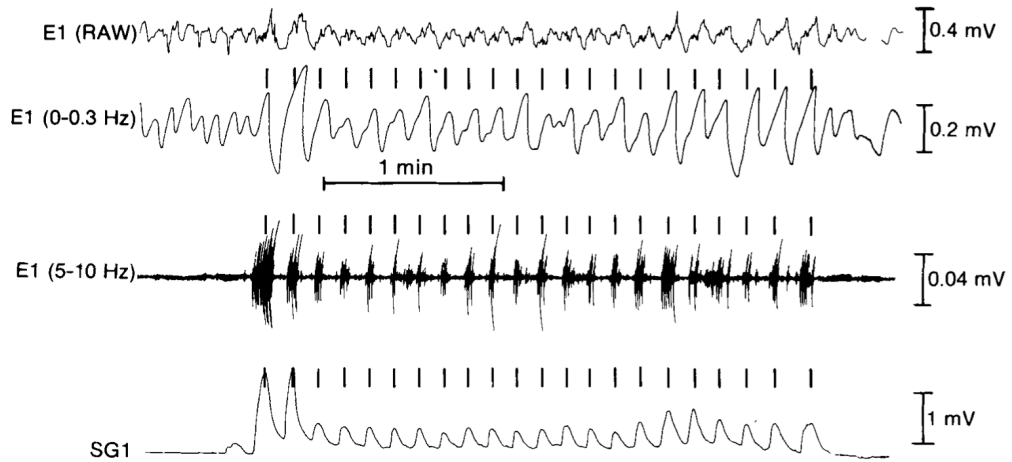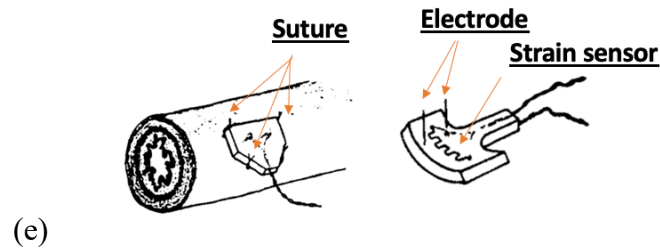
Figure 1.6 Electrical physiological recordings of the gastrointestinal tract [42]. (a) Intracellular and extracellular recordings of myoelectric activity. (b) Bipolar and monopolar recordings of myoelectric activity. (c) Propulsive movement recordings via an array of electrodes and transducers. (d) Filtering of myoelectric activity. (e) Installation of needle electrodes and serosal strain gauge transducers on the GI tract.

Table 1.1 Selective review on bioelectronic interfaces
for myoelectric activity recordings, neuromuscular electrical stimulation, and tissue mobility

Year	Authors	Specimen	Recording technique	Electrode type	Electrode number	Electrode distance	Recording direction	Myoelectric signal recording & filtering	Stimulation (amp, pulse width, freq)	Mobility recording	Ref
1983	El-Sharkawy	Dog colon	Unipolar pseudo-intracellular electrode	Suction electrode	-	-	-	Slow wave, spikes	No	Stain gauge	[47]
1986	Schang, Pilote, et al	Human sigmoid colon	Bipolar intraluminal surface electrode	Ag/AgCl ring-shaped wires	3 pairs	Interelectrode 1 cm, spacing 15 cm	Longitudinal	Spikes	No	Intraluminal pressure and flow sensor	[37]
1986	Sarma.	Dog colon	Bipolar intramuscular electrode	Needle	4 pairs	Interelectrode 7 mm, spacing 12.5 cm	Longitudinal	Slow wave (0-0.3 Hz), spikes (5-10 Hz)	No	Stain gauge	[48]
2009	Aelen, Mintchev, et al	Dog stomach	Intramuscular electrode	Stainless-steel wires	2 pairs	Spacing 3-4 cm	Circumferential	No	Biphasic voltage pulse (10 Vpp, 10 ms, 50 Hz)	Strain gauge, tissue impedance	[25]
2018	Lo, Liu, et al	Rodent & porcine colon	Surface electrode	Platinum microelectrodes on flexible PCB	6	Interelectrode 3.3 mm	Longitudinal	No	Biphasic current pulse (1 mA, 1 ms, 100 Hz)	Tissue impedance	[33]
2018	Angeli, Cheng, et al.	Human proximal jejunum	Unipolar surface electrode	Microelectrodes on flexible PCB	256	Interelectrode ~5 mm	Longitudinal, circumferential	Slow wave propagation (0-30 Hz, median filter, polynomial fitting)	No	No	[31]
2019	Abraham, et al	Rabbit small intestine	Unipolar surface electrode	Gold microelectrodes on flexible PCB	256	Interelectrode 4 mm	Longitudinal, circumferential	Slow wave propagation (0-2 Hz, median filter, polynomial fitting)	No	No	[32]
2019	Wang, Liu, et al	Porcine colon	Surface electrode	Platinum microelectrode on flexible PCB	6	Interelectrode 3.3 mm	Circumferential	No	Biphasic current pulse (2 mA, 2 ms, 100 Hz)	Tissue impedance	[34]
2019	Dubrovsky, Dunn, et al	Porcine jejunum	Surface electrode	Platinum microelectrode on flexible PCB	4	Interelectrode 3.3 mm	Longitudinal	No	Biphasic current pulse (2 mA, 2 ms, 100 Hz)	Tissue impedance	[49]
2020	Liu, Chen, et al	Rat small intestine	Bipolar intramuscular electrode	Needle	3 pairs	Interelectrode 0.5 cm	-	Slow wave	No	No	[50]
2021	Chung, Chiou, et al	Porcine small intestine	Bipolar surface electrode	Stainless-steel electrodes on stretchable elastics	2 pairs	Interelectrode 1.8 cm, spacing 1 cm	Longitudinal, circumferential	Slow wave (rectification, integration, 0-2 Hz)	Biphasic current pulse (5 mA, 2 ms, 100 Hz)	Stretchable strain sensor, tissue impedance	This work

The myoelectric activity recording techniques include unipolar or monopolar electrode arrangement and bipolar electrode arrangement, as shown in Figure 1.4. The unipolar electrode arrangement has two electrodes, including one recording electrode (V) placed on the muscle of interest and one indifferent or reference electrode (GND) placed at some distance to the recording electrode, and is coupled with a differential amplifier where the difference signal between the two electrodes (V-GND) is amplified. While the bipolar electrode arrangement has three electrodes, including two recording electrodes (V1, V2) aligned with the muscle fiber direction or electrical waves and one reference electrode (GND) placed at some distance to the recording electrodes, is coupled with a differential amplifier where the difference signal (V1-V2) between the two electrodes with respect to the reference electrode is amplified. The advantage of the unipolar electrode arrangement is that it preserves authentic EMG signal and provide a global view on the activity of a muscle, but is very sensitive to electromagnetic noise. By contrast, the bipolar electrode arrangement cancels out common signals, such as electromagnetic noise, motion artifacts, as well as the amplitude of the bipolar EMG signal, and leads to a local view on the activity of a muscle in a high spatial fashion [45, 51, 52].

Electrodes are positioned either intracellularly (in cells) or extracellularly (in tissue or on surface of tissue). For intracellular recordings, micro-electrodes impale smooth muscle cells to record transmembrane potentials. Since the impalement of the cells is hard to maintain during experiment, alternatively, suction electrodes [47] and the sucrose gap technique are used to measure pseudo-transmembrane potentials. Quantitative electrical properties of slow waves and spikes are examined [44]. For extracellular and intramuscular recordings, also known as intramuscular electromyography (imEMG), serosal, needle, or wire electrodes are inserted into tissue to record deeper muscles' electrical activities [46]. Qualitative electrical properties of slow

waves and spikes of cells adjacent to the electrodes are recorded successfully [48, 50]. For extracellular surface recording, also known as surface electromyography (sEMG), surface electrodes are attached on the surface of the tissue to record superficial muscles' electrical activities. A large number of surface electrodes has been used to determine the origin and pattern of the propagation of slow waves with high-resolution mapping [31, 32]. Some irregularity of waveform from extracellular recordings may be observed and can be explained by difference in intrinsic frequency of slow waves recorded simultaneously from a large number of uncoordinated cells [42].

The motion artifacts are the key contaminant of electrophysiological recording. Unlike wet electrodes, such as Ag/AgCl electrodes, benefit from low interface impedance with good signal stability and reducibility before drying out. Dry electrodes, such as stainless-steel electrodes, are used for long-term recordings but suffer from motion artifacts. The relative motion between the electrode and tissue changes the ionic concentration near the electrode surface and results in a potential difference. Movements less than 50 um can produce the same amplitude as signals reputed to be slow waves [44]. Hence, decrease in the relative movement at electrode-tissue interface is essential for future direction.

1.2.3 Motility monitoring

Several techniques exist for measurement of gastrointestinal motility in vivo by means of invasive or non-invasive and intraluminal or extraluminal fashions, as shown in Figure 1.7 and Table 1.2.

In non-invasive approaches, ultrasonography can be used to visualize motility in some areas of the GI tract, such as stomach, pylorus, and duodenum. Radiography based on X-rays and

CT mainly visualizes the emptying of stomach. It requires a contrast medium mixed with a meal and is radiation hazard. Some edible liquid and solid markers, such as dyes and heavy metal ions, are used for the visualization of bolus transit and the measurement of flow rate and transit time. Besides, wireless motility capsule (2.6 cm x 1.1 cm) has demonstrated the function of pH, pressure, and temperature sensing and the analysis of transit time throughout the GI tract [53].
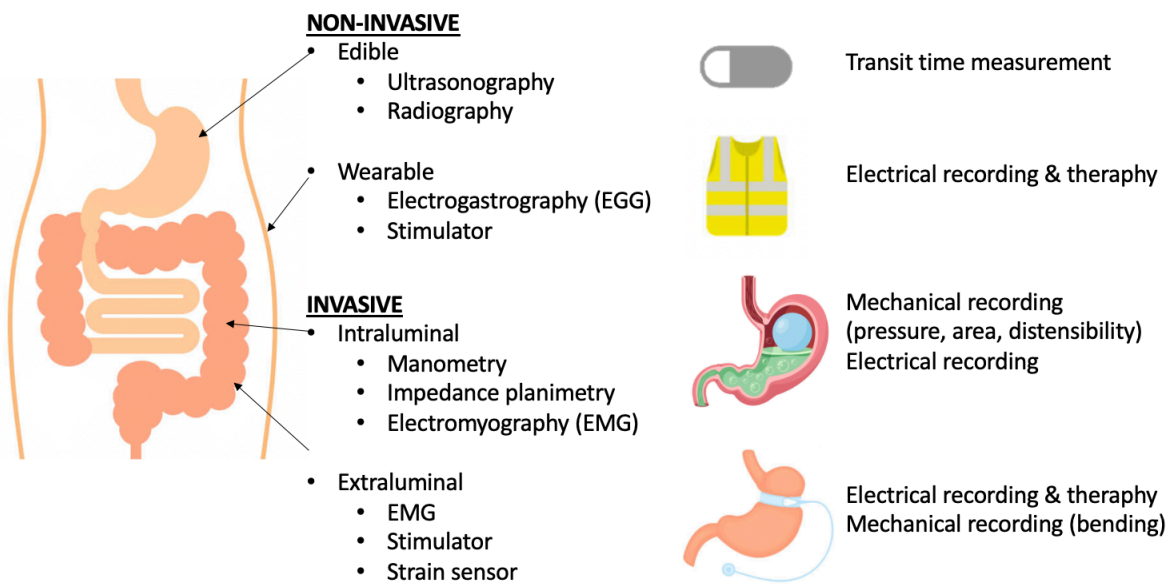
Figure 1.7 Existing bioelectronic interface in the gastrointestinal tract

Table 1.2 Techniques for tissue motility monitoring in the gastrointestinal tract

	Intraluminal	Extraluminal
Invasive	Colonic manometry [54-56]	Serosal strain gauge transducers [25, 47, 48, 59]
	Impedance planimetry [57, 58]	Impedance spectroscopy [25, 33, 34, 49]
Non-invasive	Liquid and solid markers [57]	Ultrasonography & Radiography [57]
	Electronic capsule [53]	Electrogastrography (EEG)

In invasive approaches, serosal strain gauges transducers are sutured on the gastrointestinal wall and utilize the change of curvature of the wall at the location of the transducers to address the contraction movement [25, 47, 59]. They are typically a serpentine pattern of metal wire embedded in flexible polyimide films and sutured on gastrointestinal wall with the serpentine pattern aligned to the longitudinal direction to measure the bending in that direction. The bending of the strain gauges results in the resistance change and an analog bridge amplifier is required to amplify the small difference of electric resistance.

Colonic manometry is commonly used for intraluminal colonic pressure recording and can be characterized by three types of measuring techniques, including perfusion systems [60], strain gauges [56], and pressure-sensitive fiber Bragg gratings [55, 61]. In general, overnight fasting, bowel cleaning and tap water enema are administered before the recording. In the perfusion systems, a channel with a side hole is perfused at a constant rate. The fluid flows through a transducer in the channel and into the lumen of colon. When a contraction occurs nearby the side hole of the channel, the flow in the channel is obstructed by the counter pressure or intraluminal pressure from the fluid inside the lumen. The pressure is then transmitted via the channel to the transducer. In the strain gauges techniques, several strain gauges are freely placed inside the lumen of colon, taped securely on the gluteal region of the body, and connected to a portable data recorder. An ambulatory 24-hour colonic manometry has been demonstrated [56]. Recently, high-resolution fiber-optic manometry is used to monitor real-time colonic intraluminal pressure. 36 fiber Bragg grating structures arranged along a fiber with at least 1 cm spacing has been demonstrated for the recording and analysis of complex motor patterns in colon [55], as shown is Figure 1.8. Basically, light is transmitted thorough an optical fiber and reflected at locations of fiber Bragg grating structures. The reflected power spectrum is a function of wavelength and is varied by the spacing

of the grating structures. Localized pressure can cause the distortion of the fiber as well as the spacing of the grating structures and hence the wavelength at the maximum reflected power shifts [55, 61]. The implantation of these colonic manometry may cause luminal obstruction and trigger peristaltic reflexes [55].

The purpose of both the intraluminal impedance planimetry and extraluminal impedance spectroscopy relate the impedance changes to the deformation of tissue. In intraluminal impedance planimetry, two electrodes are anchored either inside the wall of a conductive liquid-filled balloon in the lumen or just placed inside the lumen without a balloon. The distance between the two electrodes changes during the contraction and distention of the balloon and colon, and results in the changes of impedance through conductive liquid [57, 58]. Instead of measuring the impedance change through conductive liquid, extraluminal impedance spectroscopy records the impedance change of two electrodes through GI tissue and relates the motility to the impedance. For those electrodes sutured on tissue, since they are moving along with tissue, impedance decreases during contraction [25]. By contrast, for those electrodes fabricated on flexible plastics, the distance between two electrodes stays constant. Since the length of the path that the electrical current flows along extends between the two electrodes, impedance increases during contraction [33, 34, 49].
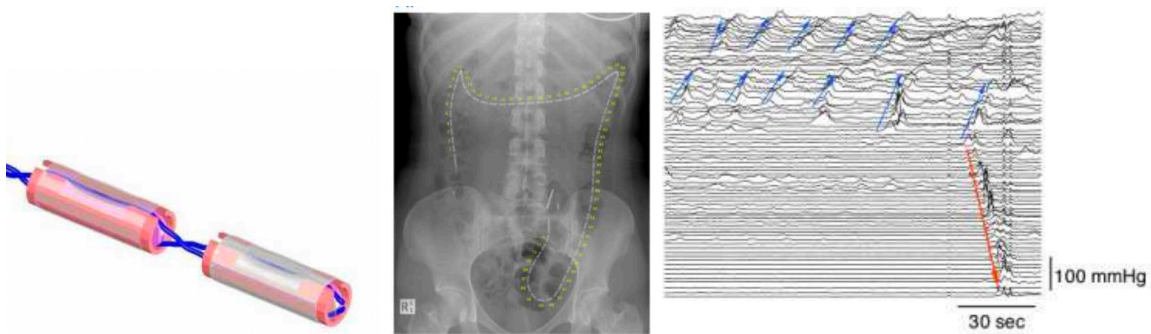
Figure 1.8 Fiber-optic manometry for colonic intraluminal pressure recording [55]

16

Therapeutical bioelectronics requires the electrical stimulation and the feedback control of the motility. Long-term and ambulatory technology on the motility recording of the gastrointestinal track is essential for future direction, as shown in Figure 1.9.
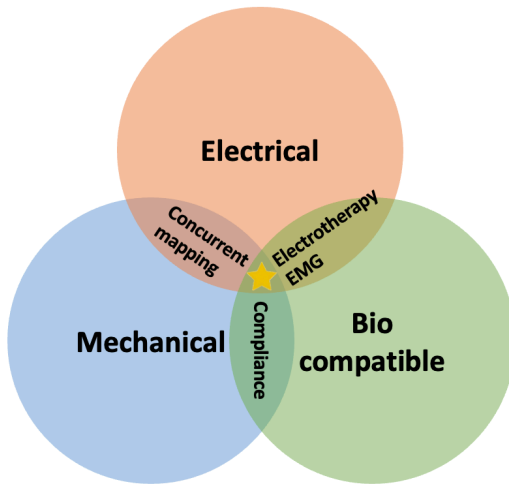
Figure 1.9 Next generation gastrointestinal platforms

1.3 Electrode performance tests

Among a variety of electrode performance testing methods in literature, Asplund et al. proposed a tutorial for standardized electrode performance tests in Nature Protocols, 2020 [62]. This paper critically discussed relevant performance tests for characterization of neural interface electrodes and explained the underlining mechanism of the tests and corresponding limitations. It summarized to a unified standard to promote efficient scientific evaluation and comparison between different materials available in literature. This could improve the transparency and efficiency on the report of the electrode performance to accelerate translation to clinical trials. Different tools are adopted to analyze recording electrodes and stimulation electrode, respectively.

1.3.1 Characterization of recording electrode

For recording electrodes, high-signal-to-noise ratio is desired. To achieve the goal, low resistance at electrode-electrolyte interface is required to reduce thermal noise and allow efficient charge transfer process at the electrode-electrolyte interface. Electrochemical impedance spectroscopy (EIS) is utilized to measure the impedance in a broad frequency band and displays as Bode plot and Nyquist plot.

The Bode plot shows the impedance of the equivalent Randles circuit at different frequencies. In general, impedance of electrode-electrolyte interface is lower at higher frequency and vice versa. Signal with frequency higher than cut-off frequency can pass the interface without attenuation, and therefore, the interface can be seemed as a "high pass" filter. Besides, since the phase does not dramatically shift in this region, signal can authentically transfer without distortion. By contrast, signal with frequency lower than cut-off frequency passes through larger impedance with different amount of phase shift and hence it is attenuated or filtered and experiences non-linear distortion.

In order to accomplish low impedance, one can refer to the impact factors of Pt electrodes [62], as shown in Figure 1.10. The dashed black line and solid black line represent the sputtered polycrystalline Pt electrodes (1 mm diameter) without or with chemically grown nanostructured Pt on surfaces, respectively. In the log-log plot, the impedance decreases at a slope of -45 degree as frequency increases and the cut-off frequency shifts from 1 kHz to 10 Hz. All the colorful lines show the Bode plots with different geometric shapes. It concludes that the increasement of either the electrochemical active area or geometrical surface area can enhance the transfer function of the electrode-electrolyte interface.
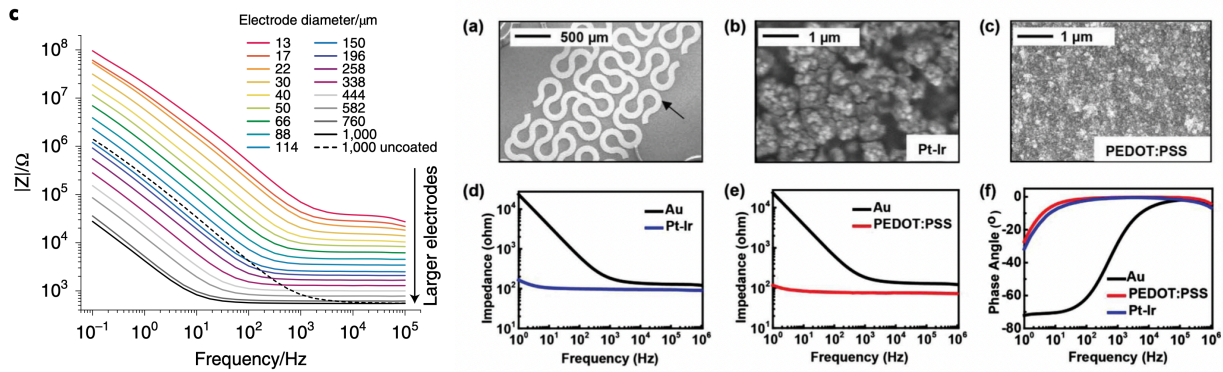
Figure 1.10 Bode plots of different size and surface roughness of metal electrodes [62]

On the other hand, the Nyquist plot is utilized to obtain estimates of some equivalent circuit models with appropriate elements and parameters in the frequency range of interest, as shown in Figure 1.11. Other than ideal resistors and capacitors, Warburg element and constant phase element (CPE) are the suitable components to be applied to equivalent circuit models for the understanding of electrochemical process. Warburg element and constant phase element are equivalent circuit elements that model the diffusion process and the behavior of electrical double layer, respectively. Yielding estimates of components and parameters are crucial if the interface should be load-matched with electrical circuits of a recording amplifier or an electrical stimulator. Details are described in Chapter 2.4.2.
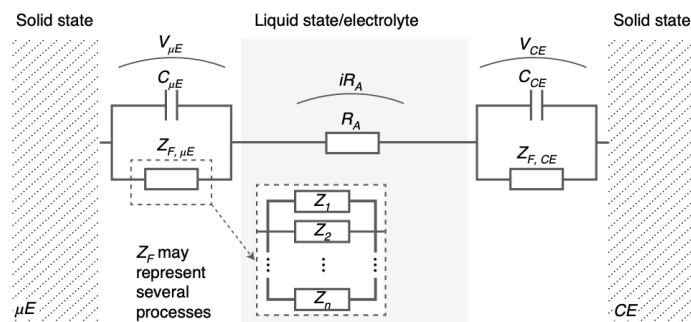
Figure 1.11 Equivalent circuit at the interface of electrode and electrolyte [62]

1.3.2 Characterization of stimulation electrode

For pulse stimulation electrode, safely delivery of required amount of charge across the electrode-electrolyte interface is desired. To achieve the goal, within the pulse duration, the maximum amplitude of the voltage across the electrode double layer should not exceed the activation voltages of water dissociation under either in cathodic or anodic phase. The electrolysis of water is an irreversible faradaic process and results in formation of oxygen and hydrogen gas and substantial pH changes due to the products of protons and hydroxide. Overtime, it could be harmful to surrounding biological tissues and corrode or otherwise deteriorate the electrode surfaces.

The cyclic voltammetry (CV) is utilized to obtain activation voltages of reactants that enter into courses of chemical reactions, and voltage ranges in which solvents are neither oxidized nor reduced. When the voltage across the electrode double layer exceeds the half-cell potentials of reactants, the reactants will be consumed rapidly and the electric current increases. Once the reactants become diffusion limited, the electric current decreases. The characterization voltages of these peaks from different reactions outline an electrochemical signature of the electrode in specific electrolytes, as shown in Figure 1.12 (a). Moreover, if the electrode has high electrochemical active area, the activation voltages shift further away from the origins as the scan rate increases [63]. On the other hand, since the electrolysis of water is mainly kinetically limited in water solution, at its activation voltages, the magnitude of electric current increases exponentially and does not decrease. The range between the activation voltages defines as water window.
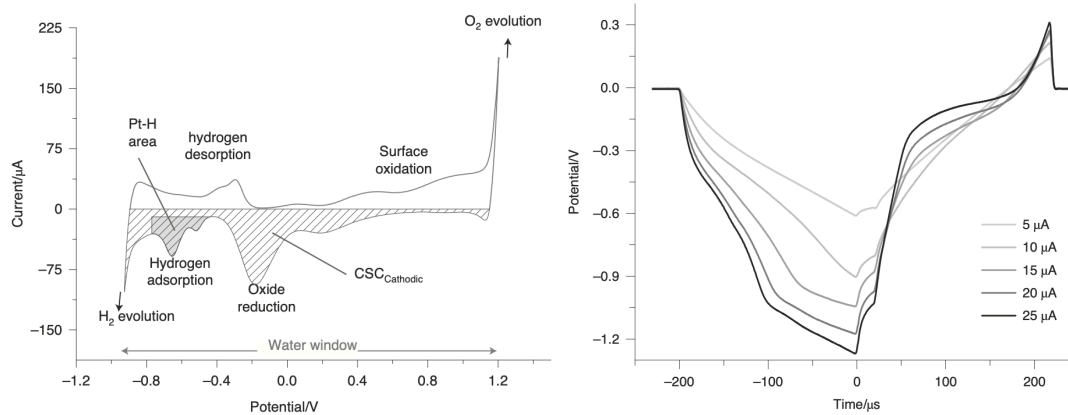
Figure 1.12 Techniques for the evaluation of stimulation equation [62]. (a) Cyclic voltammetry of platinum electrode. (b) Charge injection capacity measured by constant current pulses.

Moreover, the maximum charge injection capacity (CIC) per area is then examined. Given charge-balanced biphasic current pulses with a cathodic first phase to the electrode, the transient voltage profiles across the working electrode and counter electrode are recorded, as shown in Figure 1.12 (b). If the Randles cell model is used to simplify the circuit, we can calculate the theoretical transient voltage and time constant of the circuit, as shown in equation xx. The initial value of the voltage profiles is related to the solution resistant Rs, and the difference between steady-state voltage and initial voltage is related to the charge transfer resistance, Rct. Since the voltage across the electrical double layer is of interest, the voltage profile should take off the voltage drop contributed by the solution resistance and the modified voltage profile should not exceed the water window obtained from the CV curve. The maximum current set so that the voltage across electric double layer equals to the water window at the cathodic boundary. In the meantime, the anodic phase adjusted in duration so that the charge balance is secured and the

21

voltage is smaller than the water window at the anodic boundary. Details are described in Chapter 2.4.2.

1.3.3 Stability test

Guidelines for standardized electrode performance testing in vitro is summarized in Figure 1.13 [62]. It is required to perform long-term stability tests to predict the performance of the electrode during chronic application by means of the acceleration of aging conditions, such as high temperature, acidic environment, corrosive environment, and repetitive pulse delivery.

Recording electrodes
The most relevant quality parameter related to the performance of recording electrodes is the signal-to-noise ratio (SNR). The analysis method of choice to evaluate this parameter is **electrochemical impedance spectroscopy (EIS)**, performed in phosphate buffered saline (PBS, 0.01 M) as a universal electrolyte facilitating comparison among different materials/studies.
While impedance for a single frequency is commonly reported in the literature, we highly recommend evaluating the full spectrum to be able to determine the complete transfer function of neural electrodes.

Reporting should include:
– electrode area
– f_{cutoff}
– $|Z|_{1kHz}$
Alternatively, the **full Bode plot** should be shown in the frequency range from 1 Hz to 100 kHz.

Electrochemical stability
The stability of an electrode material can be estimated under accelerated aging conditions to predict the performance during chronic applications. Prior to, during (for separate samples) and after such aging experiments, the fundamental electrode characteristics should be documented by:
– **EIS**
– **CV**
– **High-resolution imaging**

Aging conditions:
– PBS at 37 °C (real time aging)
– PBS at 60 °C (accelerated aging)
– PBS at 37 °C (60°C) + 30 mM H_2O_2 (modeling a corrosive environment)
Reporting should include:
– Stability over >x days, evidenced by:
  • Δf_{cutoff}, ΔZ_{1kHz}
  • Bode plot + imaging before and after
    • real-time aging
    • accelerated aging

Stimulation electrodes
Stimulation electrodes are characterized by their ability to deliver charge safely across the electrode/electrolyte interface. The charge injection capacity (CIC) is evaluated by the **pulse test** or, alternatively, the **pulse-clamp method**.
Prior to exposing an electrode to biphasic current pulsing, the water window should be determined using CV so that safe charge injection (i.e., the maximum CIC) can be determined with respect to the water window. Typical pulse features are:
– biphasic current
– charge-balanced pulses
– cathodic leading phase
– 200-µs pulse duration
Reporting should include:
– **CIC_{max} per area**
– The **water window** used to define the maximum injectable charge

Stability under stimulation
Long-term pulsing experiments expand the analysis toolset for performance estimation of stimulation electrodes, in particular addressing stability required for chronic applications.
Long-term pulsing is performed using the same pulse parameters as employed for maximum CIC determination. However, this is done at reduced current amplitudes (i.e., to reach 50% of the maximum CIC during consecutive pulsing). Pulsing should be performed over 10^6–10^{10} pulses to reach relevant numbers as employed in chronic applications.

Reporting should include:
– Stability over >x days and number of pulses at Q charge/area, evidenced by:
  • Δf_{cutoff}, ΔZ_{1kHz}, ΔV_{PB}
  • Bode plot + imaging before and after pulsing
– pulse length, shape and frequency
– product of number of pulses and charge/area may serve as total stress estimate for comparison to different studies with different pulsing parameters

Complementary techniques
Additional analysis methods recommended for chemical, physical and morphological electrode characterization are EQCM for analysis of dissolution and SEM, XPS, EDX, XRD and FTIR for analysis of surface changes.

Figure 1.13 Guidelines for standardized electrode performance testing in vitro [62]

Chapter 2 Microfluidic Platforms for Ultra Stretchable Electronics

2.1 Introduction

Gastrointestinal (GI) pacing for stomach and intestines, analogous to cardiac pacing for heart, has been an emerging therapy to electrically entrain omnipresent bioelectrical activity and stimulate contraction of smooth muscle cells (SMCs), especially for patients who are refractory to medical therapy. For example, commercialized implantable gastric electrical stimulator featuring one electrode and short pulses is effective in treating chronic nausea and vomiting in more than 50% of patients with refractory gastroparesis.[1] Recently, multiple studies have shown pacing parameters, stimulation sites, and numbers of electrodes render effective treatments in gastric, small intestinal, and colonic syndromes [26]. Moreover, the spatiotemporal electric activities of SMCs and intraluminal pressure indicates propagating or non-propagating and rhythmic or sporadic contractions [64]. Hence, the concurrent mapping and tracking of the electrical activities of SMCs and mechanical responses of GI tract can offer essential and quantitative information to interpret and mitigate electrode configurations and pacing parameters, and each corresponding stimulated digestive process [37].

Despite its promising scope, existing technologies for high spatiotemporal measurements of electrical and mechanical responses are still limited. The major limitations are the rigid nature of insertion electrodes and sensors, and the lack of highly stretchable and conformal platforms. To accommodate more than 200% expansion of tissue as compared with its contraction counterparts

[65], rigid insertion electrodes and sensors are typically spaced 4 cm apart, sutured to serosal surfaces, and connected to a neurostimulation system with long connectors, individually [25, 66]. Consequently, they are incapable of capturing the dynamic propagation of mechanical and electrical interactions in a high spatiotemporal fashion. Hence, to fill up the current technology gap, the objective of this research is to develop an implantable, stretchable, and conformal GI neurostimulator to treat different types of GI disorders, which utilizes flexible stimulation configurations with high spatiotemporal and concurrent mapping of transient electrical and mechanical responses.
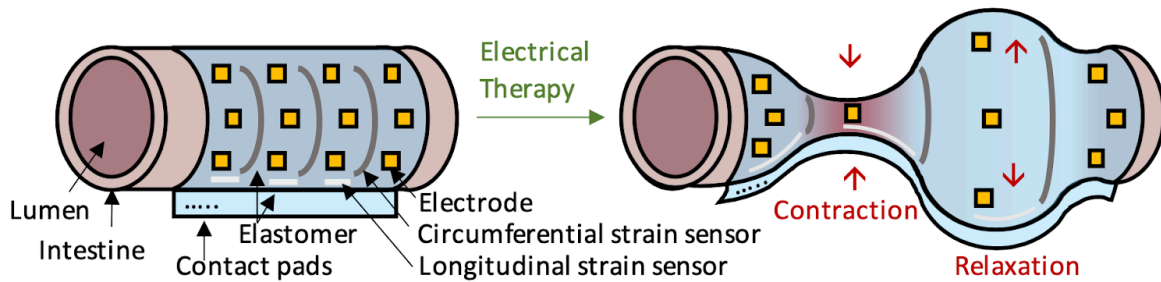
Figure 2.1 Schematic of stretchable and conformal gastrointestinal neurostimulator

The schematic of the proposed neurostimulator is shown in Figure 2.1. The platform utilizes arrays of electrodes and electrical strain sensors on a stretchable and conformal elastomer wrapped around intestines. All the components are connected by stretchable liquid metal wires embedded in the elastomer and linked to contact pads as interfaces to a connector. Sensing and stimulation electrodes are uniformly dispersed in axial and radial directions of the intestine to record electrical activities of SMCs and provide various stimulation configurations, respectively. Since SMCs contract and relax in both radial and longitudinal directions, stretchable strain sensors are designed to measure deformed circumferences and lengths along axial direction. The electronic

system for the platform provides flexible stimulation configurations and concurrent real-time data acquisition. The data will be analyzed to interpret the relation between electrical and mechanical activities. Moreover, based on the mechanical activities, machine learning models will be applied to reverse engineer and predict waveforms of contraction and relaxation for circular and longitudinal SMCs, respectively. This information can further interpret the roles of SMCs involved in the digestive processes, such as segmentation, mixing, and transport.

To summarize, the success of the project will offer a huge impact on the understanding of underlying concurrent electrical and mechanical responses of SMCs and the development of electrical therapy through our GI neurostimulator for different GI disorders.

2.2 Design

An ultra-stretchable electronic elastic band, which we called e-band, is designed to utilize the concurrent recordings of electrical activity of cells and mechanical movement of tissue to provide optimal electrotherapy to gastrointestinal tract. Three functions including electrical stimulation, electromyography and gastrointestinal motility recordings are simply realized by one strain sensor and two electrodes compacted in a single e-band.

2.2.1 Device design

As shown in Figure 2.2, the main body of the e-band is composed of five layers of elastomer films, including, from bottom to top, substrate, a microfluidic channel for strain sensor, vias, two microfluidic channels for two electrodes, and vias. The outline of the e-band is shaped by laser cutting machine after the five layers transferred on water-soluble polymer coated glass slides. The electrode layer is composed of an elastomer film, a layer of silver adhesive, and a

stainless-steel disk, and is transferred to the main body of the e-band. Meanwhile, elastomeric adapter is bonded to the inlets of the e-band for the injection of liquid metal to microfluidic channels [67]. The e-band is lifted off by dissolving the water-soluble material in water. In animal experiment, it will be wrapped around the intestine and anchored on the intestine at both the electrode sites and the two ends of the band to form a loop band.
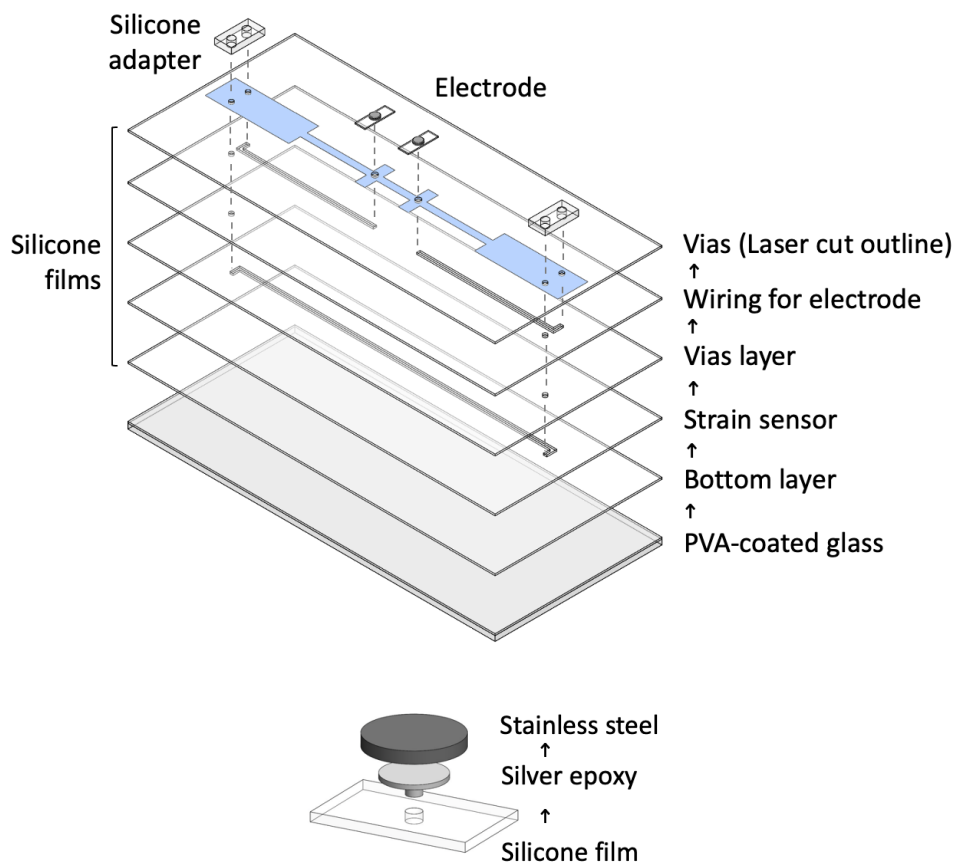
Figure 2.2 Schemetics of the e-band design. (a) Exploded view shows the five layers of SILPURAN films transferred on water soluble material-coated substrate, PDMS adapters at interconnection sites, and silver-interfaced stainless-steel electrodes. (b) Exploded view shows the zoom in of the strainless-steel electrode attached onto the SILPURAN film by silver epoxy.

27

The two electrodes of the e-band are designed to provide electrical stimulation, to record electrical activity, or to measure tissue impedance. As stimulating electrodes, biphasic current pulses are applied to tissue for neural and muscle stimulation. As recording electrodes, bipolar surface electromyography is measured to record slow wave activity and the burst of action potentials of cells. Besides, bioimpedance is also monitored to understand the electrical properties of the tissues [68]. These electrodes measure the responses between the two electrodes of the e-band or any two electrodes if more e-bands are installed on the intestine.

Before we came out the design, we first considered the conductive material of the e-band to be stretchable and electrically stable. Many approaches have been demonstrated to increase stretchability of metal wires in stretchable electronic devices, such as serpentine structure-based approaches and material-based approaches. Serpentine structures suffer from lower stretchability and buckling effect [2] during stretch-shortening cycles. From our experience, the serpentine structures made of soft material, such as PDMS, may not recover its original shape from stretching since the restoring force of the serpentine structure is weaker than the friction force between the polymer and tissue. Therefore, we considered not to adopt serpentine structures in our design. On the other hand, soft materials, such as conductive polymer nanocomposites, suffer from low electrical stability after many stretch-shortening cycles [69]. To conquer the drawbacks described above, liquid metal, such as EGaIn and Galinstan, is adopted in our design, which possesses high stretchability [70], conductivity, electrical stability [71, 72], and biocompatibility [70].

The properties of the e-band's elastomer should meet the requirement of low stiffness, permanent elasticity, good electrical insulation, biocompatibility, robustness, and easy handling, as shown in Table 2.1. The axial stiffness of the E-band is proportional to the tensile elastic modulus and cross-sectional area, and inversely proportional to the length, as shown in Equation

xxx. Although Ecoflex and Dragon skin perform great on softness, from our experience and literature, it is not easy to transfer multiple layers of these materials in a thin film fashion to build a compact 3D structure. Thicker structure is possible but it results in the increase of the stiffness [72]. In comparison, it is possible to construct compact 3D PDMS structure with multiple layers of 5-um thick PDMS thin films [20, 73]. PDMS is a good candidate but it has less stretchability than SILPURAN products (Wacker). Among the SILPURAN products, the delivery of SILPURAN film 2030 takes place in sheets with thickness ranging from 10 um to 400 um. It not only fulfills the highest medical standards but possesses excellent elastic recovery, making it predestined for gastrointestinal strain sensors.

Table 2.1 Mechanical and electrical properties of soft and elastic materials

Material	Hardness shore 00	Hardness shore A	Young's modulus (MPa)	Tensile strength (MPa)	Elongation at break (%)	Permittivity (F/m)	Ref
Sylgard 184	80	38	2.4	6.7*	135	2.70	[74]
Ecoflex 00-30	23	-	0.1	-	835	3.4	[74]
Dragon skin 10 & 30	-	10 – 30	-	3.28 – 3.45	364 – 1000	-	*
SILPURAN	-	5 – 70	-	1 – 12	300 – 850	-	*
SILPURAN film 2030	-	27	-	6	450	2.8	[75]

*Data is collected from the official websites of the products

The properties of the e-band's strain sensor should meet the requirement of high stretchability, electrical stability and sensitivity. Traditional extraluminal motility is recorded by strain gauges sutured on gastrointestinal wall. They are typically a serpentine pattern of metal wire embedded in flexible polyimide films, where the small resistance change of the metal wire is amplified by a Wheatstone bridge circuit. The curvature of the gastrointestinal wall during contraction and relaxation results in the bending of the strain gauges, and further renders the resistance of the metal wire [25, 59]. However, the recording of the curvature cannot precisely interpret the real deformation of the gastrointestinal tract. Therefore, a liquid metal-based strain sensor is adopted in our design [71, 72] and is designed to monitor the mechanical movement of the intestine by mean of the recording of the perimeter of intestine. Besides, the change of the perimeter of intestine is further related to the intraluminal pressure of the intestine.

The properties of the e-band's electrode should meet the requirement of biocompatibility (less tissue response and allergenicity), low electrode-tissue impedance (low charge transfer resistance), high long-term stability, robustness, and high resistance to liquid metal embrittlement [76, 77]. Typical materials used for implantable stimulation and recording electrodes include platinum, platinum-iridium, gold, tungsten, and stainless steel [78]. Stretchable conductive materials have been demonstrated for action potential recordings, such as PDMS mixed with gold-coated titanium dioxide nanowires for neural recording [79] and PDMS mixed with silver flakes for intramuscular EMG recording and stimulation [80]. However, these conductive polymer nanocomposites suffer from varied interface resistance (charge transfer resistance) upon stretching, which affect the power transmission spectra at the electrode-tissue interfaces and results in low signal-to noise ratio and signal distortion. Therefore, we decided to adopted typical materials as our electrodes.

Finally, the fabrication of the e-band should meet the requirement of low cost, fast tuning rate, and clean-room free. In fact, we have done different electrode designs elaborated in section xxx, including thin metal film microelectrode, heavily doped silicon electrode, SU-8 carried platinum electrode, and the printed silver adhesive-interfaced stainless-steel electrode. To conclude, we adopted the printed silver adhesive-interfaced stainless-steel electrode as our stimulation and recording electrode. The electrode is bonded to the SILPURAN film by silver epoxy and electrically connected by the liquid metal, Galinstan. It is reported that gallium reacts with silver films [76], but there is no corrosion found at the Galinstan-silver epoxy interface.

2.2.2 Principle of transmural pressure sensor

Strain sensor is designed to wrap around the gastrointestinal tract to measure the transmural pressure. The movement of contraction and relaxation or distension of the tract changes the perimeter and radius of the tract as well as the length of the strain sensor. Assuming that the gastrointestinal tract is a thin-walled cylindrical pressure vessel, according to the law of Laplace, stress in thin-walled cylindrical pressure vessels is related to the transmural pressure and the radius-to-thickness ratio [57, 81-83], as shown in Figure 2.3 and Equation 2.1 for the circumferential stress.
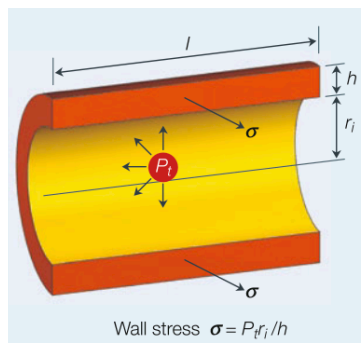
Figure 2.3 Law of Laplace for thin-walled cylindrical pressure tube [81]

31

$$\sigma_c = \frac{P_t r_i}{h} \qquad \text{(Equation 2.1)}$$

where P_t, r_i and h are the transmural pressure, internal radius and wall thickness.

Since the tissue is soft and elastic, it is hard to measure the exact thickness of the tissue. Therefore, we consider the surface tension that the composite of the e-band and tissue experiences during distension, as shown in the Equation 2.2. By knowing the inner radius of the GI tract and the surface tension (T) it experienced at certain strain, the transmural pressure can be calculated.

$$T = P_t r_i \qquad \text{(Equation 2.2)}$$

In our approach, we measure two curves to relate the electrical resistance of the e-band's strain sensor to the surface tension experienced by the tissue. Firstly, the normalized electrical resistance of the strain sensor versus strain is recorded. The curve shows linear relationship below 10% and therefore a fitted line is evaluated, as shown in Equaion 2.3. The normalized resistance could be aquired by Equation 2.4. The Secondly, the surface tension versus strain curve of a composite of a small intestine segment (1 cm x 8 cm) and an e-band (1 mm x 8 cm) placed on the mid-line of the segment is measured by a material test system (C42.503, Criterion Electromechanical Test System, MTS). The curve shows linear relationship below 10% and therefore a fitted line is evaluated, as shown in Equation 2.5. Hence, the relationship between the surface tension of the e-band-tissue composite and the electrical resistance of the e-band's strain sensor is derived, as shown in Equation 2.6. Besides, the outer radius of the GI tract is related to the inner radius and the thickness of the wall. It is also related to the original length of the e-band and the ratio of the length to the original length of the e-band, as shown in Equation 2.7 and 2.8. The original length of the e-band is a control variable and is the length before being wrapped around the GI tract. By knowing the parameters of the linear fitting curves, the initial electrical

resistance of the strain sensor at zero strain that is measured before the installation of the e-band on the GI tract, and the electrical resitance during the experiemnt, the transmural pressure can be calcuated, as shown in Equation 2.9 and 2.10.

$$R_n = m_R \varepsilon + R_{n,0} \qquad \text{(Equation 2.3)}$$

$$R_n = \frac{R_{exp} - R_{min}}{R_{max} - R_{min}} \qquad \text{(Equation 2.4)}$$

$$T = m_T \varepsilon + T_0 \qquad \text{(Equation 2.5)}$$

$$T = \frac{m_T}{m_R}\left(R_n - R_{n,0}\right) + T_0 \qquad \text{(Equation 2.6)}$$

$$r_o = r_i + h \qquad \text{(Equation 2.7)}$$

$$r_o = \frac{1+\varepsilon}{2\pi} L = \frac{1+(R_n - R_{n,0})}{2\pi m_R} L \qquad \text{(Equation 2.8)}$$

$$P_t = \frac{T}{r_i} = \frac{\frac{m_T}{m_R}(R_n - R_{n,0}) + T_0}{\frac{L}{2\pi}\left(1 + \frac{R_n - R_{n,0}}{m_R}\right) - h} \qquad \text{(Equation 2.9)}$$

$$P_t = \frac{T}{r_i} = \frac{\frac{m_T}{m_R}\left(\frac{R_{exp} - R_{min}}{R_{max} - R_{min}} - R_{n,0}\right) + T_0}{\frac{L}{2\pi}\left(1 + \frac{\frac{R_{exp} - R_{min}}{R_{max} - R_{min}} - R_{n,0}}{m_R}\right) - h} \qquad \text{(Equation 2.10)}$$

where R_{exp}, R_{min}, R_{max}, m_R, R_0, T, m_T, T_0, r_i, r_o, h, L, ε and P_t are the electrical resistance of the strain sensor, electrical resistance of the strain sensor at zero strain, electrical resistance of the strain sensor at strain of 1.17, slope and y-intercept of the fitted resistance-strain curve, the surface tension of the e-band-tissue composite, slope and y-intercept of the fitted tension-strain curve, inner radius, outer radius and thickness of the GI tract, initial length of the strain sensor that used to wrap around the GI tract, the ratio of the stretched length to the initial length of the strain sensor, and transmural pressure, respectively.

2.3 Fabrication process

The stretchable electronic rubber bands were fabricated by silicone thin film transfer process, conventional laser cutting, screen printing process, and microfluidic filling process with liquid metal in a clean room free environment.

2.3.1 Fabrication of stretchable electronic rubber band
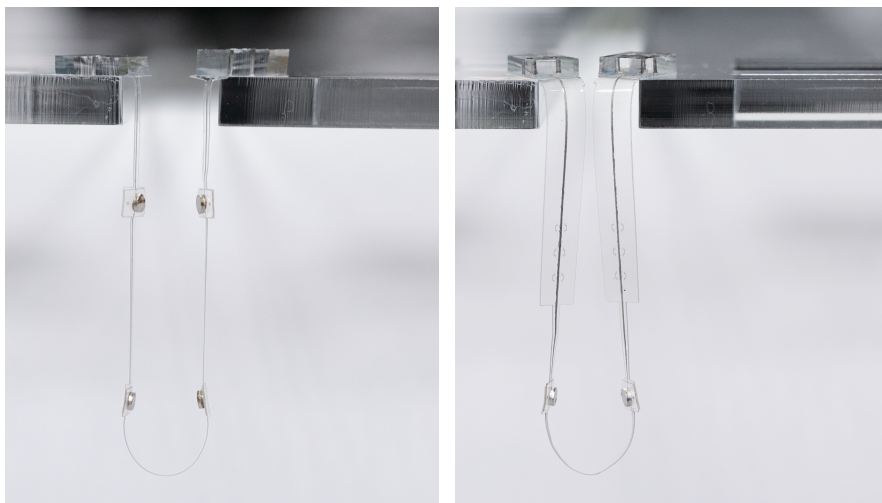
Figure 2.4 Images of fabricated E-band

As shown in Figure 2.4, the main body of the e-band is composed of five layers of elastomer films, including, from bottom to top, substrate, a microfluidic channel for strain sensor, vias, two microfluidic channels for two electrodes, and vias. The outline of the e-band is shaped by laser cutting machine after the five layers transferred on water-soluble polymer coated glass slides. The electrode layer is composed of an elastomer film, a layer of silver adhesive, and a stainless-steel disk, and is transferred to the main body of the e-band. Meanwhile, elastomeric adapter is bonded to the inlets of the e-band for the injection of liquid metal to microfluidic channels. The e-band is lifted off by dissolving the water-soluble material in water. In animal

experiment, it will be wrapped around the intestine and anchored on the intestine at both the electrode sites and the two ends of the band to form a loop band. Details of the fabrication are described below.

a. A water soluble sacrificial layer that enables plasma-activated silicone bonding was developed. 15 g of PVA was dissolved in 100 mL distilled water at 90 degree C with vigorous stirring for at least 8 hours. The mixture could be in a wide range of concentration by extending heating time or further diluting with water. The PVA solution was then filtered with a 40 um filter, cooled down, and stood still at least overnight to remove air bubbles.

b. Spin coated 10 wt % PVA solution at 2000 rpm on glass substrate and baked at 65 degree C for 1 min and annealed at 130 degree C for 30 min [84].

c. The silicone sheets (SILPURAN 2030 250/20, WACKER) were composed of two layers: a 20 um thick SILPURAN film and a PET carrier film. The silicone sheets were patterned by a laser cutting machine (TAUV-3W Laser System, 3AXLE Technology) using the parameters shown in Table. 2.2. Figure 2.5 shows the laser-cut microchannels.

d. To transfer the SILPURAN film of silicone sheets on PVA-coated glass, air plasma was first used to activate both surfaces (500 mTorr, 30 sec, 18W; PDC-32G, Harrick Plasma).

e. Place the plasma-activated SILPURAN film on plasma-activated PVA coated glass. To enhance bonding strength between two films, 80 degree C baking for 4 hours was then applied. Here, oxygen plasma was not suggested for SILPURAN/PVA bonding. After 4 hours, the PET carrier film was removed from SILPURAN film.

f. Repeat step c, d and e to transfer multiple layers of SILPURAN films on PVA-coated glass.

g. Bond PDMS adapters onto the inlets of microfluidic channels and bond fabricated silver epoxy/stainless steel electrodes (elaborated in section 2.3.2) on vias of microfluidic channels, as shown in Figure 2.5 (a).

h. Inject Galinstan into microchannels, which is a eutectic alloy composed of gallium, indium, and tin with melting temperature of -15 degree C, as shown in Figure 2.5 (b).

(a)

(b)

(c)   (d)
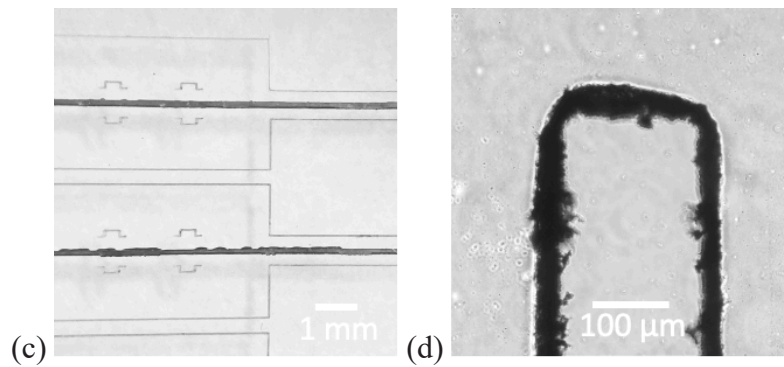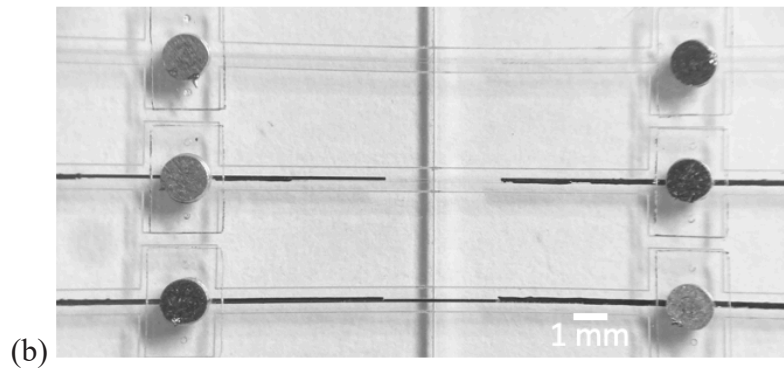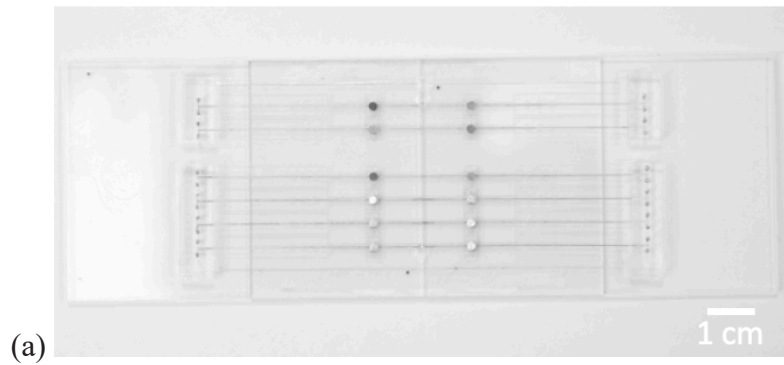
Figure 2.5 Images of laser-cut microchannel. (a) Five layers of SILPURAN films and electrodes were transferred on PVA-coated glasses. (b) The injection of liquid metal into microfluidic channel layer by layer. There was no filling in the top e-band, filling of 2 wires on the forth floor for interconnection of two electrodes in the middle e-band, and extra filling of strain sensor on the first floor for strain sensor in the bottom e-band. (c) The close look of the anchor sites (d) The microscopic image of the microfluidic channel.

Table 2.2 Laser cutting parameters used for different thickness of materials on PET

Parameter/Material	SILPURAN sheet (100 um)	SILPURAN sheet (60 um)	SILPURAN sheet (20 um)	Paper label
Scan rate	4 mm/s	8 mm/s	17 mm/s	25 mm/s
Pulse width	1 µs	1 µs	1 µs	6 µs
Frequency	40 kHz	40 kHz	40 kHz	40 kHz
Engraving time per point	0.1 ms	0.1 ms	0.1 ms	0.1 ms

2.3.2 Fabrication of electrode

There were several concerns for the electrode designs. First of all, externally, the electrode is used to contact biological samples for electrical stimulation and electrophysiological recordings, and internally, it has to electrically connect to liquid metal filled in microfluidic channels. Hence, two openings are required. Second, the adhesion between electrode and stretchable substrate should be strong under high strain. Third, to record contraction and relaxation of muscle tissues, the biocompatibility, conformity, and suitable anchoring approach of electrode on the subject were considered. Finally, toward implantable devices, robustness and repeatability of electrode performance had to be examined.

Table 2.3 Comparison of the pros and cons for different electrode types

Electrode type	Pros	Cons	Application
Thin metal film electrode	1. High resolution 2. Biocompatible 3. Compliant to typical MEMS processes	1. Low stiffness and easy to break upon stretch 2. Expensive usage of cleanroom facility	Microelectrode on flexible substrate
Conductive heavily-doped silicon electrode	1. High resolution 2. Biocompatible 3. Compliant to stretchable substrate, e.g., PDMS 4. Compliant to typical MEMS processes	1. High charge transfer resistance per unit area 2. Expensive usage of cleanroom facility	Microelectrode on stretchable substrate
SU8-carried Pt electrode	1. High resolution 2. Biocompatible 3. Compliant to stretchable substrate, e.g., PDMS 4. Compliant to water-soluble releasing tools 5. Compliant to typical MEMS processes	1. Cracking due to mismatch of thermal expansion coefficients of SU8 and platinum 2. Non-uniformity on the height of SU8 disks 3. Expensive usage of cleanroom facility	Microelectrode on stretchable substrate
Printed silver epoxy-interfaced stainless-steel electrode	1. Clean-room free 2. Fast turning rate 3. Cost efficient 4. Biocompatible 5. Compliant to stretchable substrate, e.g., PDMS 6. Compliant to water-soluble releasing tools	1. Low resolution 2. High charge transfer resistance per unit area of stainless-steel electrode	Millimeter-sized electrode on stretchable substrate

Several attempts to reach the requirements were executed. Each approach has its own pros and cons and can apply to suitable application, as shown in Table 2.3. Among all, printed silver epoxy-interfaced stainless-steel electrodes were adopted for the gastrointestinal application.

2.3.2.1 Thin metal film microelectrode

Thin metal films as electrodes transferred to PDMS films was first demonstrated by previous coworker, Dr. Ximiao Wen. The probe was fabricated on silicon wafer and released by XeF2 gas at the last step. XeF2 etching is isotropic and consumes silicon underneath the PDMS probe. It also etched PDMS but with slower etch rate. When the undercut is wider than 500 um, the releasing time of PDMS probe becomes much slower and the PDMS films became thinner and even broken. Hence, this approach was not good for large area releasing design. In the picture, the silicon was still remained at the adapter area.

To achieve rigid substrate-free design after releasing process, two approaches were established. In the first approach, Cr/Al/Pt/Cr/SiO2 layers were vapor deposited sequentially on top of silicon wafer or glass substrate and were used as an adhesion layer, a sacrificial layer, electrode material, an adhesion/protection layer and an intermediate layer, respectively. The second chromium layer enhanced the adhesion between platinum and silicon dioxide, and also prevented platinum layer from liquid metal corrosion or embrittlement [76, 77]. The intermediate layer became bondable to PDMS thin film after oxygen or air plasma treatment (500 mT, 80 W, 30sec). After all processes had done on the substrate, the aluminum layer was then released in 10 wt% sodium chloride solution by anodic dissolution technology at DC 0.7 volt.

This fabrication method enables rigid substrate-free microfluidic platform. However, it

suffered from varied dissolution rate among different location owing to the non-uniform distribution of electric fields over the sacrificial layers. Some residue of aluminum and chromium remained on the platinum electrode. Further ceric ammonium nitrate-based chromium etchant and strongly acidic aluminum etchant were required to remove these residues. Besides, this approach could provide around 2 cm undercut on each side. Patterns larger than 4 cm in any dimension took much longer time to be released and was not suitable for this approach.

To achieve acid-free release and transfer of large area ultra-thin PDMS and SILPURAN films, water soluble polymer, polyvinyl acetate (PVA), was utilized. This solid PVA layer not only acted as a water-soluble sacrificial layer but also became bondable to PDMS and SILPURAN films after air-plasma treatment (500 mT, 80 W, 30 sec) and heat treatment for additional bond formation (80 degree C for at least 4 hours). Details fabrication process for PVA solution could be found in chapter x. This approach has demonstrated a rigid substrate-free and large-area PDMS and SILPURAN thin film platforms by utilizing PVA film.

When it comes to stretchable platforms, we need to consider the yield strain and stress distribution, especially the interface between hard thin metal film and soft polymer. Thin metal films used as wires and electrodes were usually designed as serpentine structures to allow larger deformation. To prevent high stress distributed at the interface when stretching, usually a medium material was sandwiched between the hard thin film and soft materials, such as SU8 resin. On the other hand, to achieve higher yield strain, stretchable conductive materials were an alternative approach, such as polymer mixed with nanocarbon tubes, silver, or platinum powder. In general, these polymer-based conductive materials didn't have stable electrical properties as it being stretched. In order to construct robust electrode that can survive more than 200% strain with stable

electrical properties, a hard and much thicker electrode designs were considered.

2.3.2.2 Conductive heavily-doped silicon microelectrode

In order to integrate PDMS and SILPURAN thin film process to thick and hard electrodes, three approaches have been demonstrated one after another. These processes enabled the integration of liquid metal wiring in microfluidic platforms.

First, heavily doped silicon microelectrodes have been demonstrated. P-typed silicon on insulator (SOI) wafers were used. Device layer was 60 um thick, resistivity was 1-30 ohm-cm, buried thermal oxide was 1 um thick, and handle layer was 525 um thick. In the beginning, 1.5-um thick silicon dioxide was chemically vapor deposited on the SOI wafer and this protection layer was used to prevent device layer from isotropic silicon dry etching. The protection layer and device layer were patterned into the shape of microelectrodes using one photolithography process and followed by anisotropic dry etching of silicon (Oxford) and anisotropic silicon dioxide dry etching (AOE). Later, 1-um silicon dioxide was then chemically vapor deposited (CVD) on the surfaces and sidewalls of the silicon disks. This extra protection layer was used to prevent the device layer from later on isotropic silicon etching through sidewalls. Next, anisotropic silicon dioxide dry etching (AOE) was to expose the handle layer. Subsequently, isotropic silicon dry etching of handle layer was proceeded carefully to undercut the Si/SiO2 disks until the diameter of the neck underneath the disk is around 2 um. A silicon etching mask was designed and used to monitor the length of undercut during the process. The top surface of the device layer was electrically connected to liquid metal wire and the bottom layer was contacted to biological tissue for electrical stimulation and electrophysiology recordings. Hence, the top protection layer was

then removed by anisotropic silicon dioxide dry etching and then the silicon disks were pressurized contacted and transferred to PDMS film by oxygen plasma treatment (500 mT, 80 W, 30 sec) under room temperature. The precise alignment of silicon disks and PDMS film was accomplished under microscopes and 3 axes stages of the mask alignment system (Ultra µ line 7000 series, Quintel Corp.). By gentle force pressing on the handle layer, the thin necks of silicon disks were broken and released from the handle layer. The buried oxide layer now exposed and was removed by anisotropic silicon dioxide etching using RIE (machine). This machine has lower working temperature than AOE. Some Teflon-like chemical grown on top of the PDMS surface during the etching of silicon dioxide and disabled the bonding capability of PDMS. Hence, further PDMS isotropic etching process was required to remove the Teflon-like polymer layer. This approach has demonstrated conductive silicon microelectrodes with diameters ranging from 20 um to 100 um and was compatible with liquid metal wiring and microfluidic platforms. However, it was labor intensive and not cost-efficient. Consequently, SU8-carried Pt electrode was developed.

2.3.2.3 SU8-carried platinum microelectrode

SU8-carried platinum electrode with openings on both sides were demonstrated. Basically, SU8 disks were prepared on PVA coated substrate by photolithography. SU8 was developed by SU8 developer without using IPA to rinse off residues since IPA attacked PVA and SU8 adhesion. To make the disk with a tapered structure in the center, the SU8 disks were further patterned by photoresist AZ4620. By reflowing the photoresist and using polymer anisotropic dry etching, the profile of the reflowed photoresist transferred to SU8 disks. Remove photoresist using acetone since acetone didn't dissolve PVA film. Next, platinum layer and chromium layer were sputtered

on surfaces and sidewalls of SU8 and then enclosed by spin coating another layer of SU8 with a vias. The soft-baked SU8 disk was bonded to high purity N2-plasma treated SILPURAN film or PDMS film. This chemical reaction required further heat treatment to create permanent bonding. After the bonding of SU8 electrode to the SILPURAN film, immerse and release the electrode in water. The vias was later on electrically connected to liquid metal filled microfluidic channels. This approach can be further optimized if the carrier substrate was transparent, such as glass. The SU8 tapered structure was simply realized by backside exposure with a gap between mask and SU8 layer around 960 um, i.e. the thickness of glass substrate. Some issues were found. The SEM images of the SU8-carried Pt electrodes has shown some cracking after cool down from e-beam evaporator due to the difference of thermal expansion coefficient of PVA, Cr and Pt. Besides, the second layer of SU8 had edge beads near the pattens. It could affect the bonding performance. Without further optimizing the process and considering cost-efficiency, a clean-room free and a robust approach was developed.

2.3.2.4 Printed silver adhesive-interfaced stainless-steel electrode

Printed silver epoxy-interfaced stainless-steel electrode has been demonstrated, as shown in Figure 2.6. Stainless steel disks were sticked to silver adhesive when it was uncured. The cured silver adhesive was then electrically connected to liquid metal filled microfluidic channel. The adhesion between silver epoxy and SILPURAN film, and between silver epoxy and stainless-steel disks was enhanced greatly by air-plasma treatment on silicone films and stainless-steel disks. This approach achieved clean-room free and cost-efficient fabrication for biocompatible electrodes with great robustness.

(a)

(b)

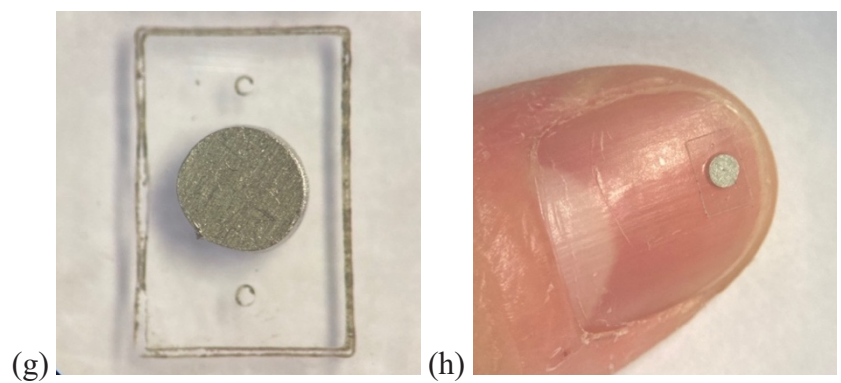(c)

Front   Back

1 mm

(d)
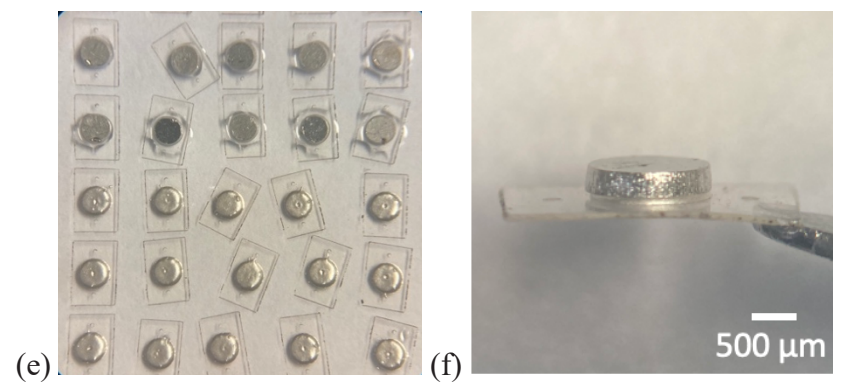

(e)

500 μm

(f)

(g)

(h)
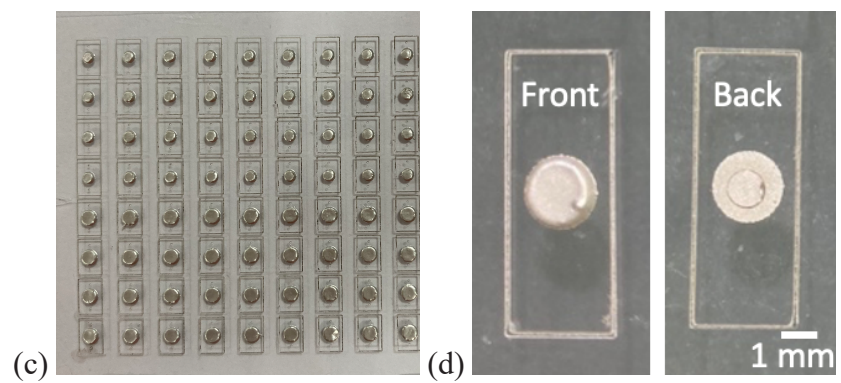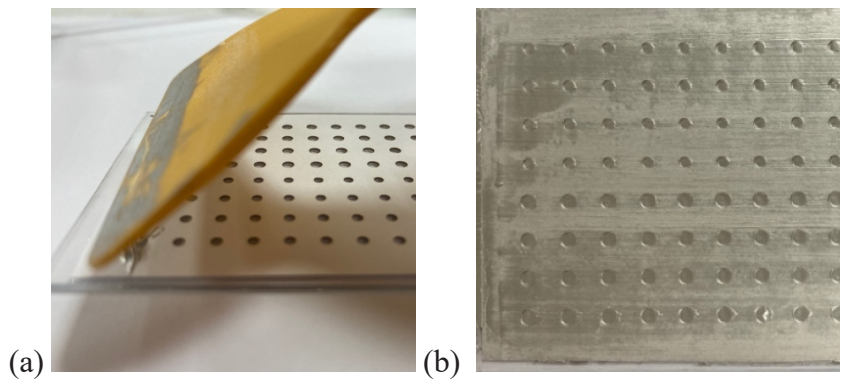
Figure 2.6 Images of printed silver-adhesive interfaced stainless-steel electrode. (a) Printing silver epoxy on plasma-treated SILPURAN film with a laser-cut paper label mask. (b) and (c) are images before and after the removal of paper label mask. (d) are the images of top and bottom views of the patterned silver epoxy. (e) The electrodes were released in water. (f) and (g-h) are the cross-sectional and top views of the silver epoxy-interfaced stainless-steel electrode.

The detailed fabrication process is shown below.

a. A 400-um thick 316L stainless steel plate (Tai Yuan Metal Corp., Taiwan) was outsourced into disks with diameter of 2 mm (3AXLE Technology, Taiwan).

b. The water-soluble sacrificial layer was prepared by spin coating 10 wt% PVA on glass substrate at 2000 rpm for 30 sec. The PVA solution was soft baked at 65 degree C for 1 min and annealed at 130 degree C for 30 min to provide stronger plasma-enabled bonding on SILPURAN film.

c. The silicone sheet (SILPURAN 2030 250/100, WACKER) was patterned by UV laser marking machine (TAUV-3W Laser System, 3AXLE Technology) using the parameters shown in Table. 2.2. The sheet was composed of two layers, including a 100-um thick SILURAN film and a 100-um thick PET carrier film, and was placed on another PVA-coated glass during the laser cutting process. The PVA film provided weaker adhesion to SILPURAN film and could prevent or mitigate the detachment of the SILPURAN film and PET carrier film when removing the sheet from the PVA-coated glass after the cutting process. Besides, the SILPURAN film was facing down on hard substrate, i.e., PVA-coated glass, to prevent the bottom surface of SILPURAN film from deforming during the cutting

process. All residues produced during the process were removed by 3M tapes.

d. The silicon sheet and PVA-coated glass were treated with air-plasma (500 mT, 18W, 30 sec; Basic plasma cleaner, PDC-32G, Harrick Plasma). The SILPURAN film was bonded to PVA film. The bonding strength was enhanced by heat treatment at 80 degree C for 4 hours. The PET carrier film was then removed.

e. Another UV laser patterned silicone film was prepared as printing mask. It was placed onto the SILPURAN film described in step d and defined the patterns of silver adhesive for the printing process. Here, the silicone film can be replaced by paper label. Cutting parameters are shown in Table. 2.2.

f. Thermal-setting conductive silver adhesive (051908, Polychem UV/EB International Corp.) was prepared by 10 to 1 ratio of silver paste and hardener by weight. The SILPURAN film and stainless-steel disks were treated with air plasma (500 mT, 18W, 30 sec; Basic plasma cleaner, PDC-32G, Harrick Plasma). The plasma treatment greatly enhanced the interface bonding strength of silver adhesive and SILPURAN film. The adhesive was then printed on the SILPURAN film by a plastic stencil. The printing mask was removed and the stainless-steel disks were individually placed on top of each uncured silver adhesive disk. The uncured silver adhesive was baked at 130 degree C for 2 hours. According to official spec, the resistivity of baked silver adhesive ranged from 1.5 e-5 to 6 e-5 (Ω.cm).

g. The printed silver adhesive-interfaced stainless-steel electrode was carried by SILPURAN film and released in water by dissolving PVA film.

2.3.3 Interconnection and fixation of ultra-stretchable elastic band

A liquid metal-filled microchannel was interconnected by a thin stainless-steel wire. One end of the stainless-steel wire was connected to a tin-plated copper wire using silver adhesive (051908, Polychem UV/EB International Corp.). The other end was bent into a loop and inserted into a hole of a PDMS adapter. The adapter was then encapsulated by placing a 1.5 mm-thick PDMS slab on top. The interconnection part was gently fixed by screwing two acrylic plates, as shown in Figure 2.7.

In order to measure contraction and relaxation of intestine movement, the E-band was pre-strained 10% to capture contraction movement. There are two ways to fix a pre-strained E-band on intestine. In the first approach, the E-band was stretched, wrapped around intestine, sandwiched by two small pieces of PDMS slabs, and tied with a thread. Since the E-band was not fixed directly on tissue, it could shift during intestine movement. In the second approach, the E-band was stretched, wrapped around intestine, and fixed by tissue adhesive (1469C, 3M Vetbond) sparingly coated on the surfaces of anchor sites. The liquid adhesive polymerized in second after contact with tissue or body fluid and became solid. It is impervious to water and created strong bond between silicone and tissue even in aqueous solution. Hence, no shifting was occurred at anchor sites. The E-band was then peeled off carefully after animal experiment with the adhesive attached. It was cleaned up by dissolving the adhesive in organic solvent such as acetone and became reusable.
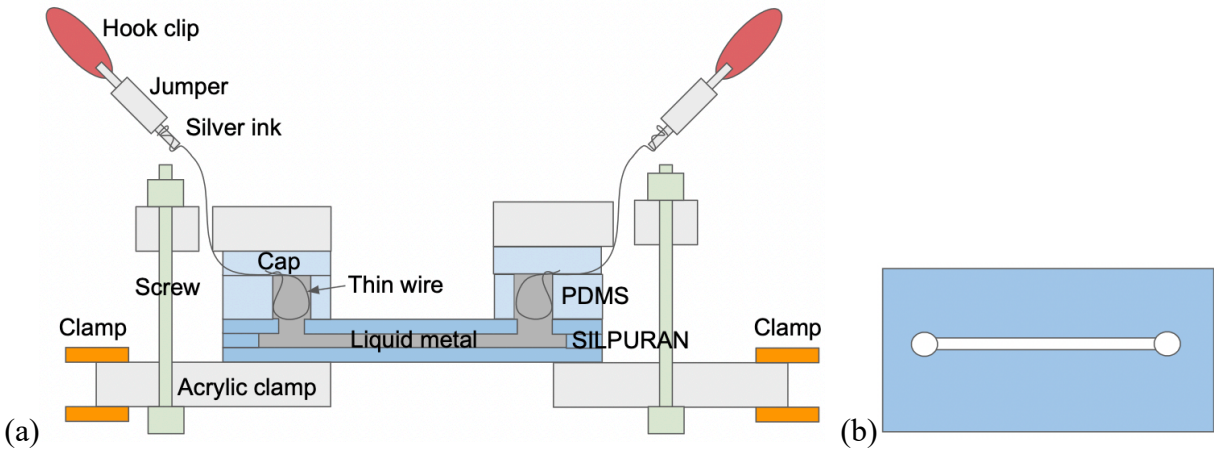
Figure 2.7 Schematics of interconnection and fixation of E-band. (a) Liquid metal filled microchannel is interconnected by thin stainless-steel wires. (b) Top view of the microchannel.

2.4 Device characterization

Ultra-stretchable electronic rubber band (E-band) has the capability of detecting strain of rubber band, sending electrical pulses, and measuring biological tissue impedance and electrical activity of muscle cells. To characterize the strain gauge during tensile testing, the load-strain curves of the E-band and the electrical resistance of the strain gauge were measured simultaneously. To characterize the stimulation electrodes, cyclic voltammetry (CV), electrochemical impedance spectroscopy (EIS), and charge injection capacity (CIC) were measured.

2.4.1 Mechanical and electromechanical properties of elastic rubber band

While the static tensile testing was performed, load-strain curves of E-band and resistance measurement of strain gauge were recorded simultaneously. Load-strain curves was recorded by a material test system with 2 kN load cell (C42.503, Criterion Electromechanical Test System, MTS).

The stretching speed ranged from 100 mm/min to 600 mm/min. The sampling rate was xxx. Meanwhile, electrical resistance was measured by a multimeter (GDM-8261A, Dual Measurement Multimeter, GW Instek, Taiwan). As a serial terminal device, the multimeter was communicated to PC via a RS232-USB interface cable at baud rate of 115200. The multimeter also adopted a scanner card (GDM-SC1A, GW Instek, Taiwan) for a maximum of 16-channel recordings. An official Microsoft Excel Add-ins and NI LabView driver supported single channel and multi-channel settings and data logging of the multimeter and scanner card. The maximum sampling rates were 10 Hz and 0.5 Hz for single channel via Excel Add-ins and 3-channel recordings via LabView, respectively. Higher data logging rate or sampling rate should be achieved by optimizing the LabView programs.

As described in Chapter 2.3, a liquid metal-filled microchannel was interconnected by thin stainless-steel wires and encapsulated by placing a PDMS slab on top of the PDMS adapter. Each side of the E-band was sandwiched by two acrylic plates and fixed by two screws. The bottom acrylic plates were clamped by the holding grips of the material test system for tensile testing. The thin stainless-steel wires were connected to the multimeter through tin-plated copper wires for electric resistance measurement, as shown in Figure 2.7.

2.4.1.1 Mechanical properties of elastic rubber band

For tensile testing, the stretching part of the E-band was 8.5 cm long, 1 mm wide, and 140 um thick, as shown in Figure 2.8. The load-distance curves of E-band were measured and further converted to load-strain curves, as shown in Figure 2.9.

The E-band was subjected to 10 loading and unloading tension cycles at different scanning rates ranging from 100 mm/min to 600 mm/min. Figure shows the raw data of load-distance curves

of the E-band at scanning rate of 100 mm/min. The load-strain curves for load and unload almost coincide. Hence, the highly stretchable elastomer has low hysteresis, which means it dissipates little energy during normal operation of cyclic loads. The Polynomial Fit tool in Origin was used to fit loading and unloading data by third order polynomial, respectively. Fitted results for scanning rate ranging from 100 mm/min to 600 mm/min are shown in Figure 2.9. It shows the consistency at different scanning rates. The ultimate tensile strain and fracture strength are shown in Figure 2.10 (i). The failure occurred in the mid-section of the specimen. Maximum strain of 117% was applied in the test.

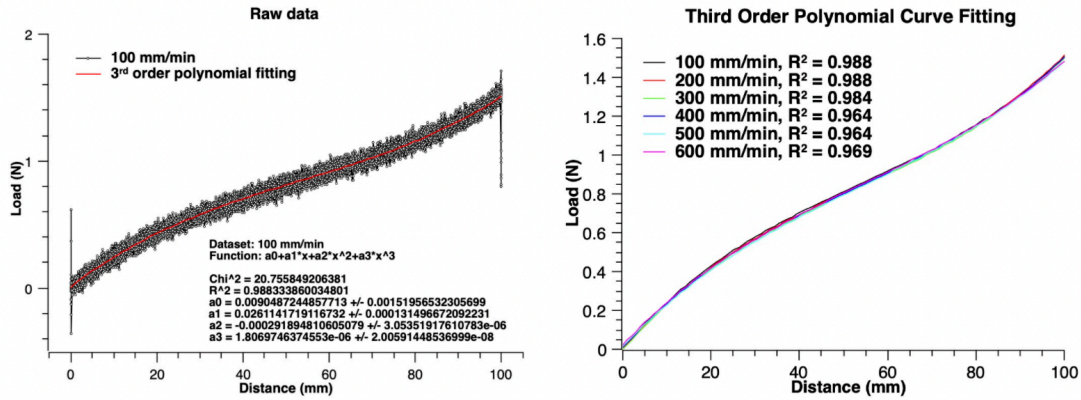Figure 2.8 Image of e-band clamped by a stretching setup

Figure 2.9 Load-distance curve of e-band

2.4.1.2 Electromechanical properties of elastic rubber band

When the E-band was subjected to cyclic loading and unloading for 100 cycles, the real-time electrical resistance was measured, as shown in Figure 2.10 (a) and (b). The maximum resistance of each cycle reaches steady-state after 3 cycles. By comparing the real-time resistance curve with its corresponding load-strain curve, the resistance measurement was related to strain, as shown in Figure 2.10 (c). In Figure 2.9, the loading and unloading curves almost coincide and no obvious hysteresis of SILPURAN is found. In Figure 2.10 (c), the resistance-strain curve shows the hysteresis at strain above 0.6. This implies that the hysteresis is not related to the mechanical property of SILPURAN but the resistivity of the liquid metal.

Ideally, the electrical resistance of the liquid metal is affected by the deformation of the surrounding elastomer, but it is also influenced by fluid mobility of the liquid metal [85]. In fact, the total volume of the liquid metal in the microchannel varied. During loading and unloading, the inlets of the microchannel gained the excess of the liquid metal or supplied the microchannel when it was lack of liquid metal. However, the viscosity of liquid metal and the friction between liquid metal and channel walls rendered the flowing of liquid metal. During unloading, the elastomer was

51

retraced but the viscosity of liquid metal in inlets resisted itself from flowing back to the microchannel. Hence, at the same strain above 0.4, the electrical resistance of unloading curve is higher than its counterpart of loading curve. This implies the flow resistance varies especially when the E-band is stretched above 0.4. This non-monotonic relationship between resistance and strain could be mitigated by changing the cross-sectional design of microfluidic channel, such as equilateral triangle or concave triangle [85].

To characterize the relation between resistance and strain for different batch of E-bands, three E-bands with different initial resistance was subjected to cyclic loading and unloading for 100 cycles. Each normalized resistance-strain curve is obtained by subtracting the initial resistance and scaled by the difference in resistance between strain of 1.17 and 0, as shown in Figure 2.10 (c-f). In Figure 2.10 (g-h), first order polynomials are used to fit the data of the three resistance-strain curves for the strain below 10% with and without normalization, respectively. A maximum strain of 1.86 was achieved, as shown in Figure 2.10 (i).

Besides, when the E-band is subjected to 10 loading and unloading tension cycles for each scanning rate ranging from 100 mm/min to 600 mm/min, the maximum resistance decreases as rates increases, as shown in Figure 2.11. The resistance responses cannot immediately follow the deformation and is expected to be related to fluid motility of liquid metal.

(a)

(b)

(c)

(d)

(e)

(f)

53
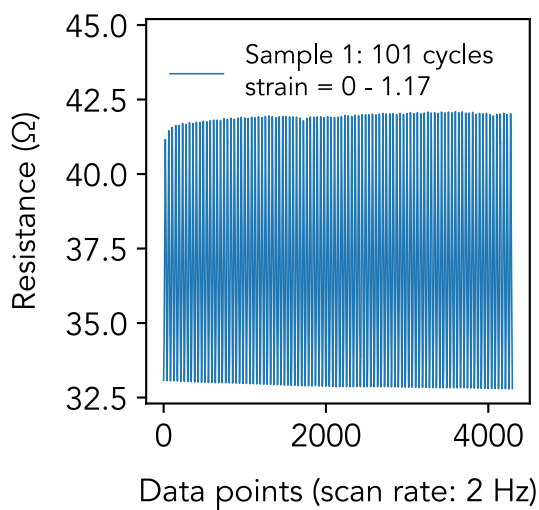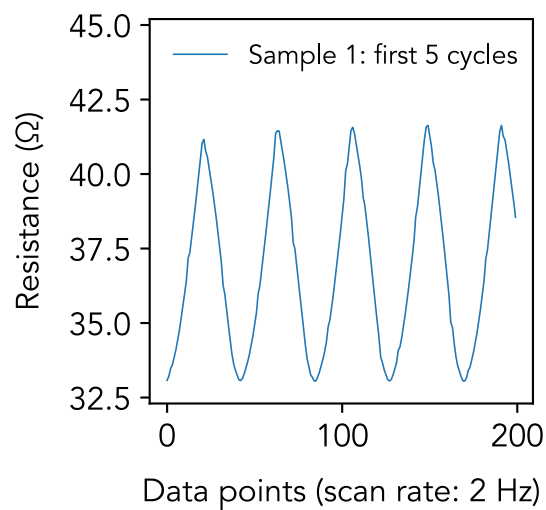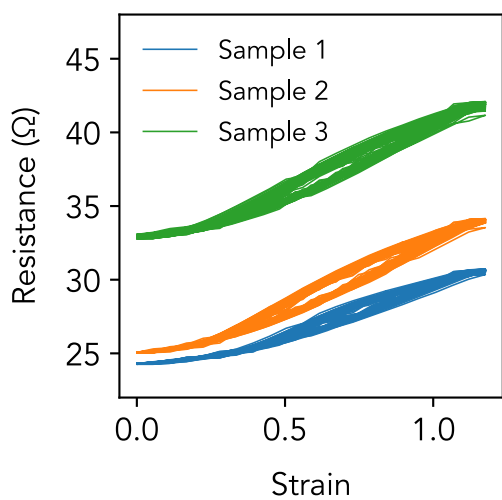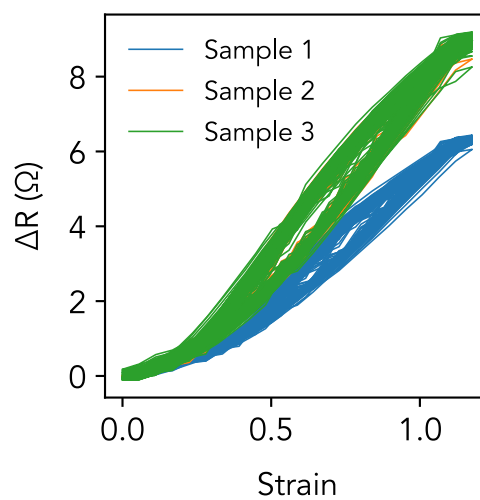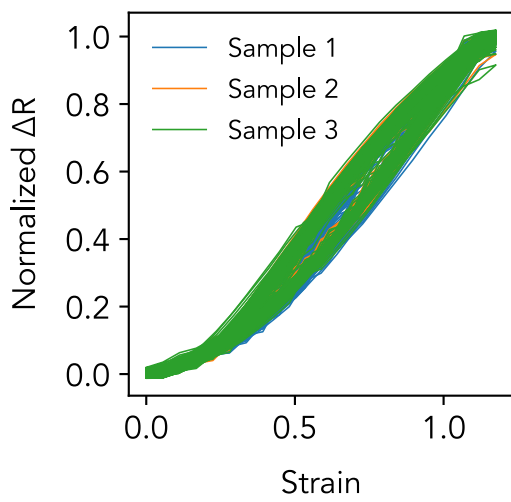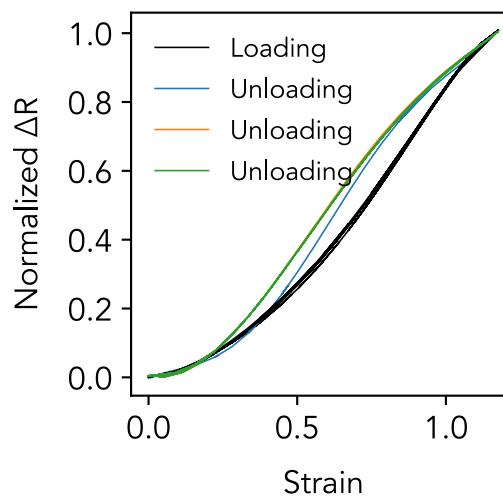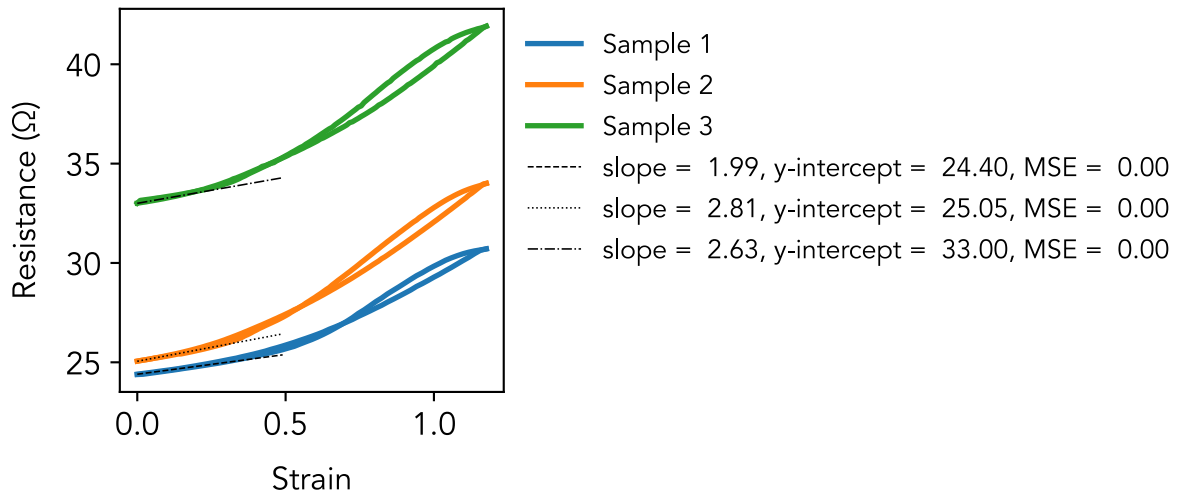
(g)
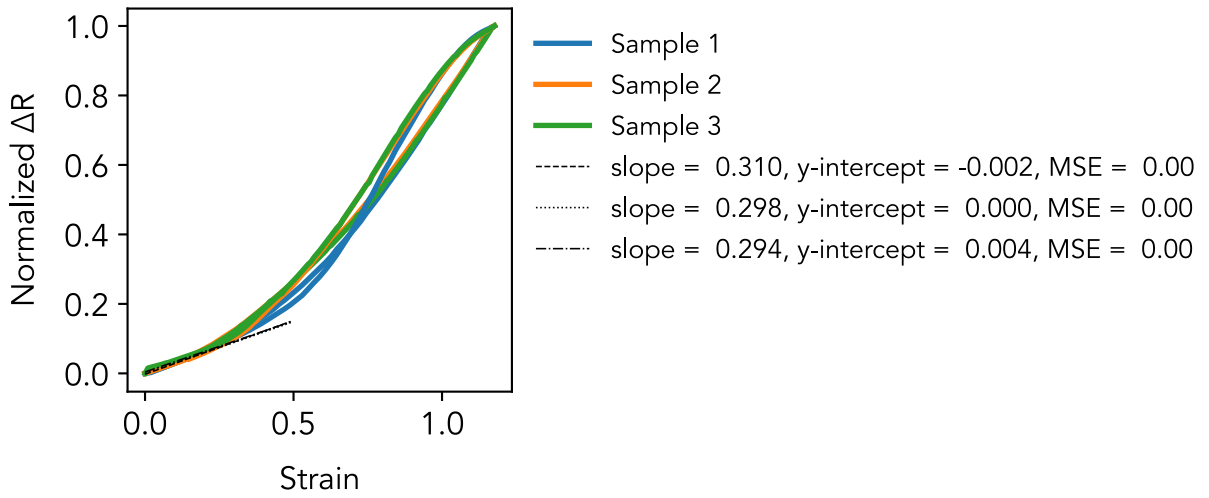
(h)
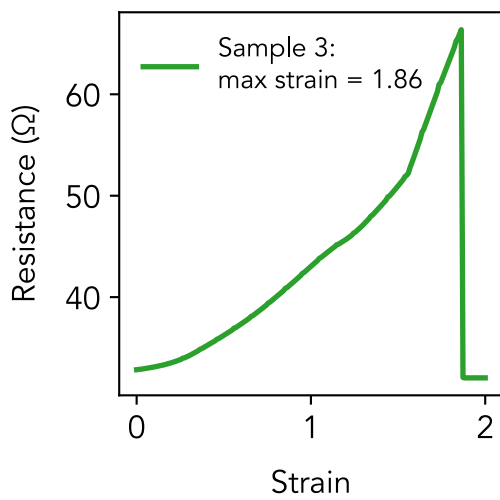
(i)

Figure 2.10 Normalization of electrical resistance versus strain of E-band at scanning speed of 600 mm/min upon 100 loading and unloading tension cycles. (a) Electrical resistance of the e-band upon 101 loading and unloading tension cycles. (b) Close look of the first 5 cycles. (c) Conversion resistance-time curve to resistance-strain curve. (d) Baselined resistance-strain curve. (e) Normalization of resistance-strain curve by the maximum resistance difference at strain of 1.17. (f) 5th order polynomial fitting curves for loading and unloading curves. (g) Linear fitting of 3 resistance-strain curves from 3 e-bands at strain below 0.1. (h) Linear fitting of 3 normalized 3 resistance-strain curves from 3 e-bands at strain below 0.1. (i) Resistance-strain curves of e-band with maximum strain of 1.86.
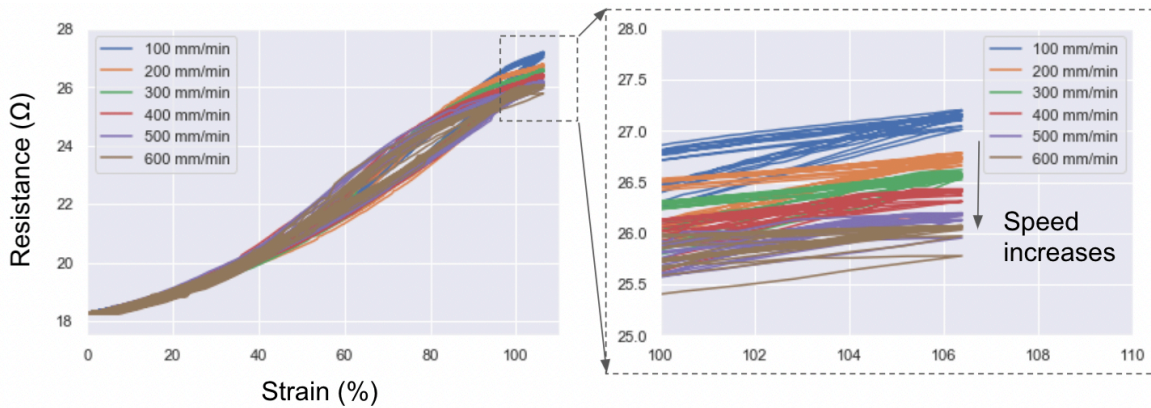
Figure 2.11 Electrical resistance versus strain of E-band at different scanning speed upon 10 loading and unloading tension cycles.

2.4.2 Electrical properties of electrodes

Details of standardized electrode performance tests have been elaborated in Chapter 1.3.

A three-electrode system of potentiostat (SP150, BioLogic) was used to examine electrochemical properties of recording and stimulation electrodes in phosphate buffer solution (PBS, 1X). It consisted of three electrodes, including a stainless-steel working electrode (400 um thick x 2 mm diameter), a Pt plate counter electrode (1 cm x 1 cm), and an Ag/AgCl reference electrode (3M NaCl). They were equal-distanced from each other and in triangle manner with the Pt plate electrode facing to the center of the triangle.

The working electrodes were made from a 400-um thick 316L stainless steel plate (Tai Yuan Metal Corp., Taiwan) and outsourced into disks using high power laser system (3AXLE Technology, Taiwan). The disks were contaminated by rust during the laser cutting process, and hence, were immersed in 2 wt% oxalic acid for the removal of contaminants. After the cleaning process, air plasma treatment (500 mTorr, 30 sec, 18W; PDC-32G, Harrick Plasma) was applied on the disks, which greatly improved the adhesion between stainless steel and uncured silver adhesive. The disk electrodes were connected by liquid metal-filled microfluidic channels and examined in the following techniques.

2.4.2.1 Characterization of recording electrodes

Potentio electrochemical impedance spectroscopy (PEIS) was utilized to measure the impedance in a broad frequency band (1 Hz to 100 kHz) and displayed as Bode and Nyquist plots.

In Figure 2.12, the Bode plot shows the impedance of the equivalent circuit at different frequencies. The impedance at 100 kHz is 100 times lower than that at 0.1 Hz and therefore can be seemed as a "high pass" filter. Take the recording of biopotential as example. The membrane

potential of muscle cells is passing by the electrode. The higher the interface resistance, the lower the electric current flowing through the interface. Therefore, the total power that transmits to the recording system decreases. A cut-off frequency is commonly used to characterize the filter. The cut-off frequency, or 3dB point, of the circuit is corresponding to a phase angle of -45 degree, where the real part of the impedance decreases to 0.707 times of the magnitude of the impedance. These features imply that when signal passes through larger impedance, it is attenuated and owning to different amount of phase shift, a signal composed of wide band of frequencies experiences non-liner distortion. Therefore, the plot outlines the transfer function of signal through the electrode-electrolyte interface.

(a) (b)
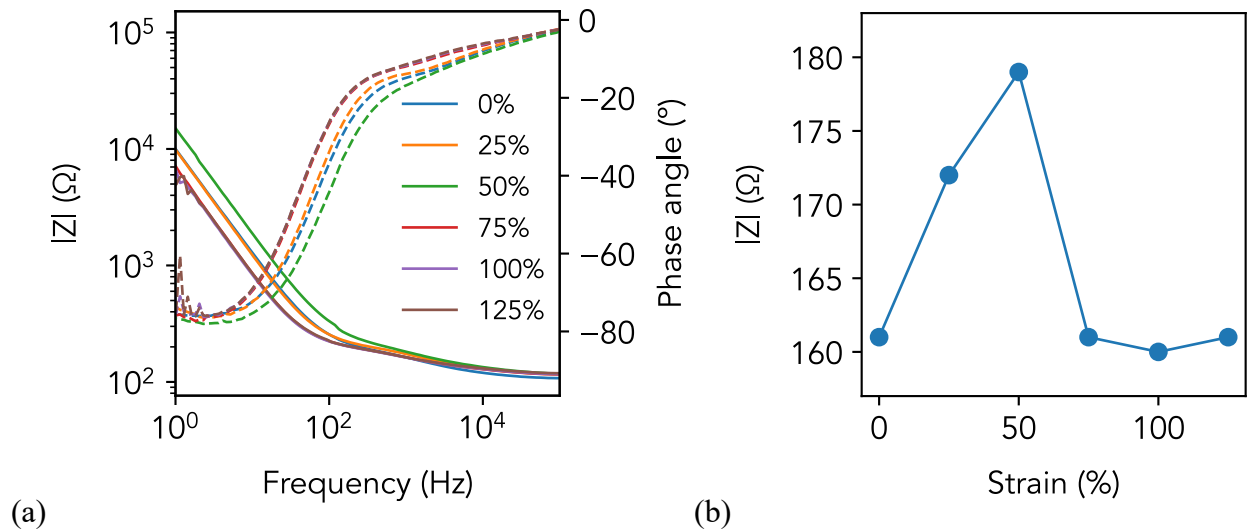
Figure 2.12 Impedance response of stainless-steel electrode on E-band at different strain levels. (a) Bode plots. (b) Impedance at 1 kHz.

Besides, the surface of a stainless-steel electrode was activated by the application of cyclic voltage in PBS solution (1X). [4] After 20 cycles of potential sweep between -1 and 1 V at a scan

rate of 100 mV/s, the cut-off frequency shifts from 66 to 37 Hz. Linear regression for the log-log plot is applied to the impedance data ranging from 1 to 10 Hz. The slope, y-intercept (at 1 Hz), and R-squared are (-0.891, 3.999, 1) and (-0.919, 3.847, 0.999), respectively. The slope is the exponent of the frequency variable and y-intercept is the exponent of 10. However, it cannot provide informative conclusions on what was happening on the electrode-electrolyte interface after the activation cycles. Therefore, Nyquist plots are required to analyze the phenomena.

Nyquist plots are utilized to obtain estimates of equivalent circuit models with appropriate elements and parameters in the frequency range of interest [86-89] . Other than ideal resistors and capacitors, distributed elements, such as constant phase element (CPE), Warburg element for semi-infinite diffusion and convective diffusion, restricted diffusion elements, and modified restricted diffusion elements, are suitable components to be applied to equivalent circuit models for the understanding of electrochemical process. The parameters of these distributed elements are shown in Equation 2.11 - 2.15. Moreover, yielding estimates of components and parameters are crucial if the interface should be load-matched with electrical circuits of a recording amplifier or an electrical stimulator.

$$Z_{CPE}(f) = \frac{1}{Q_{CPE}(i2\pi f)^{\alpha_{CPE}}}$$ (Equation 2.11)

$$Z_W(f) = \frac{\sqrt{2}\sigma_d}{\sqrt{i2\pi f}}$$ (Equation 2.12)

$$Z_{Wd}(f) = R_d \frac{\tanh\sqrt{\tau_d i2\pi f}}{\sqrt{\tau_d i2\pi f}}$$ (Equation 2.13)

$$Z_M(f) = R_d \frac{\coth\sqrt{\tau_d i2\pi f}}{\sqrt{\tau_d i2\pi f}}$$ (Equation 2.14)

$$Z_{Ma}(f) = R_d \frac{\coth(\tau_d i2\pi f)^{\frac{\alpha_d}{2}}}{(\tau_d i2\pi f)^{\frac{\alpha_d}{2}}}$$ (Equation 2.15)

(a)

(b)

(c)

(d)

(e)

(f)

(g)

(h)

(i)

59

(j)
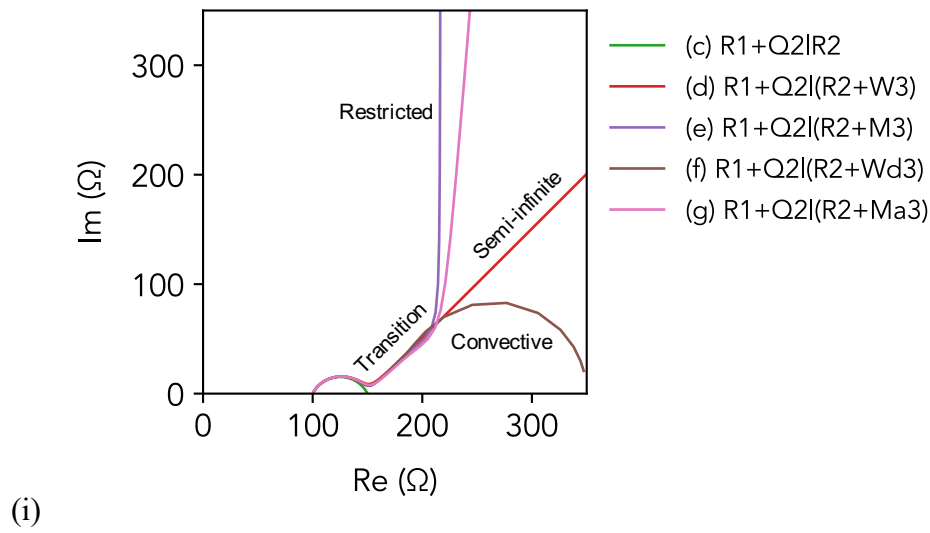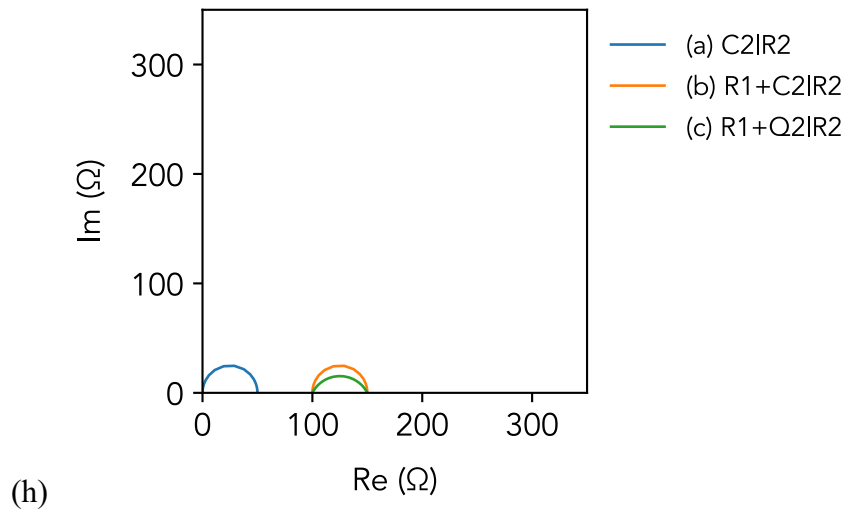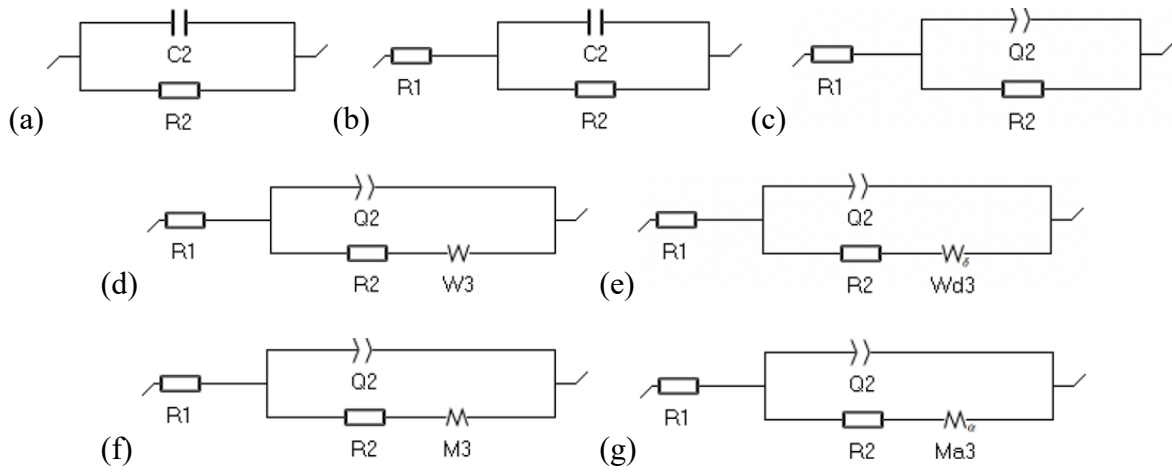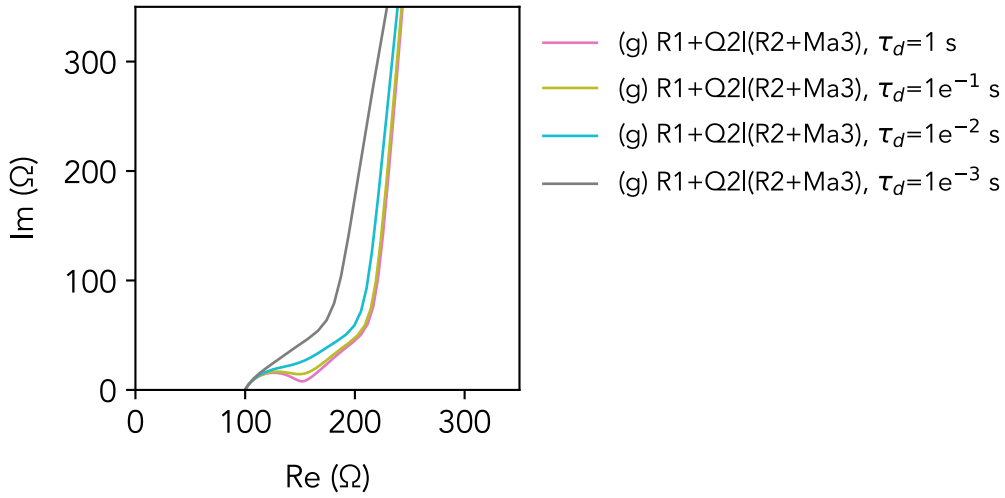
Figure 2.13 Simulated Nyquist plots for the understanding of Randles circuit with distributed elements. (a) An ideal charge transfer resistance, R2, is in parallel with an ideal double-layer capacitance, C2. (b) A simplified Randles circuit. A solution resistance, R1, is in series with a parallel combination of C2 and R2. (c) Modified Randles circuit. C2 is replaced by a constant phase element, Q2, which represents a non-ideal double layer capacitance. (d-g) Diffusion elements are added to the Modified Randles circuit to address the diffusion-limited ion exchange kinetics at low frequency. R2 is added by (d) a Warburg diffusion element for semi-infinite diffusion, W3, (e) a restricted diffusion element, M3, (f) a Warburg element for convective diffusion, Wd3, and (g) a modified restricted diffusion element, Ma3. (h-j) are plotted curves for the comparison between (a-c), (c-g), and (g) with different time constants, respectively. The default parameters used in the figures are $R1 = 25\,\Omega$, $R2 = 50\,\Omega$, $C2 = 10\,\mu F$, $Q_{CPE} = 10\,\mu F \cdot s^{(\alpha_{CPE}-1)}$, $\alpha_{CPE} = 0.7$, $\sigma_d = 200\,\Omega \cdot s^{-0.5}$, $R_d = 200\,\Omega$, $\tau_d = 1\,sec$, and $\alpha_d = 0.95$.

The electrical and electrochemical components involved in the electrode process, as a whole, can be decomposed by charge transfer process and mass transfer process. The former and

60

the latter usually happen at high and low frequency, respectively. To decipher what components are evolved in the electrode process, Figure 2.13 shows the Nyquist plots of different equivalent circuits. A simplified Randles circuit (-R-R||C-) is first used to simulate the charge transfer process, of which the RC parallel yields a full semicircle arc and the series resistance contributes a positive shift of the arc in x axis in the complex plane. The series resistance represents the solution resistance and the RC parallel represents the charge transfer resistance and the capacitance of the ideal electrical double layer at the electrode-electrolyte interface. In fact, experimental data are rarely found to be a full semicircle and its center is frequently displaced below the real axis due to the distributed element at the interface [90]. Instead of a RC parallel component, the impedance of the depressed circular arc can be simulated as a combination of the resistance in parallel with a CPE impedance. Here, the resistance and CPE impedance represent the charge transfer resistance and a non-ideal electrical double layer, respectively. The coefficient of CPE, α, ranges from 0 to 1, where 0 and 1 correspond to a pure resistance and an ideal capacitor, respectively. Since the depressed arc does not pass through the origin, a shift of the arc is required. Therefore, a solution resistance is in series with the charge transfer resistance in parallel with the CPE impedance (-R-R||CPE-).

However, the modified Randles circuit fails to simulate the straight line in the complex plan at low frequency. Such straight line is indicative of a distributed element [90]. At low frequency, the electrochemical reaction became diffusion-controlled, the charge transfer rate was limited by the transport rate of the reactants through the solution and hence the reaction transitioned from charge transfer process to mass transfer process [87]. Typically, a Warburg diffusion element (ZW) is used to simulate a semi-infinite linear diffusion. It is an example of CPE

with α equal to 0.5 and a constant angle of -45 degree. The Warburg element is in series with the charge transfer resistance (-R-(R+ZW)‖CPE-) to modify the interface impedance at low frequency.

Nevertheless, the Warburg element is not sufficient to simulate the experimental data at even lower frequency [86]. In the transition zone, the angle decreases from -45 to -80.7 degree. In the EC-Lab software, the Warburg element can be replaced by a modified restricted diffusion element (ZM) to address the transition process from semi-infinite linear diffusion to finite length linear diffusion [88]. At higher frequency, this element is equivalent to Warburg element with a constant angle of -45 degree, while, at lower frequency, the constant angle shifts to $-90\alpha_d$ degree. This transition happens at frequency of $3.88/2\pi\tau_d$. From the fitting results, the modified Randles circuits (-R-(R+ZM)‖CPE-) successfully simulate the electrode process.

(a)   (b)
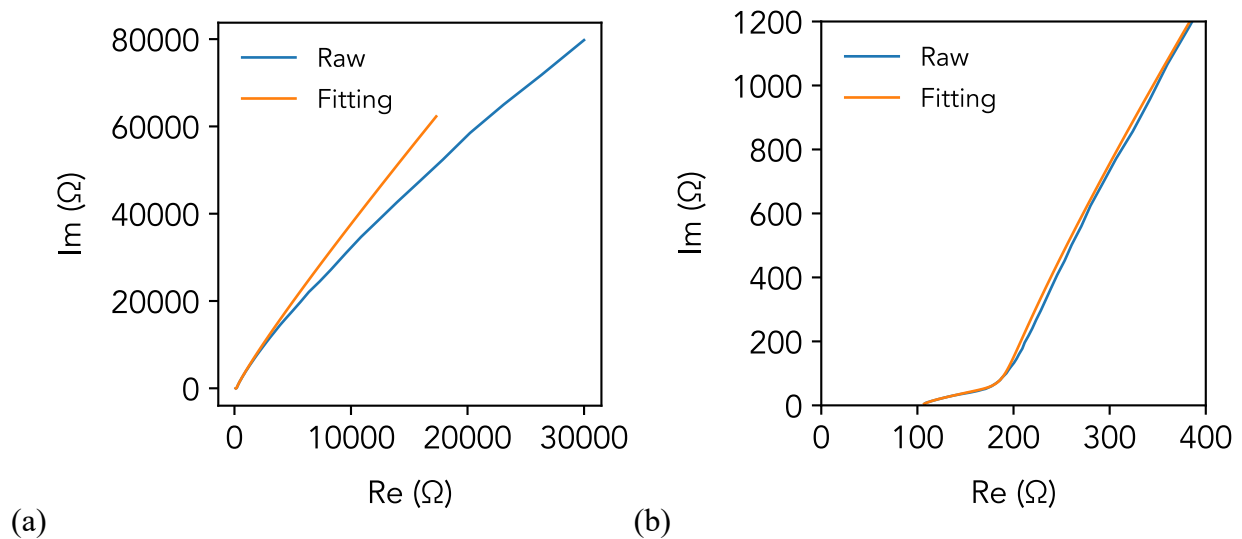
Figure 2.14 Fitting of Nyquist plot of stainless-steel electrode on E-band. (a) Raw data. (b) Zoom in at higher frequency range.

The Nyquist plots of the modified Randles circuit were analyzed using "Z-fit" function in EC-Lab software, as shown in Figure 2.14. Data ranging from 10 Hz to 100 kHz were fitted by "Randomize + Simplex" method with maximum iteration limit of 5000, where "Randomize" is first used to give optimal initial values for the subsequent "Simplex" minimization. The most suitable set of parameter values are the values that yield the lower mean squared error. The fitted components and parameters of the two Nyquist plots (before and after 20 cycles of potential sweep between -1 and 1 V) are shown in Table 2.4. According to the table, both transfer charge resistance (R2) and diffusion resistance (Rd3) decreases. The capacitance of the electrical double layer (Q1) increases and the CPE coefficient decreases. These imply the increase of electrochemical active surface and a less ideal capacitor of the electrical double layer. Besides, the increase of the solution resistance may result from the change of distance between the working electrode and counter electrode.

Table 2.4 Fitting components and parameters of modified Randles circuit for stainless-steel electrode on E-band

	R1 (Ω)	Q1 (1/Ω)	α1	R2 (Ω)	Rd3 (Ω)	τ3 (sec)	α3	χ2/|Z|
Before	104.4	11.81e-6	0.7202	52.37	187.3	1.558e-3	0.9457	7.716e-3
After	112.7	14.69e-6	0.6991	43.18	180.3	2.62e-3	0.955	4.705e-3

2.4.2.2 Characterization of stimulation electrode

Cyclic voltammetry (CV) and chronopotentiometry (CP) were utilized to measure cathodic charge storage capacity (CSCc) and charge injection capacity (CIC), respectively.

For pulse stimulation electrode, safely delivery of required amount of charge across the electrode-electrolyte interface is desired. To achieve the goal, within the pulse duration, the maximum amplitude of the voltage across the electrode double layer should not exceed the activation voltages of water dissociation under either in cathodic or anodic phase. The electrolysis of water is an irreversible faradaic process and results in formation of oxygen and hydrogen gas and substantial pH changes due to the products of protons and hydroxide. Overtime, it could be harmful to surrounding biological tissues and corrode or otherwise deteriorate the electrode surfaces.

When performing a CV, forward scans were conducted in PBS solution (1X) with a scan rate of 100 mV/s. Since the half-cell potential of the Ag/AgCl electrode was not varied during time, it was used as a reference potential. The voltage supplied to the working electrode was monitored by a voltameter, which was connected to the working electrode and reference electrode, while a galvanometer was in series with the working electrode and counter electrode to record the electric current flowing in between, as shown in the Figure 2.15. The x-axis and y-axis were the values of voltameter and galvanometer, respectively. Each cycle, the working electrode was swept from open circuit potential to upper vertex potential, swept reversely to lower vertex potential, and swept forward to open circuit potential. At open circuit potential, there is no potential or current applied to the working electrode.

In Figure 2.16, the water dissociation at the electrode-electrolyte interface is found in the CV curve of the stainless-steel electrode. The open circuit potential was -0.14 V, and the upper and lower vertex potential was 2 and -2 V, respectively. The magnitude of electric current increases exponentially below -1 V and above 1.2 V. It implies the occurrence of the electrolysis of water, which is mainly kinetically limited in water solution. The range between the activation voltages is

defines as water window. To be conservative, water window was set between -1 and 1 V in the experiment.
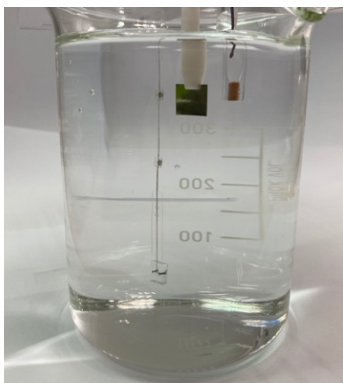
Figure 2.15 Three-electrode configuration of cyclic voltametry
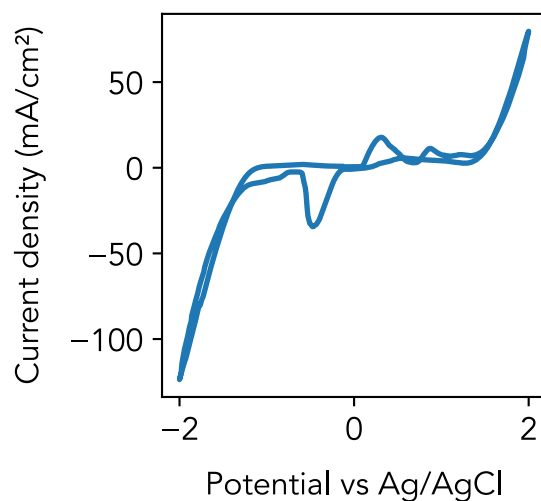
Figure 2.16 Cyclic voltammetry of stainless-steel electrode for the examination of electrolysis potential

The cyclic voltammetry (CV) is utilized to obtain activation voltages of reactants that enter into courses of chemical reactions, and voltage ranges in which solvents are neither oxidized nor reduced. When the voltage across the electrode double layer exceeds the half-cell potentials of

reactants, the reactants will be consumed rapidly and the electric current increases. Once the reactants become diffusion limited, the electric current decreases. The characterization voltages of these peaks from different reactions outline an electrochemical signature of the electrode in specific electrolytes, as shown in Figure 2.17. In fact, if the electrode has high electrochemical active area, the activation voltages shift further away from the origins as the scan rate increases [63]. The scan rate increases from 20 mV/s to 200 mV/s, the anodic and cathodic characterization voltages changes from 0.170 V to 0.295 V, and -0.182 V to -0.440 V, respectively.
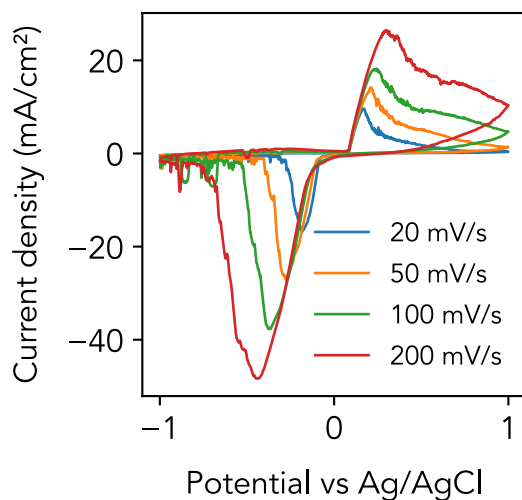
Figure 2.17 Cyclic voltammetry of a stainless-steel electrode on e-band at various scanning rates

Figure 2.18 (a) shows the CV curves at different cycles of voltage sweeps to estimate the charge storage capacity (CSC) of the electrode. The CSC is the total charge transferred to the electrode and can be calculated by the area enclosed in one cyclic sweep. It indicates the maximum charge can be delivered to the electrode without the occurrence of electrolysis of water. In neural interface, it is common to focus on catholic storage capacity (CSCc) as a comparative measure

between electrodes [62]. The CSCc was calculated by the integral of the reverse scan from the upper to the lower vertex potential defined by the water window, as shown in Figure 2.18 (b).
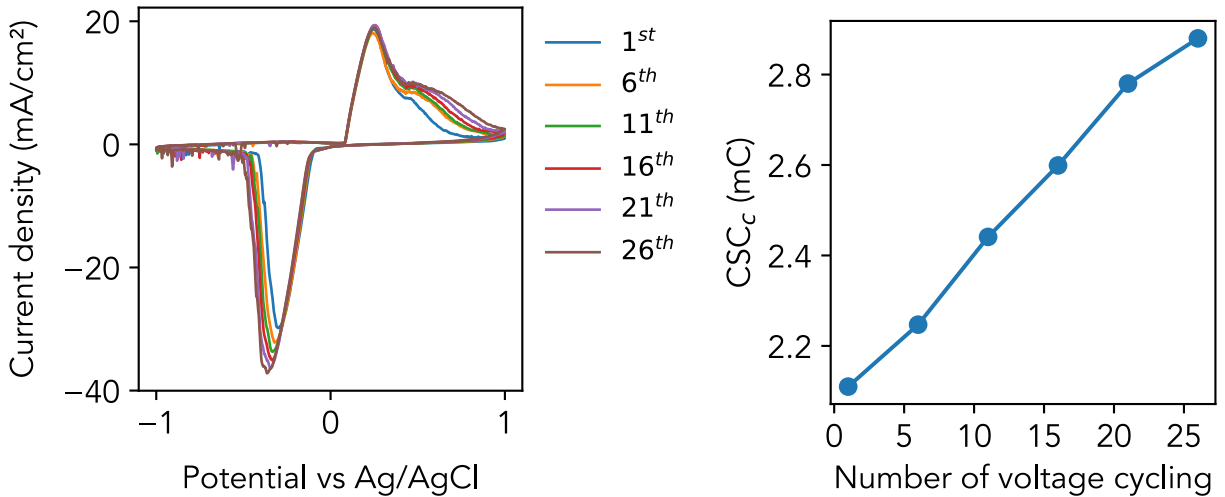
Figure 2.18 Cathodic charge storage capacity of stainless-steel electrode on E-band. (a) Cyclic voltammetry at the 1st , 6th, 11th, 16th, 21st, and 26th cycles of potential sweeps. (b) Increase in cathodic charge storage capacity with the increase numbers of potential sweeps.

Nevertheless, it is noted that only a fraction of the charge enclosed by the CV is practically available for injection by a short pulse. Only superficial layer of the electrode will actively be involved and therefore CSC overestimates the available charge. In practice, the charge injection capacity (CIC) per area is therefore examined to measure the maximum electrical charge density of a short pulse that can be injected safely across the electrode-electrolyte interface without causing tissue damage or electrolysis.

To conduct the CIC measurement, charge-balanced biphasic current pulses are given with a cathodic first phase to the electrode, and the transient voltage profiles across the working

electrode and counter electrode are recorded, as shown in Figure 2.19. If the Randles cell model is used to simplify the circuit, we can calculate the theoretical transient voltage and time constant of the circuit. The initial value of the voltage profiles is related to the solution resistant Rs, and the difference between steady-state voltage and initial voltage is related to the charge transfer resistance, Rct. Since the voltage across the electrical double layer is of interest, the voltage profile should take off the voltage drop contributed by the solution resistance and the modified voltage profile should not exceed the water window obtained from the CV curve. The maximum current set so that the voltage across electric double layer equals to the water window at the cathodic boundary. In the meantime, the anodic phase adjusted in duration so that the charge balance is secured and the voltage is smaller than the water window at the anodic boundary.

Both cathodic and anodic pulse duration was 1 ms. The magnitude of electric current ranged from 0.1 to 7 mA. The equivalent circuit model shows the estimate solution resistance in range of 104 and 112 Ω and the corresponding voltage drop of solution resistance becomes in range of 10.4 mV and 784 mV. After taking off the voltage drop contributed by the solution resistance, the modified water window for amplitude of 7 mA is shown in Figure 2.19 (b). The maximum CIC should be higher than 7 μC. For stability test, SEM and EDX analysis on a stainless-steel electrode were examined before and after 50 cycles of CV sweeps, as shown in Figure 2.20. Oxygen and phosphorus were found after 50 cycles of CV sweeps.
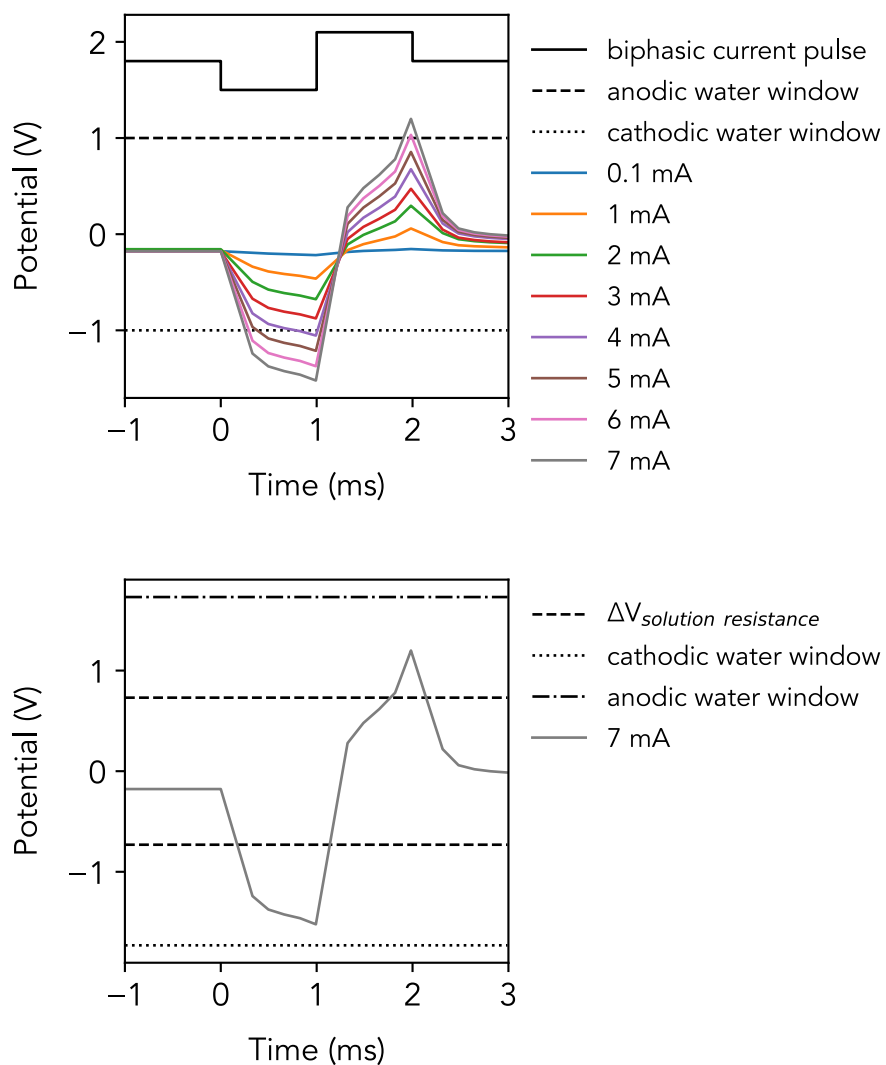
Figure 2.19 Charge injection capacity of stainless-steel electrode on E-band. (a) Without and (b) with the adjustment of the water window by considering the voltage drop across the solution resistance.

Element	Weight%	Atomic%
Cr	21.02	22.37
Fe	66.77	66.14
Ni	12.20	11.50
Totals	100.00	

Element	Weight%	Atomic%
O	2.99	9.57
P	1.03	1.70
Cr	17.80	17.54
Fe	66.12	60.66
Ni	12.07	10.54
Totals	100.00	
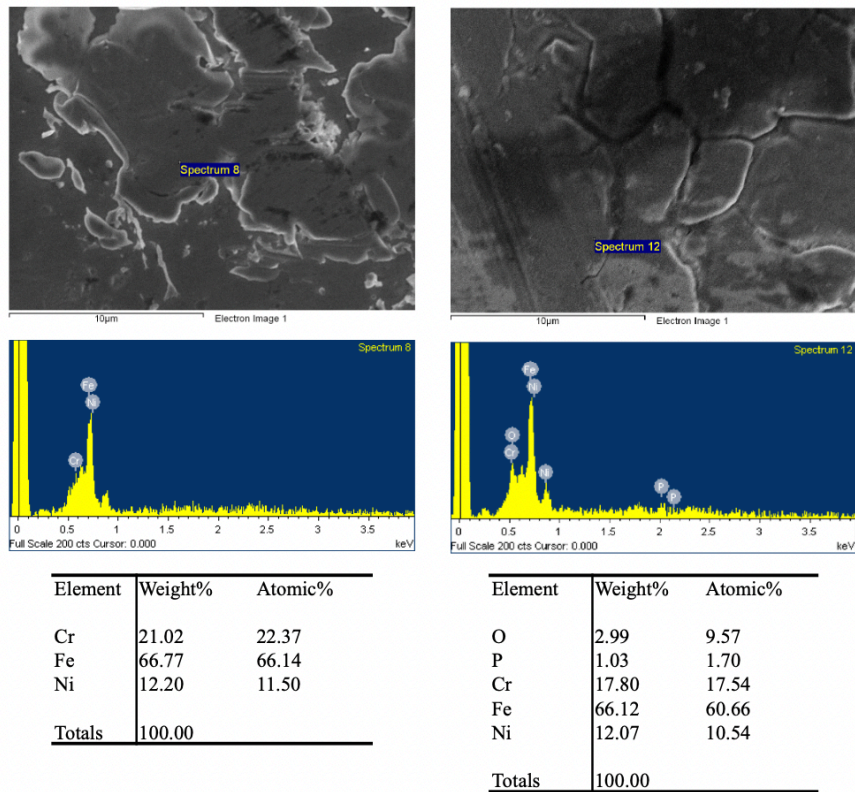
Figure 2.20 SEM and EDX analysis on stainless-steel electrode before and after 50 cycles of CV sweeps

Chapter 3 Ex-Vivo Animal Experiment

3.1 Introduction

The ultra-stretchable E-band has been demonstrated on slaughtered porcine samples for the functions of electrical stimulation, electromyography, and motility recordings. Animal experimental setup and experimental results are elaborated in this chapter.

3.2 Animal experimental setup

3.2.1 Perfusion system

A customer-designed perfusion system provided a passage of fresh physiological saline flowing through lumen of emptied intestines [91, 92] or surrounding chyme-filled intestines [93] to keep the tissue from dehydration and to supply nutrient to tissues, as shown in Figure 3.1. In order to preserve natural hydrodynamics of defecation [94] and intrinsic luminal pressure of intestines, partially digested food was suggested to be kept in the intestines for experiment. In fact, a minimum amount of luminal pressure was required to induce intestinal contraction and relaxation but too much luminal pressure will induce irregular contraction [92, 94]. Besides, the length and tension of the intestine segments affect the rate of propulsive motility and transit [95]. Therefore, in the experiment, 10-cm long intestines were hanged at two ends without longitudinal stretch, and were immersed in an organ bath with Krebs solution right below the surface of fluid to prevent the influence of extraluminal pressure applied to the tissues.
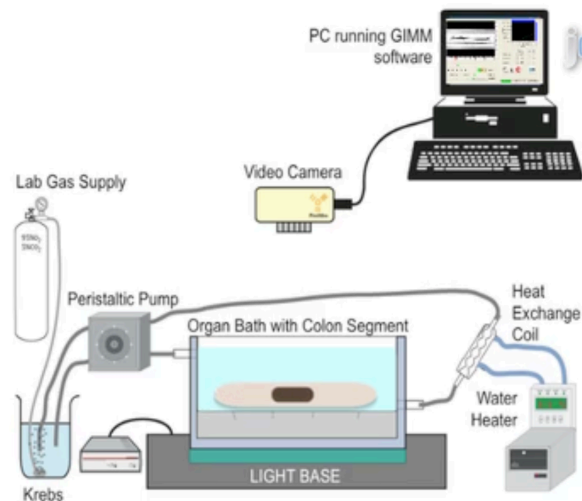
Figure 3.1 Customered perfusion system for porcine intestinal samples [93]

The small intestine segments were examined in an organ bath with Krebs solution. The Krebs solution contains sodium (Na), chlorine (Cl), potassium (K), calcium (Ca), magnesium sulfate (MgSO4), bicarbonate (HCO3), phosphate (PO4), and glucose. The composition of Krebs solution is shown in Table 3.1. The Krebs solution in main chamber was refreshed by a peristaltic pump at 10 ml/min, which was aerated with carbogen gas mixture (95% O2 + 5% CO2) for a minimum of 20 min to reach a pH of 7.4 and maintained between 33 and 37 degree C. The chamber was built with transparent acrylic for optical motility recording.

Table 3.1. Contents of Krebs solution

	NaCl	NaHCO3	KCl	KH2PO4	MgSO4.7H2O	Glucose	CaCl2
Molecular weight	58.44	84.007	74.5513	136.086	246.47	180.156	110.98
mmol/L	118	25	4.8	1.2	1.2	11	1.5
g/L	6.896	2.1	0.358	0.163	0.296	1.982	0.166

3.2.2 Tissue preparation

A bottle of fresh ice-cold Krebs solution bubbled with carbogen gas mixture (95% O2 + 5% CO2) was prepared for the preservation of intestinal tissue during transit and before experiment.

The porcine intestines were obtained 10 mins after of the slaughter of the animal from the slaughterhouse at New Taipei Meat Market (Shu Lin, New Taipei City, Taiwan). The intestine segments were kept in ice-cold Krebs solution and the adjoining mesentery of intestines were carefully removed using scissors before experiment, as shown in Figure 3.2. The anatomical regions of the collected porcine intestines include duodenum and proximal part of jejunum (starting at 10 cm from the pylorus, total length 1 m), and proximal part of the colon (starting at 10 cm from the ileal cecal valve, total length 1 m) [96]. The chyme, partially digested food, was left in the intestines with "porridge-like" consistency. The intestines were remained in ice-cold Krebs solution for up to 3 hours prior to experiment with the least tissue damage and were kept in 37-degree C Krebs solution during experiment.
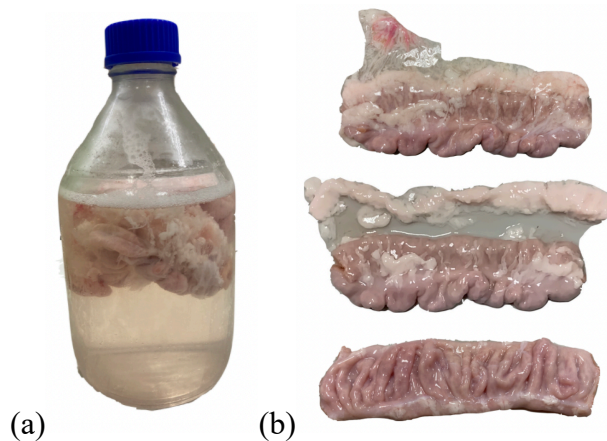

(a)   (b)

Figure 3.2 Preservation and preparation of slaughtered intestines for experiment. (a) Preservation of slaughtered intestines in a bottle of ice-cold Krebs solution. (b) Removement of adjoining mesentery before experiment.

3.2.3 Installation of electronic elastic band

In order to measure the contraction and relaxation of intestines, the e-band was used as a strain sensor as well as a pressure sensor to measure the deformation of intestine and intraluminal pressure, as shown in Figure 3.3. An e-band with 10 % pre-stretch was wrapped around the intestines and was used to capture the shortening and expansion of the perimeters of intestines during contraction and relaxation movement. Due to the fact that the gastrointestinal tract is a hollow structure, stress produced by the circumferential pre-stretched e-band deforms the shape of the intestine. Although the pre-stretched e-band was not soft enough to preserve the real deformation of the intestine, it is capable of measuring the intraluminal pressure. The intraluminal pressure is related to the stress experienced by the tissue wall and pre-stretched e-band by the law of Laplace [81-83]; the stress of the e-band is related to the deformation of tissue; and herein the deformation corresponds to the electric resistance of the strain sensor. Hence, a pre-stretched e-band was used as a strain/pressure sensor for motility recording.

Here is the procedure to fix the e-band on intestines and remove upon need.

1. Measure the perimeter of intestine segment of interest. Refine the length of E-band by cutting the anchor sites of E-band by blade so that 110% of it is equal to the perimeter. The two ends of the e-band loop are 1cm wide and used as anchor sites to form a close loop.

2. Interconnect the E-band with thin stainless-steel wires, cap the inlets by PDMS slabs, and clamp each interconnection site by two acrylic plates with screws. Pre-stretch the e-band by 10 % and lay it on a A4 paper with electrode side up.

3. The electrode sites are coated by a thin layer of tissue adhesive (3M vetbond). It is a proven adhesive for veterinary procedures that can stop minor bleeding, seal suture line and bond tissue together without the need for sutures.

74

4. Wipe the surface of the intestine segment and place it on the pre-stretched E-band. Circle the e-band around the segment to form a close loop. The liquid adhesive polymerized in second after contact with tissue or body fluid and became solid. Hence, no shifting was occurred at electrode and anchor sites. The adhesive is impervious to water and create strong bond between silicone and tissue even in aqueous solution.

5. Wet the intestine and E-band with 37-degree Krebs solution and move them to an organ bath for animal experiment.

6. The E-band was then peeled off carefully after experiment with the adhesive attached. It was cleaned up by dissolving the adhesive in organic solvent such as acetone and became reusable.

7. Alternative fixing approach. Instead of using tissue adhesive, the anchor sites can be sandwiched by two slabs of PDMS and tie a knot by a thread to fix the length of the E-band. However, the electrode sites could move during experiment.
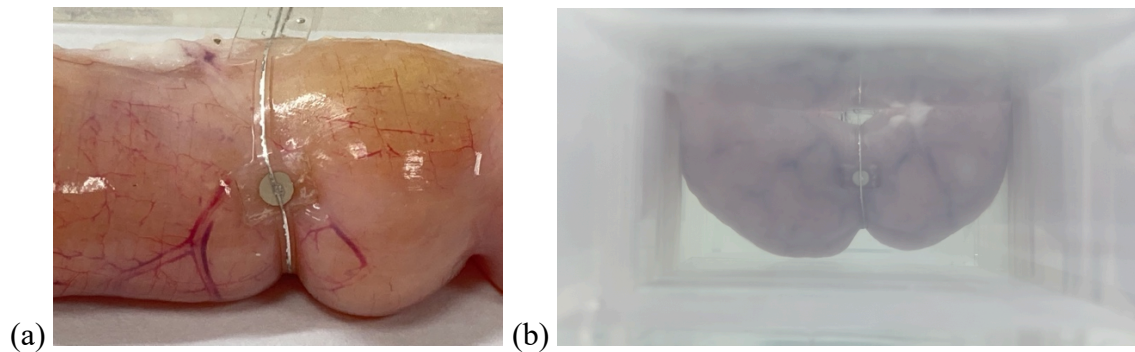

(a)   (b)

Figure 3.3 Installation and fixation of e-band on small intestine segment. (a) Two stainless-steel electrodes were glued on the small instestine segment. (b) Electrode immersed in the Krebs solution.

3.3 Experimental results

The platform utilizes arrays of electrodes and electrical strain sensors on a stretchable and conformal elastomer wrapped around intestines. All the components are connected by stretchable liquid metal wires embedded in the elastomer and linked to thin stainless-steel wires as interfaces to electronic systems. Sensing and stimulation electrodes are uniformly dispersed in axial and radial directions of the intestine to record electrical activities of SMCs and provide various stimulation configurations, respectively. Since SMCs contract and relax in both radial and longitudinal directions, stretchable strain sensors sensing sensors are designed to measure deformed circumferences and lengths along axial direction. The electronic system for the platform provides flexible stimulation configurations and concurrent real-time data acquisition. The data will be analyzed to interpret the relation between electrical and mechanical activities involved in the digestive processes, such as segmentation, mixing, and transport.

A material test system with 2 kN load cell (C42.503, Criterion Electromechanical Test System, MTS) was used to examine the compliance of tissue and E-band by load-strain curves. A multimeter (GDM-8261A, Dual Measurement Multimeter, GW Instek, Taiwan) was used to measure the electric resistance of strain sensor. A data acquisition system (MP36, BIOPAC Systems, Inc.) or an affordable electromyography sensor (MyoWare Muscle Sensor, Advancer Technologies) was used to record and amplify surface electric activity of smooth muscle cells to detect muscle activation via electric potential. The MyoWare sensor was compatible with most development boards and Arduino was used to control it. A precision impedance analyzer (6500B, Wayne Kerr Electronics) was used to measure tissue impedance.

3.3.1 Compliance

The mechanical properties of intestinal tissues obtained from slaughtered pigs was examined by a material test system with 2 kN load cell (C42.503, Criterion Electromechanical Test System, MTS). The stretching speed ranged from 100 mm/min to 600 mm/min. The sampling rate was xxx. Uniaxial tension tests were performed to determine the effect of E-band wrapped around intestines. Ultimate strength, elongation at failure, and elastic modulus of intestinal tissue and E-band were derived from the tests and analyzed.

The collected porcine intestine specimens include duodenum and proximal part of jejunum (starting at 10 cm from the pylorus, total length 1 m), and proximal part of the colon (starting at 10 cm from the ileal cecal valve, total length 1 m). The chyme in the lumen of the intestinal tissues were emptied and the slaughtered tissue specimens were stored in Krebs solution at 4 degree C for 18 hours and were warmed up to 37 degree C prior to mechanical tests. Excess fat, connective tissue, and mesentery were removed by scissors. The specimens were laid open and divided into rectangular specimens with natural length of 1cm x 8 cm (falling in the direction of gravity) and with long-edge side parallel to the axial direction of the intestines. Each side of the specimens were sandwiched by two slabs of PDMS and clamped by the holding grips of the material test system for tensile testing.

The appearance of muscularis propria are different in small intestines and large intestines. The muscularis propria is responsible for the main propulsive forces in the intestinal wall and is consisted of inner circular smooth muscle and outer longitudinal smooth muscle [41]. The former and the latter control the intestinal movement in radial and axial directions, respectively. At the end of small intestines, the longitudinal muscle layer starts to concentrate into three bands, called taeniae coli, on cecum and continuously visible on ascending, transverse and descending colons.

It further reduces to two bands on sigmoid colon and no band left on rectum. In fact, the lengths of circular muscle layers vary and are longer than its adjoining taenia coli. The taeniae coli run the entire length of the colon and force the circular muscle layers to form random shape of sacculation, as shown in Figure 3.4. The taeniae coli was much stiffer and less stretchable than the adjoining smooth muscle layer [97]. Since the compliance and stiffness of E-band on soft tissue is of interest, the taeniae coli was removed in the mechanical tests.
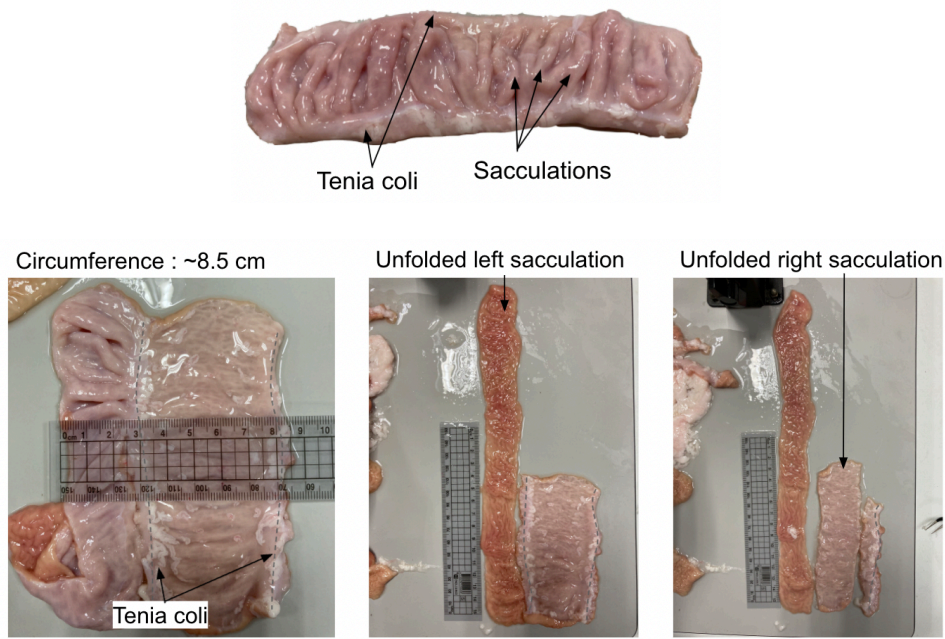
Figure 3.4 Image of taeniae coli and sacculation of large intestine

Figure 3.5 shows the load-strain curves of E-band, small intestines, small intestines with E-band attached, large intestines (without taeniae coli), and large intestines (without taeniae coli) with E-band attached. The ultimate strength, elongation at failure, and elastic modulus of the materials are summarized in Table 3.2. From the results, the small intestine is stiffer than large

intestine and the influence of E-band stiffens the small intestines. The data is similar to the literature reports [97, 98].

Table 3.2 Mechanical properties of E-band and intestinal tissues with and without E-band

	E-band	Small intestine	Small intestine w/ e-band	Large intestine	Large intestine w/ e-band
Ultimate strength (N/m)	54.8	619.6	538.1	370.7	448.1
Strain at failure	1.95	0.53	0.54	0.89	0.98
Slope (N/m) (<10% strain)	20.6	146.81	290.43	57.67	103.34
MSE	9.93	14.15	28.55	10.27	11.23

(a)

(b)

(c)

80
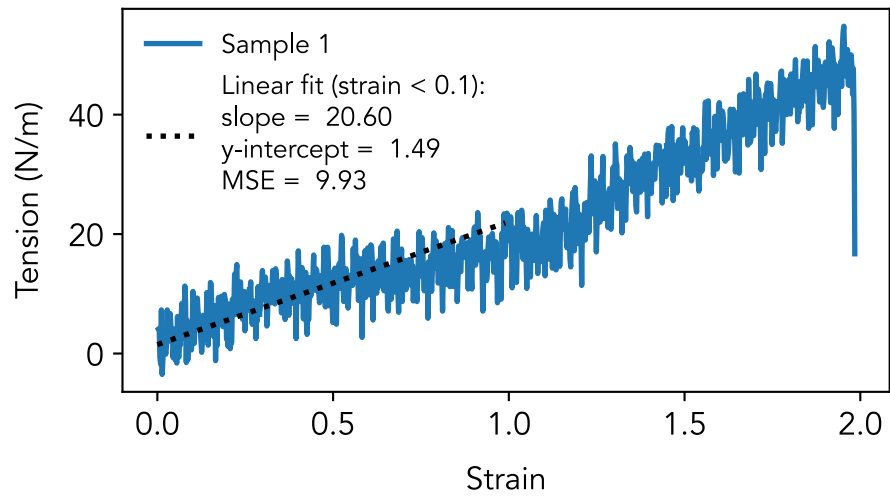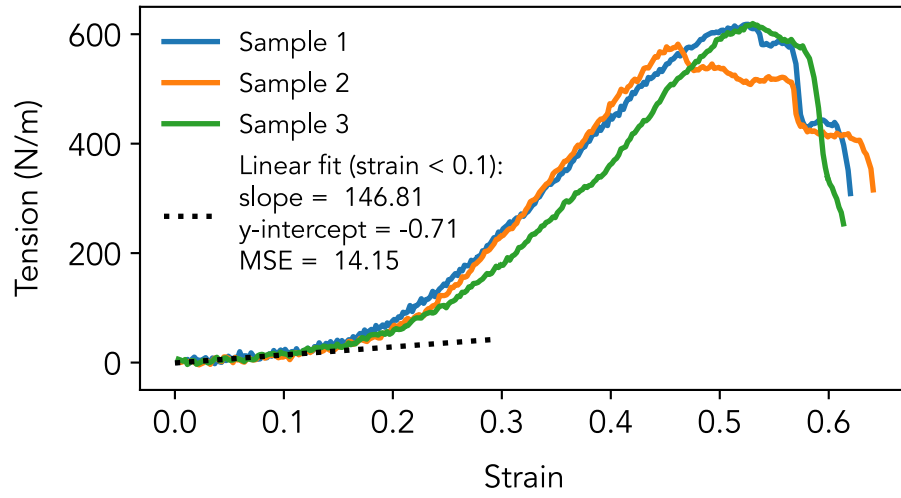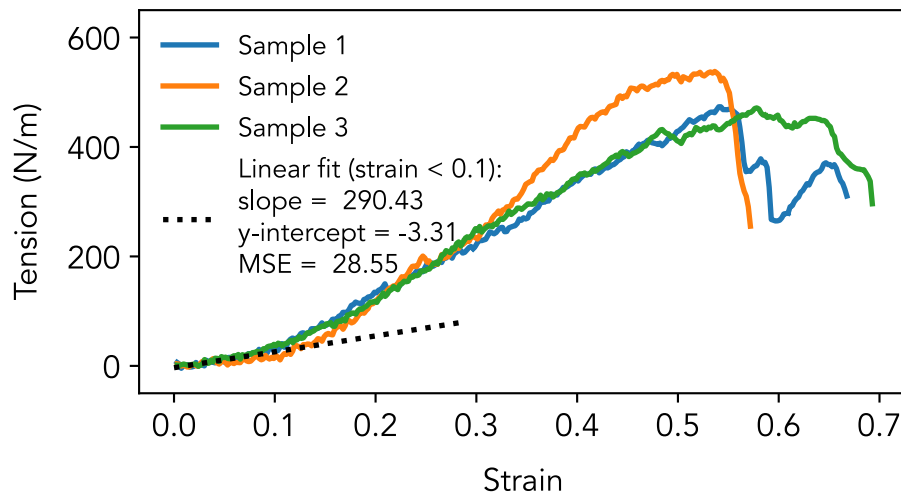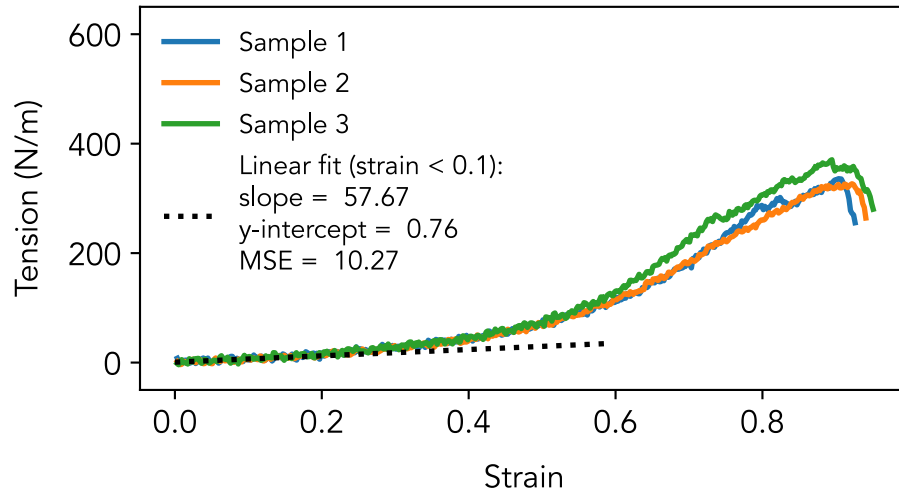
(d)
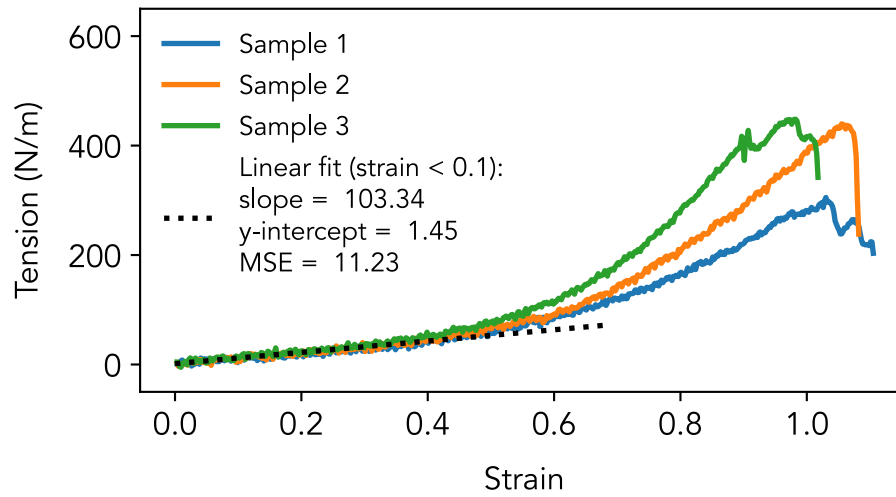
(e)

Figure 3.5 Tension versus strain curve of e-band and porcine intestine segments with inear fitting for strain below 0.1. (a) E-band. (b) Small intestine. (c) Small intestine attached with an e-band. (d) Large intestine. (e) Large intestine attached with an e-band.

Due to the fact that the intestinal pressure remains relatively constant for mammals [94], the averaged intraluminal pressure of 20 mmHg in human jejunum is used as a reference for the justification of compliance [99, 100]. According to the law of Laplace, the stress experienced by the E-band is proportional to the intraluminal pressure and radius of lumen and is inversely proportional to the thickness of E-band. The stress can be further converted to force load by multiplying the cross-sectional area of E-band. The E-band is 1 mm wide and 140 um thick. The radius of the porcine small intestine is 1 cm. The calculated force applied on the E-band is equal to 26 mN, which corresponds to 10% stretch of the E-band, as shown in Figure 2.10. Therefore, within 10% stretch, the E-band will be compliant to intestinal motility.

In the experiment, E-band was pre-stretched by 10% and anchored on the surface of intestine by tissue adhesive. The stress induced by the pre-stretched E-band deformed the intestine due to the nature of the soft and hollow structure. The pre-stretched E-band was able to monitor the contraction and relaxation of the bowel movement.

Food undergoes mechanical and chemical digestion in the gastrointestinal tract. Peristaltic contraction and hydrochloric acid in stomach breaks down bolus into chyme. Together with bile from the gallbladder and enzymes from the pancreas, the chyme is digested in small intestines by segmentation, mixing, and transport. Undigestible chyme and water enter large intestines and are absorbed and compacted into semi-solid feces. From the slaughtered porcine samples, small intestine segments were filled with chyme and no feces was found in the large intestine segments. Therefore, in the following experiment, small intestines were used for demonstration.

3.3.2 Strain gauge and pressure sensor

The electrical resistance of the E-band strain sensor was measured by a multimeter (GDM-8261A, Dual Measurement Multimeter, GW Instek, Taiwan). As a serial terminal device, the multimeter was communicated to PC via a RS232-USB interface cable at baud rate of 115200. The multimeter also adopted a scanner card (GDM-SC1A, GW Instek, Taiwan) for a maximum of 16-channel recordings. An official Microsoft Excel Add-ins and NI LabView driver supported single channel and multi-channel settings and data logging of the multimeter and scanner card. The maximum sampling rates were 10 Hz and 0.5 Hz for single channel via Excel Add-ins and 3-channel recordings via LabView, respectively. Higher data logging rate or sampling rate should be achieved by optimizing the LabView programs.

Multiple E-bands were wrapped around slaughtered porcine intestinal tissues to measure the peristalsis movement and wave propagation, as shown in Figure 3.6. The anchor sites of each E-band were sandwiched by two slabs of PDMS and was tied in a knot by a thread to fix the length of the E-band. The resistance change during the peristalsis movement was related to the strain difference of strain sensor, which is further related to the pressure difference by the law of Laplace.
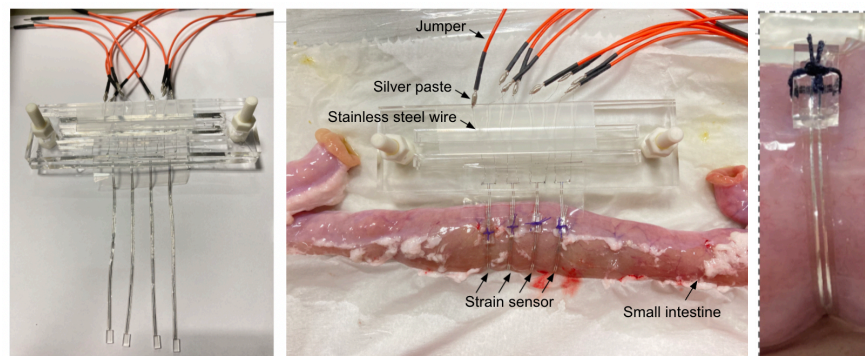

Figure 3.6 Installation of E-bands on small intestine segment

Peristalsis movement of the intestines occurs at frequencies of 7-20 cycle per minutes [99]. As shown in the Figure 3.7, the frequency of the slow wave was 7 cycles per minutes. The slow wave frequency was paced by external stimulation control with voltage pulse of 100 Vpp at 100 Hz for 30 sec and increased to 14 per minute.
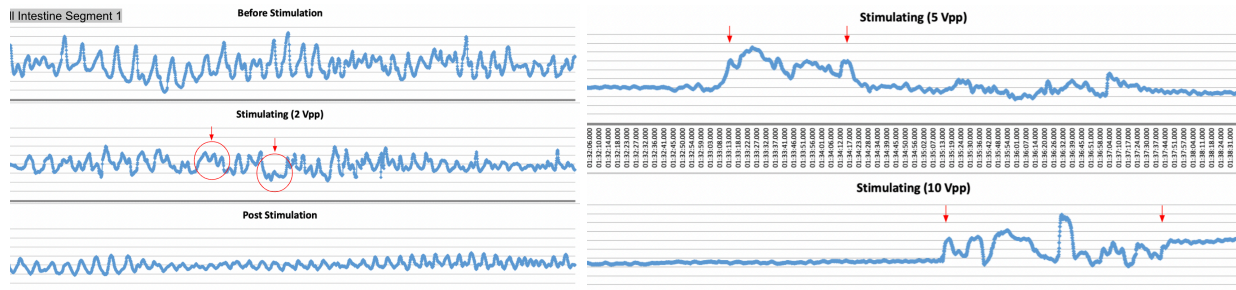
Figure 3.7 Peristalsis movement of small intestine segment measured by strain sensor of e-band

Figure 3.8 shows the large area propulsive movement of the small intestine segment. Four strain sensors were located 1 cm away from each other. The peristalsis movement was induced by external biphasic voltage pulses with amplitude of 300 Vpp, pulse duration of 1 ms, and frequency of 100 Hz. The stimulation pulses were applied adjacent to the strain sensor #4, #3, #2, and #1 sequentially. The contraction movement in radial direction shortened the diameter of lumen and the strain sensor and resulted in the decrease of electrical resistance, while the contraction movement in longitudinal direction shortened the local intestine segment in longitudinal direction and cause the increase of the intestine thickness, diameter of lumen, and therefore the electrical resistance. Experimental data with electrical stimulation and control data with intrinsic movement obtained 4 mins after the experiment. The peak resistances of the four strain sensors have time delay, which implies a propulsive movement of the intestine was induced. Among all, the strain

sensor #4 captures both the contraction and relaxation behaviors and the baseline resistance of the experiment and control data remains the same.
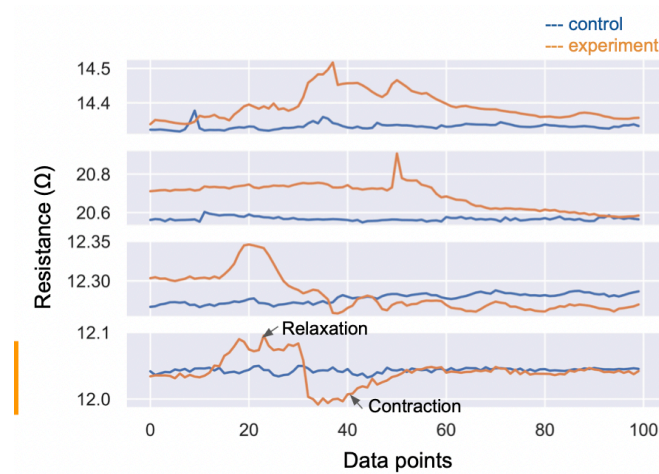
Figure 3.8 Propulsive movement of small intestine segment measured by strain sensor of e-band

Figure 3.9 shows the two directional motility recording. There were three strain sensors that cross each other, including two circumferential strain sensors #1 and #2 and one 3-cm long longitudinal strain sensor #3. Stimulation pulses were applied at two ends of intestine segment by external biphasic voltage pulses with amplitude of 200 Vpp, pulse duration of 1 ms, and frequency of 100 Hz. The electric current passed through the intestine segment and triggered the longitudinal muscles at two ends of the segment contract. Therefore, the strain sensor #2 was elongated in longitudinal direction and resulted in the increase of the resistance. In the meantime, the intestine segments nearby the strain sensor #1 and #2 relaxed or distended and contracted in radial direction and cause the resistance to increase and decrease. Small oscillations of resistance due to slow wave were observed in the data.

85
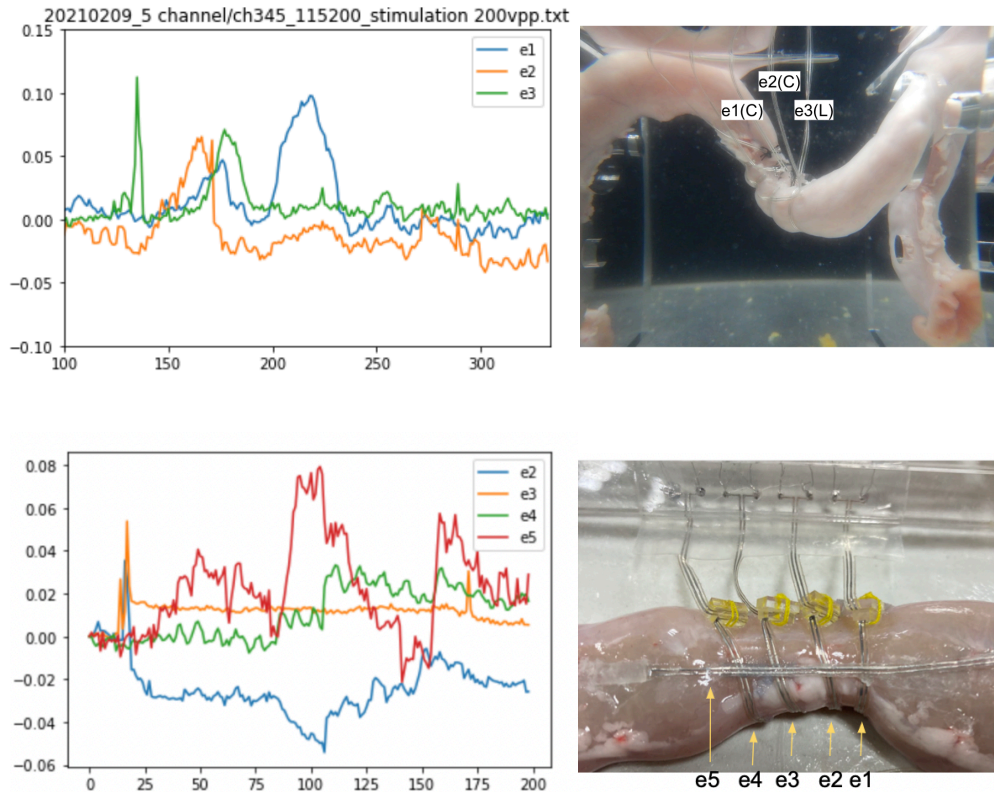
Figure 3.9 Two directional motility recording measured by strain sensor of e-band

Figure 3.10 shows the large area concurrent movement of the small intestine segment. Strain sensor #1, #2, #3, and #4 were located 1 cm away from each other and # 3 was disconnected. The movement was induced by external biphasic voltage pulses with amplitude of 100 Vpp, pulse duration of 1 ms, and frequency of 100 Hz. The stimulation pulses were applied adjacent to the strain sensor #4. The highest and lowest resistances of the three strain sensors happened at the same time, which implies a large area concurrent movement of the intestine was induced. Strain sensor #1 and #2 relaxed while strain sensor #4 contracted.
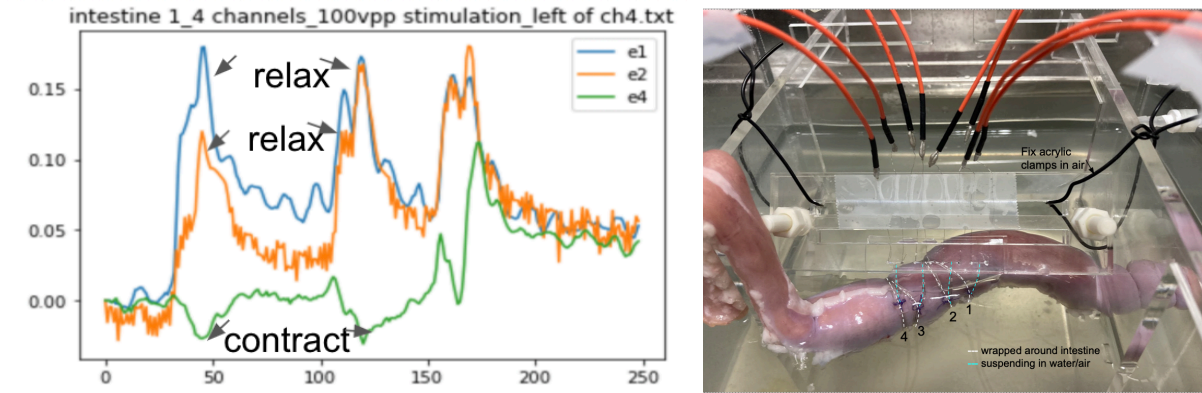
Figure 3.10 Concurrent movement of small intestine segment measured by 3 e-bands

Besides, the difference in baseline resistance induced by the electrical stimulation is owing to the increase of intraluminal pressure. From the law of Laplace in Equation 2.1-2.10, the intraluminal pressure is proportional to the stress experienced by the E-band and the thickness of E-band and is inversely proportional to the radius of lumen. The stress can be obtained from the resistance change of the E-band. The universal normalized resistance-strain curve for strain below 10% relates the normalized resistance to strain. The load-strain curve for strain below 10% relates the strain to the force load applied to the e-Band. By applying the parameters shown in Table 3.3, Figure 3.11 shows the relationship of transmural pressure versus electrical resistance and strain, respectively.

Table 3.3 Parameters used for the transmural pressure calculations

Parameter	m_T	T_0	m_R	$R_{n,0}$	R_{min}	R_{max}	L	h
Value	290.43 (N/m)	-3.31 (N/m)	0.3	0	27.1 (Ω)	33.2 (Ω)	4 (cm)	1

(a)   (b)
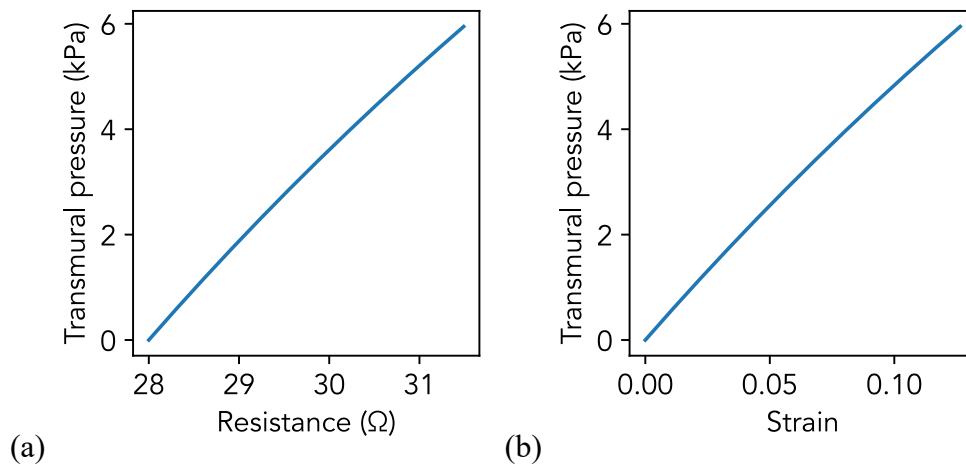
Figure 3.11 Experimenral transmural pressure versus strain curve. These parameters are used for the experiment in Figure 3.12.

3.3.3 Gastrointestinal electrical stimulation

The chronopotentiometry (CP) of the three-electrode system of potentiostat (SP150, BioLogic) was used to provide 100 Hz biphasic current pulses with a cathodic first phase to the electrode. Both cathodic and anodic pulse duration was 1 ms. The magnitude of the electric current ranged from 0 to 10 mA. Meanwhile, electrical resistance of E-band strain sensor was measured by a multimeter (GDM-8261A, Dual Measurement Multimeter, GW Instek, Taiwan). As a serial terminal device, the multimeter was communicated to PC via a RS232-USB interface cable at baud rate of 115200. An official Microsoft Excel Add-ins supported single channel settings and data logging of the multimeter with the maximum sampling rate of 10 Hz.

The working electrode and counter electrode of the potentiostat were connected to the two stainless-steel electrodes of the E-band separately, which were spaced 1.8 ~ 2 cm apart in the circumferential strain sensor. The reference electrode was shorted to the counter electrode. The tissue was immersed in 37 degree Krebs solution.
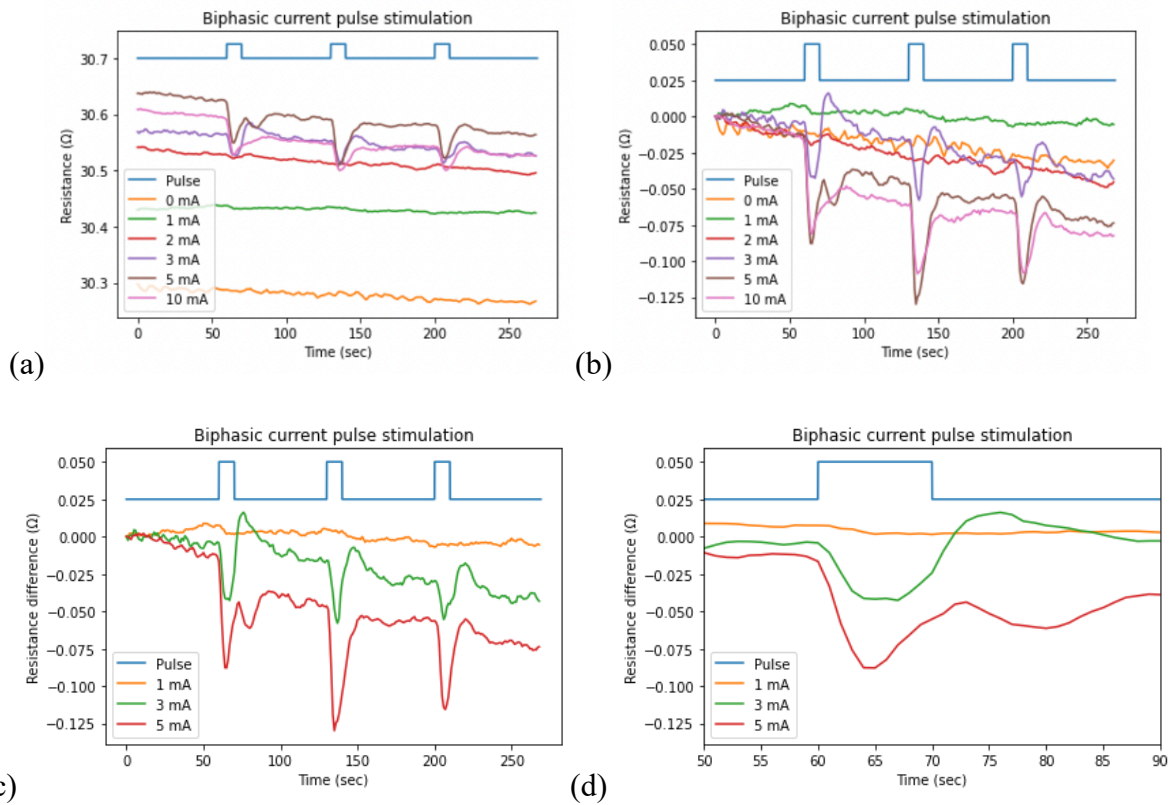
Figure 3.12 Real-time motility recording induced by electrical stimulation with various amplitudes of biphasic current pulses. (a) Raw data. (b) Baselined raw data by the first data. (c) Three different motility behaviors. (d) Contraction and relaxation are active after stimulation.

Figure 3.12 shows the real-time motility recording induced by electrical stimulation with various amplitude. 100 Hz biphasic current pulses were applied for 10 sec and turned off for 1 min and repeated for 3 times. Both cathodic and anodic pulse duration were 1 ms. The magnitude of the electric current ranged from 0 to 10 mA. The shifts of the baseline show the difference in the diameter of lumen and intraluminal pressure. Different amplitude of current pulses varies the strength and patterns of the induced contraction and relaxation movement. The curves with current amplitude below 3 mA do not show significant contraction nor relaxation. When 3 mA of current

pulses flow between two electrodes, contraction movement was induced and followed by relaxation movement. The motility pattern was repeatable for 3 times. When 5 mA and 10 mA of current pulses were applied, repeatable contraction movement was induced. The former shows even higher difference in resistance than the latter. The zoom in figure shows the 10 sec stimulation pulses induce intestinal movement for about 30 sec.

3.3.4 Biopotential recordings

A data acquisition system (Channel 3, MP36, BIOPAC Systems, Inc.) or an affordable electromyography sensor (MyoWare Muscle Sensor, Advancer Technologies) was used to record and amplify surface electric activity of smooth muscle cells to detect muscle activation via electric potential. The MyoWare sensor was compatible with most development boards and Arduino was used to control it. Meanwhile, electrical resistance of E-band strain sensor was measured by a multimeter (GDM-8261A, Dual Measurement Multimeter, GW Instek, Taiwan). As a serial terminal device, the multimeter was communicated to PC via a RS232-USB interface cable at baud rate of 115200. An official Microsoft Excel Add-ins supported single channel settings and data logging of the multimeter with the maximum sampling rate of 10 Hz.

An E-band was wrapped around the intestine. The two inputs of the data acquisition system (red and white lead) were connected to the two electrodes of the E-band fixed circumferentially on the intestine segment and the ground electrode (black lead) was connected to one end of the intestine segment. In the circuit of the acquisition system, the two electrodes were connected to the inputs of a differential op amplifier, followed by pre-amplifiers, filters, post-amplifiers, and etc. The BIOPAC measured the potential difference between the two electrodes of the E-band and displayed as EMG and integrated EMG data. Different band pass filters were later on applied to

the signal, including 0-2 Hz, 0-0.3 Hz, 0.3-0.75, and 5-10 Hz, where 0-0.3 Hz and 5-10 Hz correspond to the slow wave and spikes activity, respectively, as shown in Figure 3.13. The spikes come along with the peaks of the slow waves and correlates to the onset of contraction movement. The position of the two electrodes renders the biopotential profile. The multimeter measured the resistance of the strain sensor of the same E-band.

Figure 3.14 shows the surface EMG and strain sensor recordings of a healthy intestine segment (3.5 hours after slaughter) by BIOPAC. The slow wave occurs at around 7 cycles per minute, which is the frequency of oscillation of depolarization and repolarization of membrane potential of smooth muscle cells.

Figure 3.15 shows the surface EMG and strain sensor recordings of a dying small intestine segment (10 hours after slaughter) by BIOPAC. The slow wave occurs at around 12 cycles per minute. No significant correlation to the electric resistance measurement. The extracellular electrodes successfully capture the surface EMG when there is no obvious contraction movement. These data further state that the surface EMG is not the motion artifact from the intestine [44].
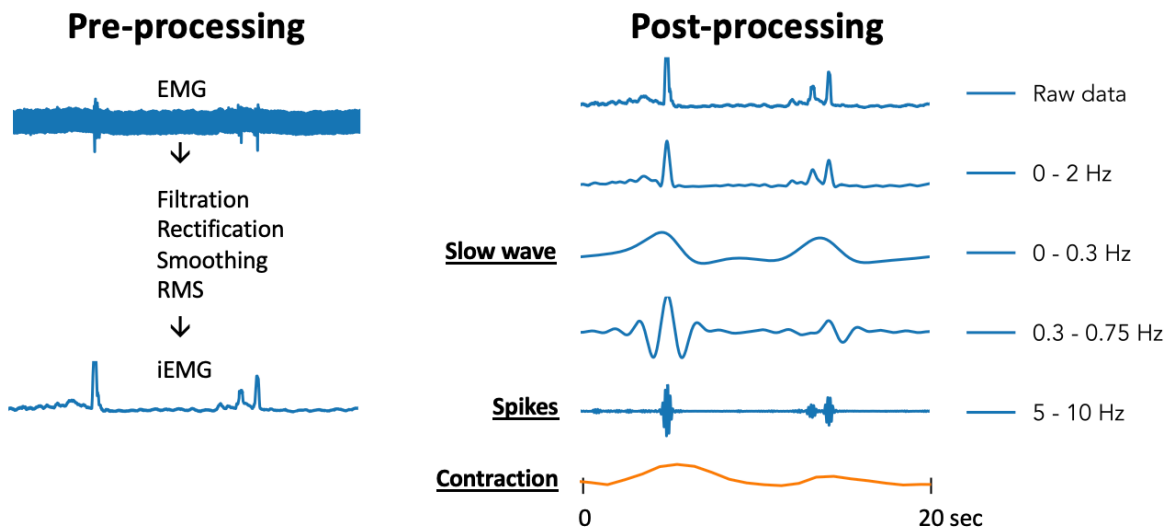
Figure 3.13 Pre-processing and post-processing of EMG signal

91
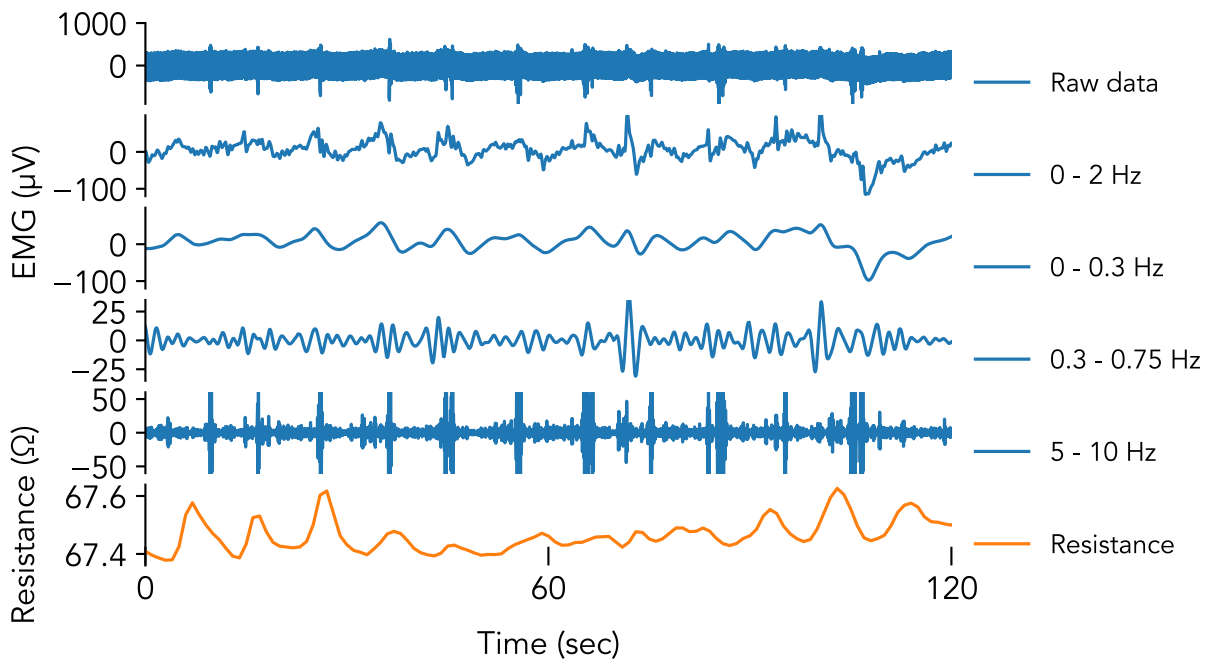
(a)
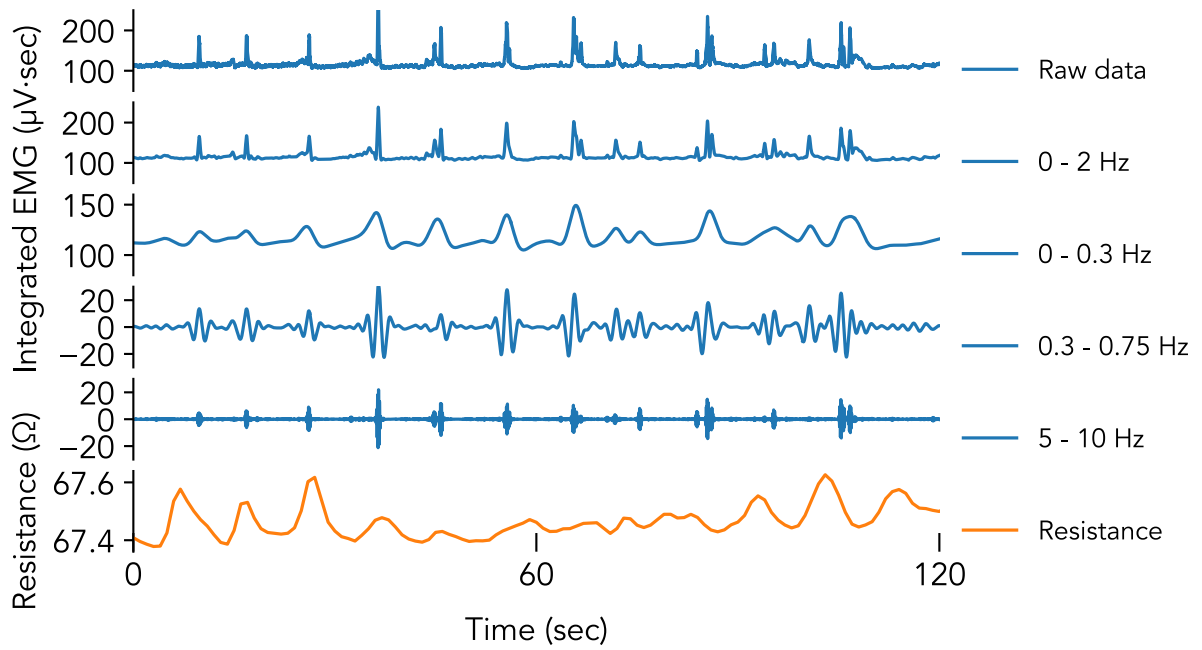
(b)
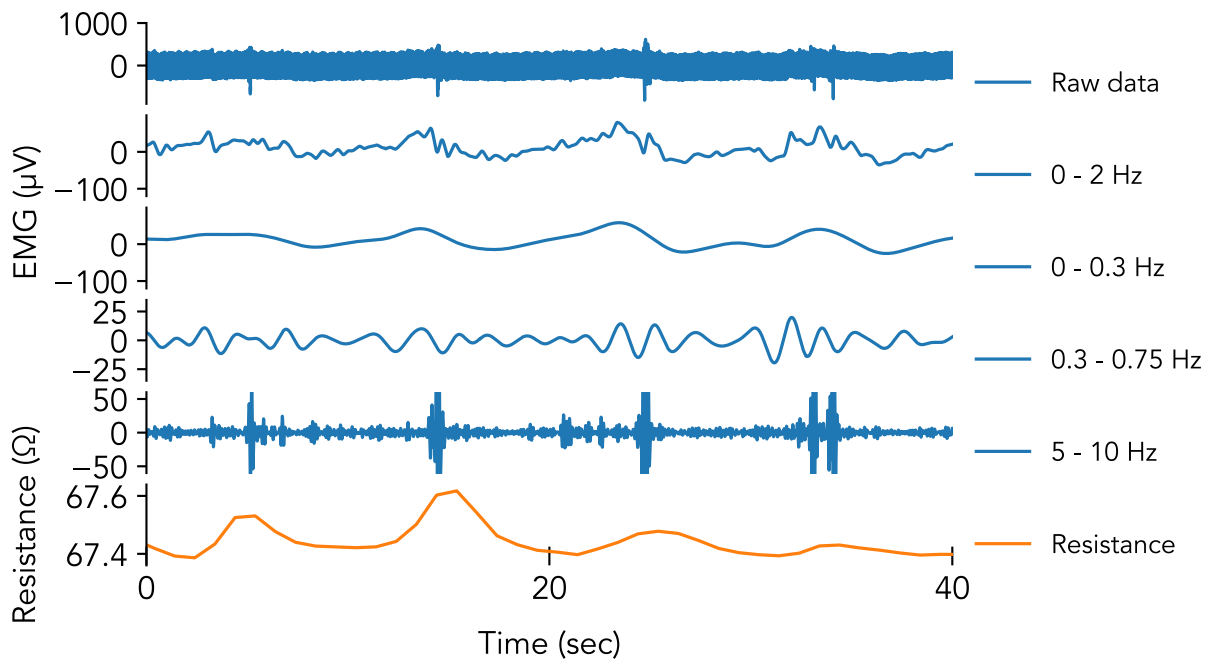
(c)

(d)

Figure 3.14 Concurrent recording of surface EMG and electrical resistance of strain sensor on a healthy small intestine segment with different filtering. (a) EMG signal. (b) Integrated EMG. (c)

and (d) show the contraction movement was initiated at the onset of spikes from EMG and integrated EMG, respectively.

(a)

(b)
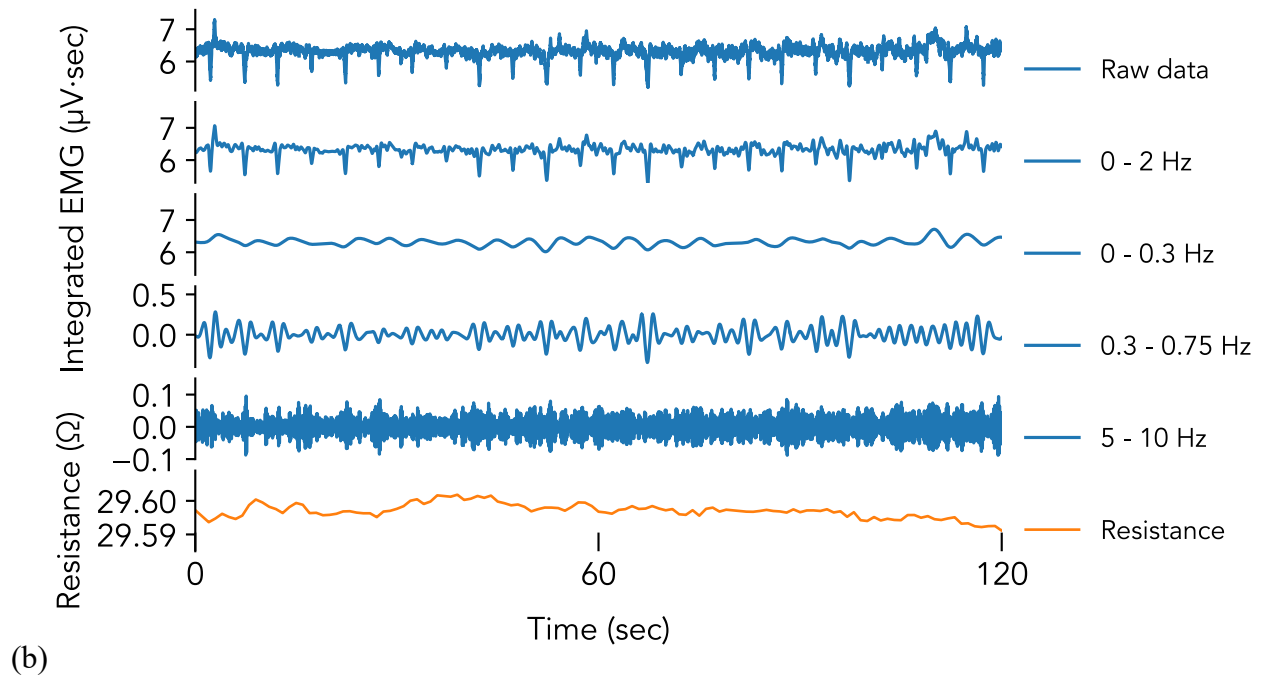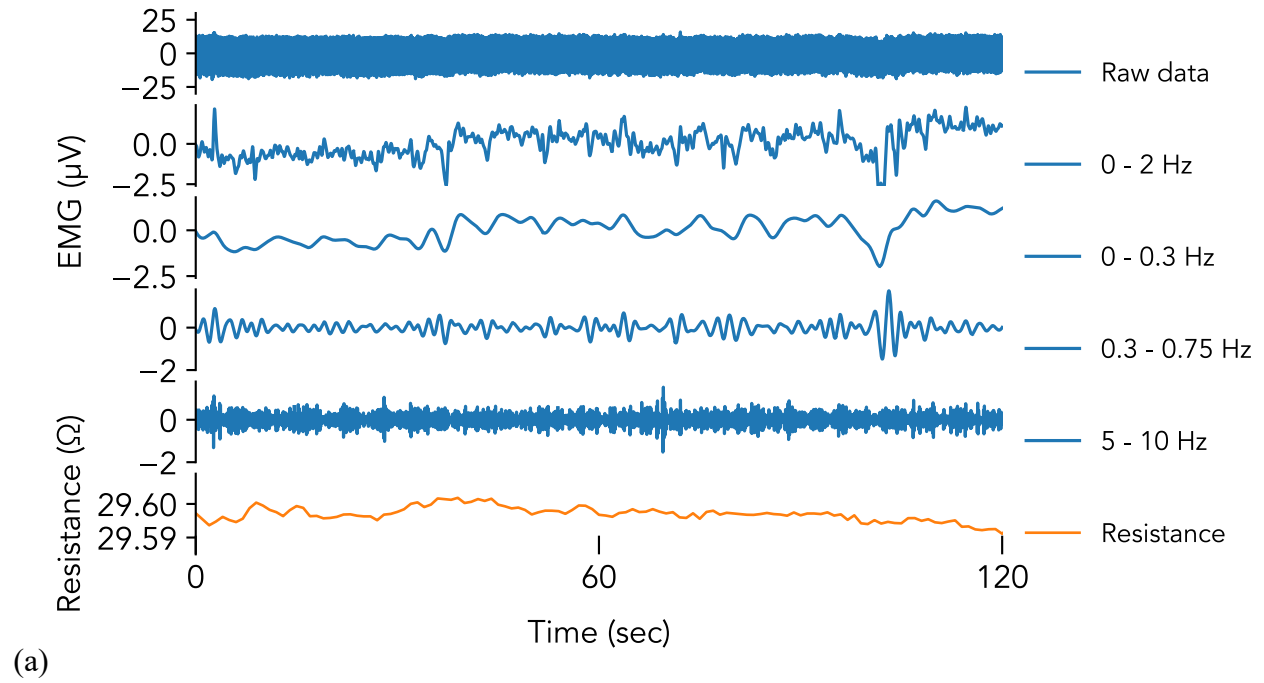
Figure 3.15 Concurrent recording of surface EMG and electrical resistance of strain sensor on a dying small intestine segment with different filtering. (a) EMG signal. (b) Integrated EMG.

3.3.5 Tissue impedance recordings

A precision impedance analyzer (6500B, Wayne Kerr Electronics) was used to measure tissue impedance at 1 kHz with sampling rate of 4 Hz. Meanwhile, electrical resistance of E-band strain sensor was measured by a multimeter (GDM-8261A, Dual Measurement Multimeter, GW Instek, Taiwan). As a serial terminal device, the multimeter was communicated to PC via a RS232-USB interface cable at baud rate of 115200. An official Microsoft Excel Add-ins supported single channel settings and data logging of the multimeter with the maximum sampling rate of 10 Hz.
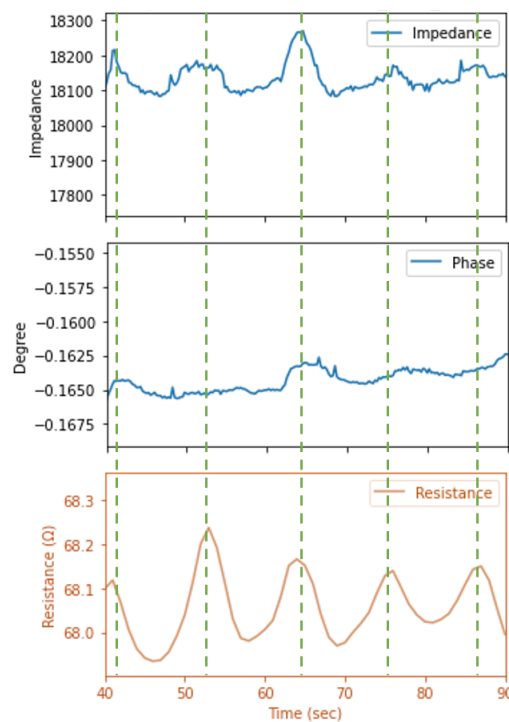
Figure 3.16 Concurrent recording of tissue impedance and electrical resistance of strain sensor on a healthy small intestine segment.

The impendence analyzer measured the tissue impedance between the two electrodes of the E-band. The multimeter measured the resistance of the strain sensor of the same E-band. Figure 3.16 shows the tissue impedance and strain sen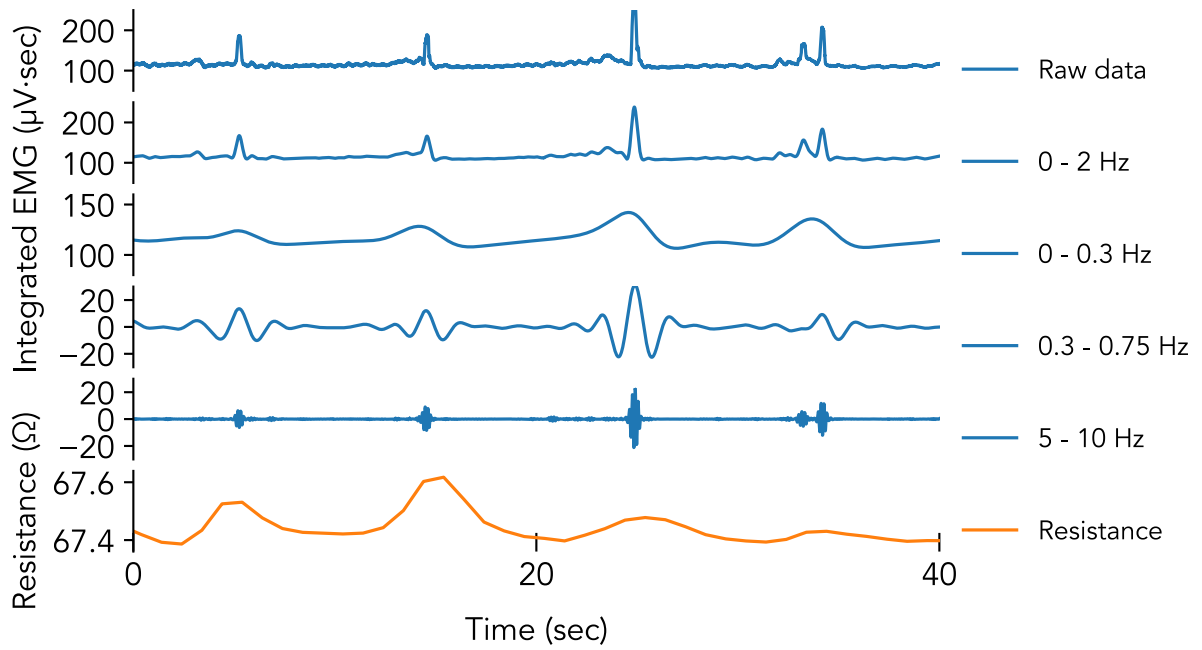sor recordings of a healthy intestine segment (4 hours after slaughter). When the lumen of the small intestine and local intraluminal pressure increase, the distance between two electrode increases as well as the tissue impedance.

3.3.6 Discussion

From our results, e-band has successfully stimulated the contraction and distention of small intestine. Meanwhile, the arrangement of the bipolar electrodes has been successfully measured EMG signal, which show good alignment of slow waves and spikes activity, as well as spikes activity and contraction movement. Moreover, the circumferential tissue impedance is well aligned with the contraction movement. This provides a promising tool for longitudinal motility recording without the installation of longitudinal e-bands.

If multiple e-bands are installed on the intestine segments, circumferential mobility and electrical activity can be recorded by the circumferential strain sensors and electrodes, respectively, and longitudinal mobility and electrical activity can be recorded by any two electrodes arranged in the longitudinal directions, as shown in Figure 3.17. This could allow two-dimensional mapping for both electrical activity and mechanical activity.
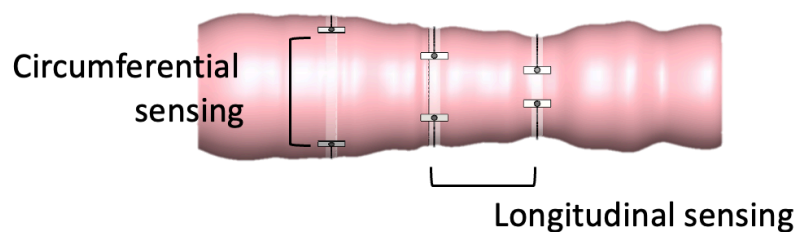
Figure 3.17 Two-dimensional recording of tissue motility and electrical activity.

96

Chapter 4 Conclusion and future opportunities

To summarize, the success of the project offers an impact on the understanding of underlying concurrent electrical and mechanical responses of SMCs and the development of electrical therapy through our GI neuromuscular stimulator for different GI disorders.

For long-term and large-area bioelectronic interfaces for the GI tract, multiple miniaturized E-bands should be accompanied with optimized interconnection techniques, efficient power consumption and sufficient power supply, and customized integrated circuitry that is capable of remote-control electrical stimulator, and wireless recording and transmission of electrical resistance of strain sensor, electromyography and tissue impedance, as shown in Figure 4.1.

Moreover, based on the electromechanical behaviors of the strain sensor, machine learning models will be applied to reverse engineer and predict waveforms of contraction and relaxation for circular and longitudinal smooth muscle cells, respectively. This information can further interpret the roles of the circular and longitudinal muscle cells involved in the digestive processes.
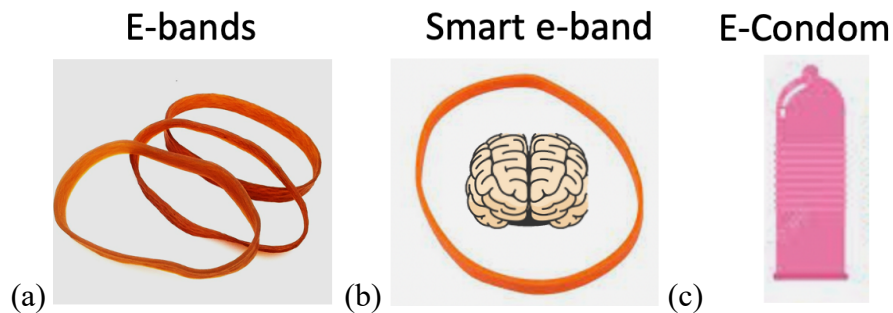
Figure 4.1 Future opportunities. (a) Installation of multiple e-bands on animal samples for two-dimensional mapping of electrical and mechanical properties. (b) Implantable and wireless smart e-band for feedback-controlled stimulator. (c) Electronic condom for therapeutical use on human.

Reference

1.   Wu, W., *Stretchable electronics: functional materials, fabrication strategies and applications.* Science and Technology of Advanced Materials, 2019. **20**(1): p. 187-224.

2.   Zhang, Y., et al., *Buckling in serpentine microstructures and applications in elastomer-supported ultra-stretchable electronics with high areal coverage.* Soft Matter, 2013. **9**(33): p. 8062-8070.

3.   Fan, J.A., et al., *Fractal design concepts for stretchable electronics.* Nat Commun, 2014. **5**: p. 3266.

4.   Xu, L., et al., *Materials and fractal designs for 3D multifunctional integumentary membranes with capabilities in cardiac electrotherapy.* Adv Mater, 2015. **27**(10): p. 1731-7.

5.   Tang, Y. and J. Yin, *Design of cut unit geometry in hierarchical kirigami-based auxetic metamaterials for high stretchability and compressibility.* Extreme Mechanics Letters, 2017. **12**: p. 77-85.

6.   Silverberg, J.L., et al., *Applied origami. Using origami design principles to fold reprogrammable mechanical metamaterials.* Science, 2014. **345**(6197): p. 647-50.

7.   Dickey, M.D., *Stretchable and Soft Electronics using Liquid Metals.* Adv Mater, 2017. **29**(27).

8.   Wang, Y., et al., *Volume-invariant ionic liquid microbands as highly durable wearable biomedical sensors.* Materials Horizons, 2016. **3**(3): p. 208-213.

9.   Wang, Z., et al., *3D Printable, Highly Stretchable, Superior Stable Ionogels Based on Poly(ionic liquid) with Hyperbranched Polymers as Macro-cross-linkers for High-Performance Strain Sensors.* ACS Appl Mater Interfaces, 2021. **13**(4): p. 5614-5624.

10.   Wang, H., et al., *Ionic Gels and Their Applications in Stretchable Electronics.* Macromol Rapid Commun, 2018: p. e1800246.

11.   Fan, X., et al., *PEDOT:PSS for Flexible and Stretchable Electronics: Modifications, Strategies, and Applications.* Adv Sci (Weinh), 2019. **6**(19): p. 1900813.

12.   Larmagnac, A., et al., *Stretchable electronics based on Ag-PDMS composites.* Sci Rep, 2014. **4**: p. 7254.

13.   Weng, W., et al., *A gum-like lithium-ion battery based on a novel arched structure.* Adv Mater, 2015. **27**(8): p. 1363-9.

14.   Lee, P., et al., *Highly stretchable and highly conductive metal electrode by very long metal nanowire percolation network.* Adv Mater, 2012. **24**(25): p. 3326-32.

15.   Dang, W., et al., *Printable stretchable interconnects.* Flexible and Printed Electronics, 2017. **2**(1).

16.   Bandodkar, A.J., et al., *All-printed stretchable electrochemical devices.* Adv Mater, 2015. **27**(19): p. 3060-5.

17.   Suikkola, J., et al., *Screen-Printing Fabrication and Characterization of Stretchable Electronics.* Sci Rep, 2016. **6**: p. 25784.

18.   Wang, M., et al., *Stencil Printing of Liquid Metal upon Electrospun Nanofibers Enables High-Performance Flexible Electronics.* ACS Nano, 2021.

19.   Chiolerio, A., et al., *Inkjet-printed PEDOT:PSS electrodes on plasma-modified PDMS nanocomposites: quantifying plasma treatment hardness.* RSC Adv., 2014. **4**(93): p. 51477-51485.

20.   Wen, X., et al., *Flexible, multifunctional neural probe with liquid metal enabled, ultra-large tunable stiffness for deep-brain chemical sensing and agent delivery.* Biosens Bioelectron, 2019. **131**: p. 37-45.

21.   Minev, I.R., et al., *Biomaterials. Electronic dura mater for long-term multimodal neural interfaces.* Science, 2015. **347**(6218): p. 159-63.

22.   Farajidavar, A., *Bioelectronics for mapping gut activity.* Brain Res, 2018. **1693**(Pt B): p. 169-173.

23.   Ramadi, K.B., S.S. Srinivasan, and G. Traverso, *Electroceuticals in the Gastrointestinal Tract.* Trends Pharmacol Sci, 2020. **41**(12): p. 960-976.

24.   Lin, X., et al., *Entrainment of intestinal slow waves with electrical stimulation using intraluminal electrodes.* Ann Biomed Eng, 2000. **28**(5): p. 582-7.

25.   Aelen, P., et al., *Pilot acute study of feedback-controlled retrograde peristalsis invoked by neural gastric electrical stimulation.* Physiol Meas, 2009. **30**(3): p. 309-22.

26.   Zhang, J. and J.D. Chen, *Pacing the gut in motility disorders.* Curr Treat Options Gastroenterol, 2006. **9**(4): p. 351-60.

27.   Sevcencu, C., *A review of electrical stimulation to treat motility dysfunctions in the digestive tract: effects and stimulation patterns.* Neuromodulation, 2007. **10**(2): p. 85-99.

28.   Vujic, A., et al., *Going with our Guts*, in *Proceedings of the 2020 International Conference on Multimodal Interaction*. 2020. p. 260-268.

29.   Ng, R.T., et al., *Transcutaneous electrical stimulation (TES) for treatment of constipation in children.* Cochrane Database Syst Rev, 2016. **11**: p. CD010873.

30.   Du, P., et al., *High-resolution mapping of in vivo gastrointestinal slow wave activity using flexible printed circuit board electrodes: methodology and validation.* Ann Biomed Eng, 2009. **37**(4): p. 839-46.

31.   Angeli, T.R., et al., *Intra-operative high-resolution mapping of slow wave propagation in the human jejunum: Feasibility and initial results.* Neurogastroenterol Motil, 2018. **30**(7): p. e13310.

32.   Cherian Abraham, A., et al., *Dynamic slow-wave interactions in the rabbit small intestine defined using high-resolution mapping.* Neurogastroenterol Motil, 2019. **31**(9): p. e13670.

33.   Lo, Y.K., et al., *A Wireless Implant for Gastrointestinal Motility Disorders.* Micromachines (Basel), 2018. **9**(1).

34.   Wang, P.M., et al., *A Wireless Implantable System for Facilitating Gastrointestinal Motility.* Micromachines (Basel), 2019. **10**(8).

35.   Schiemer, J.F., et al., *Five-fold Gastrointestinal Electrical Stimulation With Electromyography-based Activity Analysis: Towards Multilocular Theranostic Intestinal Implants.* J Neurogastroenterol Motil, 2019. **25**(3): p. 461-470.

36.   Snape, W.J., Jr., S.A. Matarazzo, and S. Cohen, *Effect of eating and gastrointestinal hormones on human colonic myoelectrical and motor activity.* Gastroenterology, 1978. **75**(3): p. 373-8.

37.   Schang, J.C., et al., *Myoelectrical activity and intraluminal flow in human sigmoid colon.* Dig Dis Sci, 1986. **31**(12): p. 1331-7.

38. Al-Shboul, O.A., *The importance of interstitial cells of cajal in the gastrointestinal tract.* Saudi J Gastroenterol, 2013. **19**(1): p. 3-15.

39. Sarna, S.K., *Physiology and pathophysiology of colonic motor activity (2).* Dig Dis Sci, 1991. **36**(7): p. 998-1018.

40. Sarna, S.K., *Physiology and pathophysiology of colonic motor activity (1).* Dig Dis Sci, 1991. **36**(6): p. 827-62.

41. Lowe, J.S., Anderson, P. G., & Stevens, A., *Stevens & Lowe's human histology.* 2015.

42. Sarna, S.K., *In vivo myoelectric activity: methods, analysis, and interpretation*, in *Comprehensive Physiology*. 1989. p. 817-863.

43. Sarna, S.K., in *Colonic Motility: From Bench Side to Bedside*. 2010: San Rafael (CA).

44. Sanders, K.M., S.M. Ward, and G.W. Hennig, *Problems with extracellular recording of electrical activity in gastrointestinal muscle.* Nat Rev Gastroenterol Hepatol, 2016. **13**(12): p. 731-741.

45. Merletti, R. and S. Muceli, *Tutorial. Surface EMG detection in space and time: Best practices.* J Electromyogr Kinesiol, 2019. **49**: p. 102363.

46. Raez, M.B., M.S. Hussain, and F. Mohd-Yasin, *Techniques of EMG signal analysis: detection, processing, classification and applications.* Biol Proced Online, 2006. **8**: p. 11-35.

47. El-Sharkawy, T.Y., *Electrical activities of the muscle layers of the canine colon.* J Physiol, 1983. **342**: p. 67-83.

48. Sarna, S.K., *Myoelectric correlates of colonic motor complexes and contractile activity.* Am J Physiol, 1986. **250**(2 Pt 1): p. G213-20.

49.   Dubrovsky, G., et al., *Intestinal Electrical Stimulation to Increase the Rate of Peristalsis.* J Surg Res, 2019. **236**: p. 153-158.

50.   Liu, Y., et al., *Characteristics of myoelectrical activities along the small intestine and their responses to test meals of different glycemic index in rats.* Am J Physiol Regul Integr Comp Physiol, 2020. **318**(5): p. R997-R1003.

51.   Beck, T.W., et al., *A comparison of monopolar and bipolar recording techniques for examining the patterns of responses for electromyographic amplitude and mean power frequency versus isometric torque for the vastus lateralis muscle.* J Neurosci Methods, 2007. **166**(2): p. 159-67.

52.   Mohr, M., et al., *Intermuscular Coherence Between Surface EMG Signals Is Higher for Monopolar Compared to Bipolar Electrode Configurations.* Front Physiol, 2018. **9**: p. 566.

53.   Farmer, A.D., S.M. Scott, and A.R. Hobson, *Gastrointestinal motility revisited: The wireless motility capsule.* United European Gastroenterol J, 2013. **1**(6): p. 413-21.

54.   Hagger, R., et al., *Periodic colonic motor activity identified by 24-h pancolonic ambulatory manometry in humans.* Neurogastroenterol Motil, 2002. **14**(3): p. 271-8.

55.   Arkwright, J.W., et al., *Design of a high-sensor count fibre optic manometry catheter for in-vivo colonic diagnostics.* Opt Express, 2009. **17**(25): p. 22423-31.

56.   Rao, S.S., et al., *Ambulatory 24-h colonic manometry in healthy humans.* Am J Physiol Gastrointest Liver Physiol, 2001. **280**(4): p. G629-39.

57.   Gregersen, H., *Biomechanics of the Gastrointestinal Tract.* 2003.

58.	Nguyen, H.N., J. Silny, and S. Matern, *Multiple intraluminal electrical impedancometry for recording of upper gastrointestinal motility: current results and further implications.* Am J Gastroenterol, 1999. **94**(2): p. 306-17.

59.	Holmes, G.M., E.M. Swartz, and M.S. McLean, *Fabrication and implantation of miniature dual-element strain gages for measuring in vivo gastrointestinal contractions in rodents.* J Vis Exp, 2014(91): p. 51739.

60.	Bassotti, G. and M. Gaburri, *Manometric investigation of high-amplitude propagated contractile activity of the human colon.* Am J Physiol, 1988. **255**(5 Pt 1): p. G660-4.

61.	Swart, P.L., B.M. Lacquet, and A.A. Chtcherbakov, *Chirped fiber optic Bragg grating esophageal pressure sensor*, in *2002 15th Optical Fiber Sensors Conference Technical Digest. OFS 2002(Cat. No.02EX533)*. 2002. p. 235-238.

62.	Boehler, C., et al., *Tutorial: guidelines for standardized performance tests for electrodes intended for neural interfaces and bioelectronics.* Nat Protoc, 2020. **15**(11): p. 3557-3578.

63.	Daubinger, P., et al., *Electrochemical characteristics of nanostructured platinum electrodes--a cyclic voltammetry study.* Phys Chem Chem Phys, 2014. **16**(18): p. 8392-9.

64.	*Colonic Motility: From Bench Side to Bedside.* 2010.

65.	Uno, Y., *Colonic transit time and pressure based on Bernoulli's principle.* Clin Exp Gastroenterol, 2018. **11**: p. 153-163.

66.	Lin, Z. and J.D. Chen, *Advances in gastrointestinal electrical stimulation.* Crit Rev Biomed Eng, 2002. **30**(4-6): p. 419-57.

67. Dickey, M.D., et al., *Eutectic Gallium-Indium (EGaIn): A Liquid Metal Alloy for the Formation of Stable Structures in Microchannels at Room Temperature.* Advanced Functional Materials, 2008. **18**(7): p. 1097-1104.

68. Adler, A. and A. Boyle, *Electrical Impedance Tomography: Tissue Properties to Image Measures.* IEEE Trans Biomed Eng, 2017. **64**(11): p. 2494-2504.

69. Mishra, R.K., et al., *Wearable Flexible and Stretchable Glove Biosensor for On-Site Detection of Organophosphorus Chemical Threats.* ACS Sens, 2017. **2**(4): p. 553-561.

70. Ma, Z., et al., *Permeable superelastic liquid-metal fibre mat enables biocompatible and monolithic stretchable electronics.* Nat Mater, 2021. **20**(6): p. 859-868.

71. Kim, H.-J., C. Son, and B. Ziaie, *A multiaxial stretchable interconnect using liquid-alloy-filled elastomeric microchannels.* Applied Physics Letters, 2008. **92**(1).

72. Yong-Lae, P., C. Bor-Rong, and R.J. Wood, *Design and Fabrication of Soft Artificial Skin Using Embedded Microchannels and Liquid Conductors.* IEEE Sensors Journal, 2012. **12**(8): p. 2711-2718.

73. Wang, B., et al., *An implantable multifunctional neural microprobe for simultaneous multi-analyte sensing and chemical delivery.* Lab Chip, 2020. **20**(8): p. 1390-1397.

74. Vaicekauskaite, J., et al., *Mapping the mechanical and electrical properties of commercial silicone elastomer formulations for stretchable transducers.* Journal of Materials Chemistry C, 2020. **8**(4): p. 1273-1279.

75. Fouillet, Y., et al., *Stretchable Material for Microfluidic Applications.* Proceedings, 2017. **1**(4).

76. Glickman, E., et al., *Interaction of liquid and solid gallium with thin silver films: Synchronized spreading and penetration.* Acta Materialia, 2011. **59**(3): p. 914-926.

77. Geddis, P., et al., *Effect of static liquid Galinstan on common metals and non-metals at temperatures up to 200 °C.* Canadian Journal of Chemistry, 2020. **98**(12): p. 787-798.

78. Geddes, L.A. and R. Roeder, *Criteria for the selection of materials for implanted electrodes.* Ann Biomed Eng, 2003. **31**(7): p. 879-90.

79. Tybrandt, K., et al., *High-Density Stretchable Electrode Grids for Chronic Neural Recording.* Adv Mater, 2018. **30**(15): p. e1706520.

80. Guvanasen, G.S., et al., *A Stretchable Microneedle Electrode Array for Stimulating and Measuring Intramuscular Electromyographic Activity.* IEEE Trans Neural Syst Rehabil Eng, 2017. **25**(9): p. 1440-1452.

81. Westerhof, N., N. Stergiopulos, and M.I.M. Noble, *Snapshots of Hemodynamics.* 2010.

82. Wagenseil, J.E. and R.P. Mecham, *Vascular extracellular matrix and arterial mechanics.* Physiol Rev, 2009. **89**(3): p. 957-89.

83. Camasao, D.B. and D. Mantovani, *The mechanical characterization of blood vessels and their substitutes in the continuous quest for physiological-relevant performances. A critical review.* Mater Today Bio, 2021. **10**: p. 100106.

84. Fukumori, T. and T. Nakaoki, *Significant Improvement of Mechanical Properties for Polyvinyl Alcohol Film Prepared from Freeze/Thaw Cycled Gel.* Open Journal of Organic Polymer Materials, 2013. **03**(04): p. 110-116.

85.   Park, Y.-L., et al., *Influence of cross-sectional geometry on the sensitivity and hysteresis of liquid-phase electronic pressure sensors.* Applied Physics Letters, 2012. **101**(19).

86.   Nguyen, T.Q. and C. Breitkopf, *Determination of Diffusion Coefficients Using Impedance Spectroscopy Data.* Journal of The Electrochemical Society, 2018. **165**(14): p. E826-E831.

87.   Choi, W., et al., *Modeling and Applications of Electrochemical Impedance Spectroscopy (EIS) for Lithium-ion Batteries.* Journal of Electrochemical Science and Technology, 2020. **11**(1): p. 1-13.

88.   Barsoukov, E. and J.R. Macdonald, *Impedance Spectroscopy.* 2018.

89.   Diard, J.P. and C. Montella, *Diffusion-trapping impedance under restricted linear diffusion conditions.* Journal of Electroanalytical Chemistry, 2003. **557**: p. 19-36.

90.   Noda, T., et al., *Electrochemical Evaluation of Geometrical Effect and Three-dimensionalized Effect of Iridium Oxide Electrodes Used for Retinal Stimulation.* Sensors and Materials, 2018.

91.   Swaminathan, M., et al., *Video Imaging and Spatiotemporal Maps to Analyze Gastrointestinal Motility in Mice.* J Vis Exp, 2016(108): p. 53828.

92.   Schreiber, D., et al., *Motility patterns of ex vivo intestine segments depend on perfusion mode.* World J Gastroenterol, 2014. **20**(48): p. 18216-27.

93.   Hoffman, J.M., E.M. Brooks, and G.M. Mawe, *Gastrointestinal Motility Monitor (GIMM).* J Vis Exp, 2010(46).

94.   Yang, P.J., et al., *Hydrodynamics of defecation.* Soft Matter, 2017. **13**(29): p. 4960-4970.

95. Dickson, E.J., et al., *An enteric occult reflex underlies accommodation and slow transit in the distal large bowel.* Gastroenterology, 2007. **132**(5): p. 1912-24.

96. Taborda, J.A.V., et al., *Encapsulation of bioactive compounds from byproducts of two species of passionflowers: evaluation of the physicochemical properties and controlled release in a gastrointestinal model.* Heliyon, 2021. **7**(7): p. e07627.

97. Christensen, M.B., K. Oberg, and J.C. Wolchok, *Tensile properties of the rectal and sigmoid colon: a comparative analysis of human and porcine tissue.* Springerplus, 2015. **4**: p. 142.

98. Qiao, Y., et al., *Measurement of mechanical properties of rectal wall.* J Mater Sci Mater Med, 2005. **16**(2): p. 183-8.

99. Gayer, C.P. and M.D. Basson, *The effects of mechanical forces on intestinal physiology and pathology.* Cell Signal, 2009. **21**(8): p. 1237-44.

100. Fink, S., *The Intraluminal Pressures in the Intact Human Intestine.* Gastroenterology, 1959. **36**(5): p. 661-671.